

Study of nearby spiral galaxies- IC 342 and NGC 628 at low frequencies using LOFAR

Ayushi Mandlik



Argelander-
Institut
für
Astronomie

Masterarbeit in Astrophysik
angefertigt im Argelander Institut für Astronomie

vorgelegt der
Mathematisch-Naturwissenschaftlichen Fakultät
der
Rheinische Friedrich-Wilhelms-Universität Bonn
Deutschland

July 1, 2018

To my parents

I hereby declare that this thesis was formulated by myself and that no sources or tools than those cited were used.

Date

Signature

1. Gutachter: Prof. Dr. Michael Kramer
2. Gutachter: Prof. Dr. Cristiano Porciani

Abstract

This thesis presents the first arcsec resolution observations of two nearby spiral galaxies- IC 342 and NGC 628, using LOw Frequency ARray (LOFAR). Low frequency (145 MHz) continuum observations trace older, lower-energy cosmic-ray electrons in the galaxy via radio synchrotron emission. These electrons are ones that have travelled away from their locations of origin (supernova remnants) and are present in the extended disks and haloes of the galaxies. Low frequency surveys also help us understand the properties of warm ionized mediums of galaxies with the help of free-free absorption of synchrotron flux density by the ionized gas. The first part of my thesis presents FACTOR, which is the novel algorithm used to calibrate and image the galaxies using LOFAR visibilities. Images of the two face-on star forming spiral galaxies are presented at various resolutions. This is followed by an analysis of the spectral index distribution in the galaxies obtained between the LOFAR maps and VLA¹ maps of 1.49 GHz for IC 342 and 3 GHz for NGC 628. Correlations between spectral index values and the levels of star formation are obtained with the help of far-infrared, H-alpha and thermal radio emission maps, which trace the regions of star formation in galaxies. Thermal fractions required to explain the observed spectral indices are calculated. The values of thermal fraction needed to explain the flat spectral index values seen in the central part and arms of IC 342 seem unphysical. This leads to the explanation that IC 342 suffers from higher levels of thermal absorption due to higher star formation rates. On the other hand, NGC 628 does not seem to suffer much from thermal absorption owing to its lower levels of star formation. Low frequency observations are also ideal to study diffuse magnetic fields in galaxies. The technique of RM Synthesis is applied to obtain the parallel component of magnetic fields (while its perpendicular counterpart can be calculated from the synchrotron flux density). As a result of wavelength dependent Faraday depolarization, diffuse polarized emission cannot be detected for either of the two galaxies.

¹Very Large Array

Acknowledgments

I would like to start by acknowledging Dr. Rainer Beck. It was an honour and a privilege to work under you. You were very kind and patient with me throughout this project. Your immense knowledge and love for the subject gave me courage to keep going with the project, in spite of several negative results. I would also like to thank Dr. Andreas Horneffer, for helping me with definitely the most difficult part of my thesis. You were extremely supportive, explaining even the most fundamental and basic concepts involved in LOFAR data calibration. I also heartily thank Prof. Dr. Cristiano Porciani. You were one of the best teachers in my life. Your lectures were simply amazing, and your exams- a very humbling experience. Preparing for the Astro-Seminar under your guidance was also a lot of fun. I would also like to thank Prof. Dr. Michael Kramer, for supporting me during my thesis, and for letting me be a part of your amazing group. I owe my deep gratitude to Dr. Thushara Pillai and Dr. Jens Kauffmann for your willingness to help me, even when I was very new to the concept of ‘research’. Another person I am thankful for is Dr. Cathy Horellou. You were very helpful during my Sweden trip, and your crepes are really good! I would also like to thank Dr. Shane O’ Sullivan for providing me with your codes, it would have taken me forever to write them myself. I would also like to thank Dr. Aritra Basu. Your understanding of the subject and your simple explanations for everything were extremely helpful. You were an amazing mentor and friend, and it was a shame you had to leave before the completion of my Masters. I am sure that my thesis would have been much better had you been around to clarify my doubts.

I would also like to thank Kira Kuhn for being very helpful. It is indeed true what they say, ‘when in doubt, ask Kira!’. I would like to thank all my friends who were always there to keep my spirits high. I would like to especially thank Maja Kierdorf. After Andreas left the institute, you were more of a teacher to me than anyone, taking time off your schedule to read my thesis and even coming in to explain the comments! I would also like to thank Yik Ki Ma, for proof reading my thesis (with such detailed suggestions!). I would also like to thank Nataliya Porayko for coming in and explaining how magnetic fields are studied.

I would like to thank my fortunes for giving me such amazing parents, whom I miss every single day! Mumma, your constant support and faith in me kept me going during this humbling journey that was my Masters. Papa, without your guidance and understanding, I would never have reached this juncture. I would also like to thank Shirley Joseph, my long distance friend. Life is always better when your best friend is there to gossip with, in spite of the long miles. Last but not the least, I would like to thank Vishnu Balakrishnan, for always having my back, and keeping me happy with a constant supply of food. Next time people say I look ‘healthy’, I shall let them know that you are the culprit. I hope that in years to come, some of your workaholic lifestyle would rub off on me, and help me become a better researcher.

Contents

Abstract	vii
Acknowledgments	ix
Contents	xi
List of Figures	xiii
List of Tables	xvii
1 Introduction	1
1.1 Low frequency astronomy	1
1.2 LOw Frequency ARray- LOFAR	2
1.3 Importance of low frequency astronomy (LOFAR Key Science Projects)	5
1.3.1 Astrophysical processes at Low Frequencies	6
1.4 Image synthesis for interferometers	9
1.4.1 Interferometric concepts	10
1.4.2 UVW coordinate system	10
1.4.3 Calibration techniques used for LOFAR calibration	11
1.4.4 Overview of imaging procedure for LOFAR	13
2 Imaging	15
2.1 NGC 628	15
2.2 IC 342	15
2.3 Observational setup	17
2.4 Calibration of LOFAR data	18
2.4.1 Direction independent part	18
2.4.2 Direction dependent part	18
2.4.3 Overview of Factor	20
2.5 Imaging	27
2.5.1 Checking flux density scales using TGSS	34
3 Scientific analysis	35
3.1 Spectral index mapping	35
3.1.1 IC 342	35
3.1.2 NGC 628	36
3.2 Interpretation of spectral index maps	36
3.2.1 IC 342	36
3.2.2 Case of missing flux	41
3.2.3 NGC 628	45
3.3 Star Formation in the two galaxies	47
3.4 Discussion	49

4 Magnetic field study at Low frequency	51
4.1 Introduction	51
4.2 Faraday Rotation Measure synthesis technique	52
4.3 Faraday tomography of the galaxies	54
4.3.1 RM Synthesis to study diffuse emission:	54
4.3.2 Extra-galactic polarized sources	56
A Appendix	59
A.1 Radio Interferometry Measurement Equation- RIME formalism	59
A.2 NGC 628- correlation plot	61
A.3 Making of thermal maps	61
Bibliography	66

List of Figures

1.1	The different Antenna types in LOFAR. <i>Left:</i> Low Band Antenna is held upright by the two copper wires connected to its top that help in detection of the two polarizations, and the ground mesh (Schellart et al. 2013). <i>Right:</i> Each High Band Antenna tile has 16 aluminium elements held together by an expanded polystyrene structure (van Haarlem et al. 2013)	2
1.2	Arrangement of the LOFAR stations in Europe. <i>Left:</i> The blue regions represent the international stations. The orange regions in the represent the remote stations. <i>Right:</i> On a closer look, the red regions represent the core stations. These images were obtained from http://astron.nl/lofar/tools/lofarmap.html	3
1.3	The uv coverage of LOFAR including all core, remote and international stations (van Haarlem et al. 2013). The simulation of this uv-coverage is based on a hypothetical 6 hour observation of a source at a declination of 48 deg between 30-78 MHz using single beam with bandwidth of 48 MHz.	4
1.4	The Spectral Energy Distribution of M82, a star-burst galaxy. The region below the frequency of 30 GHz is mostly dominated by non-thermal, synchrotron emission from cosmic ray electrons. At frequencies higher than that, free-free emission dominates, while at frequencies above 200 GHz, thermal dust emission dominates. Free-free absorption due to HII regions absorbs some of the emission. This absorption takes place throughout the galaxy and is responsible for the flattening of the spectrum at the frequencies below 1 GHz (Condon 1992).	5
1.5	This is a schematic diagram depicting the lifetime of our Universe. At redshift $z \approx 1100$, the dark ages begin, and EoR begin at $z \approx 6 - 12$. Courtesy of National Astronomical Observatory of Japan (NAOJ).	6
1.6	When an electron moves at relativistic speeds, the \sin^2 radiation pattern is Lorentz transformed. <i>Left:</i> The radiation pattern of a non-relativistic electron. <i>Right:</i> The relativistic radiation pattern. This image has been taken from http://www.astro.utu.fi/\protect\unhbox\voidb@x\penalty\OM\{cflynn/astroII/14.html	7
1.7	The radio spectrum of an ideal HII region. Here, thermal emission and absorption process are dominant, because an HII region is in LTE. At low frequencies, the slope is 2.0, while the slope at higher frequencies is around -0.1. At the total opacity of around 1, the turn over occurs. This is when free-free absorption is seen to dominate. This image has been taken from https://www.cv.nrao.edu/course/astr534/FreeFreeEmission.html	9
1.8	A two element interferometer observing an arbitrary source in the direction \hat{s} , with the baseline B . The two elements are represented as 1 and 2 with V_1 and V_2 as their respective visibilities. ‘X’ represents the correlator where the multiplication and averaging of the signal takes place.	11
1.9	The UVW coordinate system. <i>Left:</i> The (u, v, w) coordinates, along with the directions. The \vec{B}_λ represents the direction of the source in UVW coordinate system. <i>Middle:</i> The (l, m) coordinate system on the image plane, which is visited upon again section A.1. <i>Right:</i> The Earth EWNS directions.	11

1.10 LOFAR is represented by three antennas at ground level. The ionospheric electron density structure (grey bubbles)are shown, with the various fields of view shown in (red, green and blue areas). For antennae like VLA, the primary beam patterns, shown in regimes 1 and 2, each individual antenna has the field of view in which the TEC stays approximately the same. The primary beam patterns in LOFAR are more like the ones shown in regimes 3 and 4. The TEC along the line of sight in the field of view has variations. In regimes 1 and 3, the relatively compact array configurations are shown. The TEC variation across the array for a single viewing direction within the FoV is approximately a gradient. In regimes 2 and 4, relatively extended array configurations are shown. The TEC variation varied significantly for the fields of view in such configurations. This image has been taken from Intema et al. (2009), where a very good description of the calibration techniques is given.	12
2.1 Schematic of the chemical and physical structure of the nucleus of IC342(Meier & Turner 2005)	16
2.2 This was the arrangement of baselines used for the observation. This is a plot generated by task in CASA called 'plotms' for the first measurement set for the frequency 111 MHz in the first time step. From the plot, one can see the baselines used in terms of meters. As can be seen, the observation uses a dense core to image diffuse flux in the galaxy- the disk and the halo parts. <i>Right:</i> This image shows the shorter baselines used. The shortest projected baseline used was around 23 m.	17
2.3 <i>Left:</i> Initial subtract image of NGC 628, using frequencies between 135 to 167 MHz. It has a restoring beam of 43.99 arcsec by 31.64 arcsec and position angle of -17.27deg. As can be seen, artifacts from individual sources, such as 3C 049 (at RA: 01h41m09.160s and DEC: +13d53m28.05s in J2000 coordinate system), can severely affect the galaxy image quality. Hence, the field of view is divided into "isoplantic" patches called "facets". <i>Right:</i> The facet patches can be seen in the image, and are made around the radio sources present in each facet. They are represented by the white dots in the image on the right. The facet patches are based on the Veroni tessellation scheme.	19
2.4 This image depicts the faceting scheme used for NGC 628. The middle facet marked "target" is NGC 628. The sources marked 1, 4 and 5 were included by hand due to their high fluxes. The image is the one obtained from the initial calibration (same as the one in the previous figure). The beam is elongated to account for the low elevation elongation of the LOFAR primary beam.	21
2.5 Self calibration images of the facet with source 194- otherwise known as 3C 49. The image marked "Dir. Indep." is the direction independent image of the facet. In the second row, the phase term is being solved, which took three iterations. Then, the phase + amplitude calibration was done, which took 7 iterations.	22
2.6 <i>Left:</i> The initial subtract image of facet containing the source 3C49. <i>Right:</i> Final self-cal image of 3C49. The image is considerably better than the one on the left,however some of the artifacts still remain. The source is the source is farther away from the target source, hence, the artifacts that remain do not affect the image too much.	23
2.7 Faceting in IC342 for Direction Dependent calibration in Factor. The facets have been overlaid on the image made using averaged Prefactor data. The resolution of the image is 17.35 by 12.72 arcsec. It was cleaned to a threshold of 0.3 mJy with Briggs weighting of -0.5.	23
2.8 The four SNR candidates (labelled 1,2,3 and 4). The source in the dotted red circle cannot be a SNR because these SNRs do not have a flux density as high as the source.	28
2.9 This image depicts the source that was a major problem in the imaging of IC 342, giving rise to several artifacts. The Figure on the left depicts the image in which the source has been subtracted while on the right, the source remains. There is little to no difference between the two and there is almost no change in the noise of the images. Hence, subtracting the source also provided no help.	28
2.10 This is the LOFAR image of IC342 at the central frequency of 146.2 MHz. Bandwidth of the observation was 62.5 MHz. This image has the resolution of 12.48" by 10.26"; PA: -8.10 deg. The contours are at 3, 8, 12, 18, 32 and 44 × 0.39 mJy/beam, which is the noise of the image in a quiet region.	29
2.11 This image has the resolution of 25.93" by 23.26"; PA: 62.7 deg. The contours are at 3, 8, 12, 18, 32 and 44 × 0.56 mJy/beam, which is the noise level of the image.	29
2.12 This image of IC 342 has the resolution of 38.15" by 34.39"; PA: 23.99 deg. The contours are at 3, 8, 12, 18, 32 and 44 × 0.78 mJy/beam, which is the noise level of the image.	30
2.13 This image of NGC 628 has the resolution of 20"; PA: 180 deg. The contours are at 3, 8, 12, 18, 32 and 44 × 0.98 mJy/beam, which is the noise level of the image	31

2.14 This image of NGC 628 has the resolution of 26.06" by 25.21"; PA: 88.26 deg. The contours are at 3, 8, 12, 18, 32 and 44×1.04 mJy/beam, which is the noise level of the image	31
2.15 This image of NGC 628 has the resolution of 40"; PA: 180 deg. The contours are at 3, 8, 12, 18, 32 and 44×1.06 mJy/beam, which is the noise level of the image.	32
2.16 The Figure shows the elevation of the two target sources- IC 342 and NGC 628 at the time of observation. The elevation of NGC 628 is lower, which resulted in a lower sensitivity i.e., higher noise level in its image. The plots have been obtained using https://support.astron.nl/otool	33
2.17 The values of integrated flux density values of point sources from the TGSS catalog and the integrated flux density values obtained from LOFAR were compared. On an average, the TGSS point sources had a flux density a factor of 1.3 higher than the LOFAR point sources. Hence, the maps have been multiplied by a factor of 1.3.	34
3.1 <i>Above:</i> The spectral index map of IC 342 obtained from 1.4 GHz VLA map and 145 MHz LOFAR map at 45" resolution. It uses values above 5σ the noise level (5 σ) from the VLA and LOFAR maps. The contours on the map are 0.2, 0.4, 0.6, 0.8, 1, 0 \times -1. <i>Below:</i> The error map for the spectral index map. The contours are the same for both the images.	37
3.2 The spectral index distribution for IC 342 for the spectral index map shown in Figire 3.1. The binning is done according to Freedman-Diaconis Rule (Freedman & Diaconis 1981)	38
3.3 <i>Above:</i> The spectral index map for NGC 628 obtained from 3 GHz VLA map and 145 MHz LOFAR map at 20" resolution. This is a 3-sigma spectral index map. The contours on the map are 0.2, 0.4, 0.6, 0.8, 1, 0 with unit contour level of -1. <i>Below:</i> The error map for the spectral index map. The contours are the same for both the images.	39
3.4 This histogram shows the distribution of the spectral index values for NGC 628. The median lies at -0.86 (expected value).	40
3.5 Spectral Energy Distribution (SED) for the three process important in star forming galaxies like IC 342. The red dashed line indicates synchrotron emission, and has a spectral index value (α) of -0.7. The thermal emission is indicated by the blue dotted line, and has a spectral index value of -0.1. Thermal absorption process is indicated by the green curve. This process is responsible for the flattening of the spectral index at low radio frequencies. Based on the two frequencies considered to obtain the spectral index, the flattening and steepening of the spectrum can be explained.	40
3.6 This image depicts the correlation of the flatter spectral index and the presence of thermal emission. The contours are 0.5, 5, 18, 32, 80 of the thermal map with unit contour level of 10 mJy/beam	41
3.7 Correlation of the thermal intensity values with the spectral index map values for IC 342. The spectral index values are obtained by clipping the values of flux densities lower than 5σ the noise level in 1.49 GHz and 145 MHz map, for each pixel. From the Figure, it is evident that regions with higher radio thermal flux density which indicate the presence of free-free absorption from star forming regions, have a flatter spectral index values. The 'tail' seen at the right hand portion showing the discrepancy may be because of the missing diffuse flux density that affects spectral indices at low intensity.	42
3.8 The overlaid plot is the FIR map of IC 342 at $350\mu\text{m}$. One can notice the correlation of flatter spectral index and higher flux density of this map. The contours represent 0.2, 0.4, 0.6, 0.8, 1, 1.5, 2, 3 \times 15 Jy/beam.	42
3.9 This plot shows the flux density values from previous study done for the galaxy by Tabatabaei et al. (2017) for IC 342 as blue dots, with the fit shown in blue line. The green dashed line represents the extrapolated fit with the slope of -0.76. The pink star represents the flux density from the LOFAR map, and the red star represents the expected flux density for the frequency of 145 mHz.	43
3.10 The radial profiles for the full UV range maps. <i>Left:</i> The radial profile of the galaxy IC 342 i.e., radius vs log of integrated flux density for 20 cm map. <i>Right:</i> The radial profile for the LOFAR map. The bright background source for both the images has been subtracted before the integration has been performed.	44
3.11 This is the spectral index map obtained between $\lambda 6.2$ cm and $\lambda 20.1$ cm at 25" resolution. Contours show the total intensity at $\lambda 6.2$ cm. It has been taken from Beck (2015).	45
3.12 This image depicts the correlation of the flatter spectral index and the presence of H- α emission. The contours are 0.5, 1, 3, 5, 8, 12, 18, 32, 44, 80 of the h-alpha map with unit contour level of 5 mJy/beam. The regions are described in the text.	46
3.13 Overlaying the LOFAR map onto an optical image from SDSS shows that this region contains a stellar object. This was done inorder to understand the region marked D	46

3.14 Correlation plots of the thermal intensity values value with the spectral index map values, for each pixel. The various regions have different slops of correlation, which is interesting. <i>Left:</i> The correlation plot of the H-alpha map flux density. the region marked D in this case seems to have a higher flux in H-alpha map, but with a steep spectral index. <i>Right:</i> The correlation plot of the thermal radio map. The region D in this plot vanishes. Hence, the discrepancy seen in region D was because of an improper continuum subtraction.	47
3.15 Correlation of the flatter spectral index in NGC 628 and the presence of thermal radio emission at 3 GHz frequency. The contours are 0.1, 0.2, 0.4, 0.6, 1×0.1 mJy/beam.	48
3.16 The radial profile of the galaxy NGC 628 i.e., radius vs log of integrated flux density for 3 GHz map (Mulcahy et al. 2017) and 145 MHz LOFAR map.	48
3.17 The SFR are shown as small triangles (Pan et al. 2014). Each radial step here is $10''$. One can see a similarity in the two plots. In the center, high star formation exists, and that region has a flat spectral index.	49
4.1 Flow chat depicting the procedure of RM Synthesis to understand polarization in astronomical objects, using the visibilities obtained from a radio receiver	53
4.2 Instrumental polarization seen at the Faraday depth of 0 rad/m ²	55
4.3 One of the sources from the Taylor catalog that has been observed to have a higher polarized intensity compared to other sources in the FoV of NGC 628 (7.32 mJy). It is expected to be polarized at 150 MHz, but no polarization is seen. This image has been taken from the NVSS survey and is at a frequency of 1.4 GHz.	57
4.4 Most of the Faraday Spectrum that has been studied looks like this, thus making it impossible to understand if there are any real peaks in the Faraday spectrum.	58
A.1 Correlation of the flux density value with the spectral index map values, for each pixel. The various regions have different slops of correlation, which is interesting. This plot shows the regions A, C and D.	61

List of Tables

1.1	LOFAR specifications, all obtained from (van Haarlem et al. 2013)	3
1.2	The LOFAR imaging modes	4
2.1	Parameters of NGC 628	15
2.2	Parameters of IC 342	16
2.3	Parameters of NGC 628	17
2.4	This table shows the diagnostic plots that are obtained as an output from the Prefactor pipeline. They give an overview of the condition of the data and help us select and flag any data sets that seem bad, and were not previously flagged by the pipeline.	26
2.5	The weighting schemes in imaging synthesis.	27
2.6	The parameters of the images for IC 342.	28
2.7	The parameters of the images for NGC 628.	30
3.1	If a spectral index for synchrotron emission is assumed as -0.7 and thermal emission is assumed as -0.1 , the percentage of thermal fraction for the observed spectral index values (between frequencies of 145 to 1490 MHz, α_{obs}) are obtaind (represented as $f_{\text{th}-0.7}$), at the two frequencies — 145 MHz and 1.49 GHz. The same is done when the spectral index for synchrotron emission is assumed to be -0.5 and the thermal fraction is represented as $f_{\text{th}-0.7}$. These values have been obtained using the code from Dr. Beck (priv. comm).	38
4.1	a and b represent the RA and DEC as given the the Taylor catalog. d is from the Taylor catalog, while c is the quantity of the Van Eck source. The degrees of depolarization is given in the last column using the equation 4.12.	56
4.2	All these sources are from the Taylor catalog, which are present in my field of view. They are not polarized at 150 MHz in my study.	57

Chapter 1

Introduction

1.1 Low frequency astronomy

History of radio astronomy

- | | |
|-------|--|
| 1933 | At the Bell Labs, Karl Jansky was trying to understand the source of interference at short wavelengths in the transatlantic wireless communications, and discovered radiation at 20.5 MHz frequency that moved across our sky. He concluded that this radiation was not from Earth. |
| 1937 | Grote Reber speculated that these signals were thermal in nature and built a parabolic reflector radio telescope with a diameter of 9.5 m and made the first radio map depicting the galactic plane and parts of the sky at 160 MHz, and published the paper in 1944 (Reber 1944). |
| 1940s | Innovations during the Second World War in the RADAR technology further helped the research. J.S. Hey, England and G. C. Southworth discovered that the Sun was radiating radio emission. This was followed by discovery of fluctuation in cosmic radiation at radio frequency by J.S. Hey, S.J. Parsons, and J.W. Phillips (Hey et al. 1946). Several discrete radio sources were also identified. Radio emission from meteors was also studied. |
| 1950s | In the paper Ewen & Purcell (1951) , H. I. Ewen and E. M. Purcell observed the HI 21 cm line from a Galactic source at declination of 5 deg, as predicted by van de Hulst in 1945. Several observatories came to life in this decade such as Cambridge observatory that helped in producing the 2C and 3C catalogues. These were the first catalogues to make use of aperture synthesis technique. Radio emission from Jupiter was also studied at 22 MHz and 3 GHz (Burke & Franklin 1955). |
| 1960s | A. Penzias and R. Wilson using the Holmdel Horn Antenna at the Bell Labs made one of the most important astrophysical discoveries: the Cosmic Microwave Background, for which they were awarded the Nobel prize in 1978. This decade also marked the discovery of pulsars by J. Bell in her article "Little Green Men, White Dwarfs or Pulsars?" (Bell Burnell 1979). A. Hewish received the Nobel prize in 1974 for this discovery. |
| 1970s | Hulse and Taylor discovered the first binary pulsar system at Arecibo, and thus proved the presence of Gravitational wave radiation, after conducting pulsar timing for nearly 20 years (Hulse & Taylor 1975). They were awarded the Nobel prize for this discovery in 1993. The first global radio telescope was formed in 1976 to observe water maser sources. |
| 1980s | The need for better resolution gave rise to the construction of interferometers such as TPT in Clark Lake, observing at the frequency of 57.5 MHz. The first self calibration for VLA images was done. Astronomical Image Processing Software (AIPS) was also released. |
| 1990s | VLA system observing at 74 MHz frequency was used. Planck black-body spectrum for the CMB was measured, and the anisotropy was discovered for the first time using COBE satellite (Kogut et al. 1993). Mather and G. Smoot were awarded the Nobel prize for this discovery in 2006. |

During 1970 to 2000, due to the need for higher resolutions, studies were mostly focused on radio frequencies of > 1 GHz (see section 1.4). Several telescopes sensitive to the higher radio frequency were made- VLA, ATCA, GMRT, MERLIN and single dish telescopes such as Effelsberg, Arecibo and Lovell. Interest in low frequency radio astronomy began when many sources were seen to have inverted spectra due to synchrotron self-absorption or

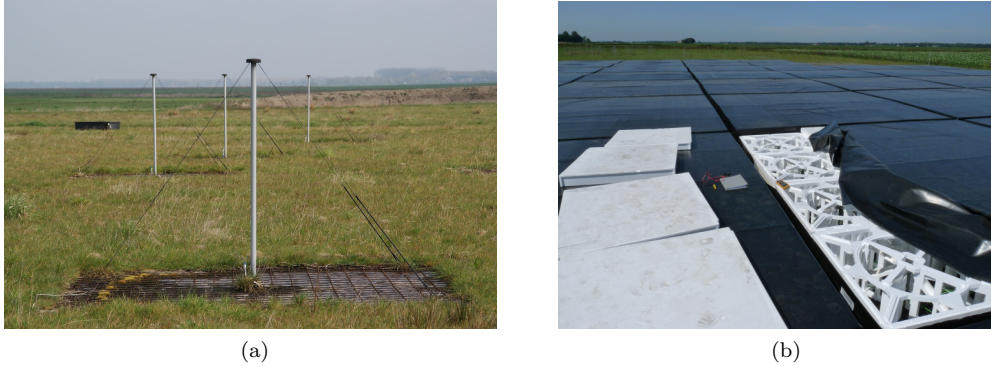


Figure 1.1: The different Antenna types in LOFAR. *Left:* Low Band Antenna is held upright by the two copper wires connected to its top that help in detection of the two polarizations, and the ground mesh ([Schellart et al. 2013](#)). *Right:* Each High Band Antenna tile has 16 aluminium elements held together by an expanded polystyrene structure ([van Haarlem et al. 2013](#))

free-free absorption (see section [1.3.1](#)). NRAO and the Naval Research Laboratory completed the implementation of VLA at 73.8 MHz in 1998 and found that ionospheric phase shifts posed the biggest difficulty in calibrating data. It was found that self-calibration could help with this ([Kassim et al. 2007](#)). In the paper [Cohen et al. \(2006\)](#), 70,000 sources were cataloged at 77 MHz, including several extra-galactic sources such as high redshift galaxies, galaxy clusters, Supernova Remnants (SNRs) and Galactic sources such as pulsars. It covers almost 95% of the 3π sr of sky above -30 deg declination. This survey is very useful for calibration in LOFAR and has been revised to give 95,000 sources in [Lane et al. \(2012\)](#). In the paper [Wilkinson \(1991\)](#), a 1 km² array was proposed so as to study the neutral hydrogen at cosmological distances, called the Square Kilometer Array (SKA). Due to cost constraints, the concept of Phased Arrays ([van Ardenne et al. 2000](#)) using dipole antennae was proposed, which then gave rise to LOFAR.

1.2 LOW Frequency ARray- LOFAR

LOFAR or LOw Frequency Array is a radio interferometer mainly located in the Netherlands. It consists of two types of receiving elements: the Low Band Antennae (LBA) that covers the frequency range of 10-90 MHz, and the High Band Antennae (HBA) that covers the frequency range from 110-250 MHz. It is interesting to note that the pointing in LOFAR is done by applying digital delays to elements of individual stations. The LBA (shown in Figure [1.1a](#)) in reality can only operate between the frequency range of 30-80 MHz due to the presence of Radio Frequency Interference (RFI) at the lower frequency regime and the commercial FM band at the higher regime. An LBA dipole can detect two orthogonal linear polarizations, with an all-sky sensitivity. The dipoles themselves make up the elements to do beam-forming. The HBA (shown in Figure [1.1b](#)) can reach frequency only upto 240 MHz due to RFI. 16 antennae are grouped under one “tile”, and each of these tiles can form a “tile beam”. Each tile does the beam-forming with the help of an analogue beam-former that adds a delay to each dipole. LOFAR has a dense core i.e., it has numerous short baselines that are very helpful in the study of diffuse emission. It currently has 24 core stations (CSs) located in Exloo, Netherlands, and 14 remote stations (RSs) located all over the Netherlands. These stations have 96 LBAs and 48 HBAs with 48 digital Receiver Units (RCUs). These arrangements can be seen the Figure [1.2](#). The international stations (ISs) are present in Germany (5 stations), Great Britain (1 station), France (1 station), Sweden (1 station) and Ireland (1 station). A summary of the arrangement and other properties of LOFAR are given in Table [1.1](#).

The data from both LBA and HBAs are sent to the receiver unit (RCU), where digitization using Analog to Digital converter through coaxial cables. Then the beam-forming is done in the digital electronics section. After that, the signal is either sent to the Cobalt correlator in Groningen or recorded and dealt with locally based on the observing mode. LOFAR has three main observing modes that are explained in the Table [1.2](#). The data streams from the individual dipole antennae are sent to the Central Processing (CEP) facility located in Groningen through a dedicated network high speed fibers. The data is then processed in the Blue Gene/P supercomputer. During this processing, the signal from the stations is correlated, and the beam-forming is done. After this, the data is given to the storage cluster. The data is processed using several reduction pipelines before being stored in the LOFAR long term archive (LTA) for scientific purposes. The CEP4 cluster, part of the LOFAR clusters, is used

Characteristic	Value	Comments
Frequency range	10-90 MHz	LBA
	110-190 MHz	HBA
Shortest baseline	68 m	among CSs, RSs and ISs (unprojected values)
Maximum baseline	3.5 km	CSs
	121 km	RSs
	1158 km	ISs
Number of Polarizations	2	
Bandwidth	48 MHz	16-bit mode
	96 MHz	8-bit mode
Maximum number of simultaneous beams	244	16-bit mode
	488	8-bit mode

Table 1.1: LOFAR specifications, all obtained from ([van Haarlem et al. 2013](#))Figure 1.2: Arrangement of the LOFAR stations in Europe. *Left:* The blue regions represent the international stations. The orange regions in the represent the remote stations. *Right:* On a closer look, the red regions represent the core stations. These images were obtained from <http://astron.nl/lofar/tools/lofarmap.html>

to do the initial processing and calibration using pipelines on the data from the Cobalt correlator (in Groningen). Another cluster- CEP3, used by LOFAR users to decide the strategy to be used for calibration. Once the data has been processed, it is made available on Long Term Archive (LTA).

Some of the packages used for the calibration of LOFAR data are: Astronomical Image Processing Software(AIPS), Common Astronomy Software Applications (CASA ; [McMullin et al. 2007](#)), AOFlagger (helps in flagging RFI) ([Offringa et al. 2012](#)), SAGECal (calibration package), dysco (compressing storage manager for measurement sets) and several others, which will be visited upon during the course of the thesis. Some of the performance metrics of LOFAR are described below:

- The rate of change of the ionospheric phase above the Netherlands is 1 rad per 15 s in the 110 to 190 MHz band ([van Haarlem et al. 2013](#)). For LBA, water may affect the gain by the order of 10%, though HBA amplitudes remain pretty stable. These effects of ionospheric phase shift can be significantly depreciated using the method of self-calibration.
- The angular resolution is from 0.5 deg to sub-arcsec levels, depending on the declination of the source, and the array configuration.
- One the factors that affect the image quality is the uv coverage. As can be seen from the Figure 1.3, we can easily see that LOFAR has a very dense core and there are several long baselines, for better resolution.

Modes	Description
Interferometric	Gives visibility data to be used in surveys and for single source imaging.
Beam Formed	This is used when high time resolution is needed e.g., for pulsars, cosmic rays, etc.
Direct Storage	Uncorrelated data is recorded locally for single station all sky imaging or local Transient Buffer Board (TBB) experiments.

Table 1.2: The LOFAR imaging modes

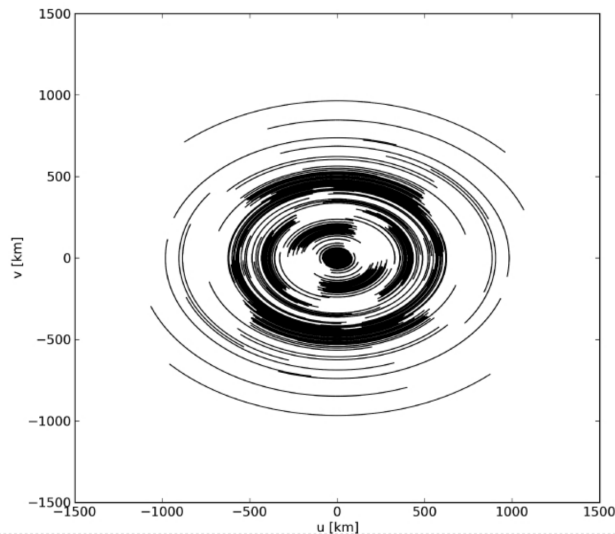


Figure 1.3: The uv coverage of LOFAR including all core, remote and international stations (van Haarlem et al. 2013). The simulation of this uv-coverage is based on a hypothetical 6 hour observation of a source at a declination of 48 deg between 30-78 MHz using single beam with bandwidth of 48 MHz.

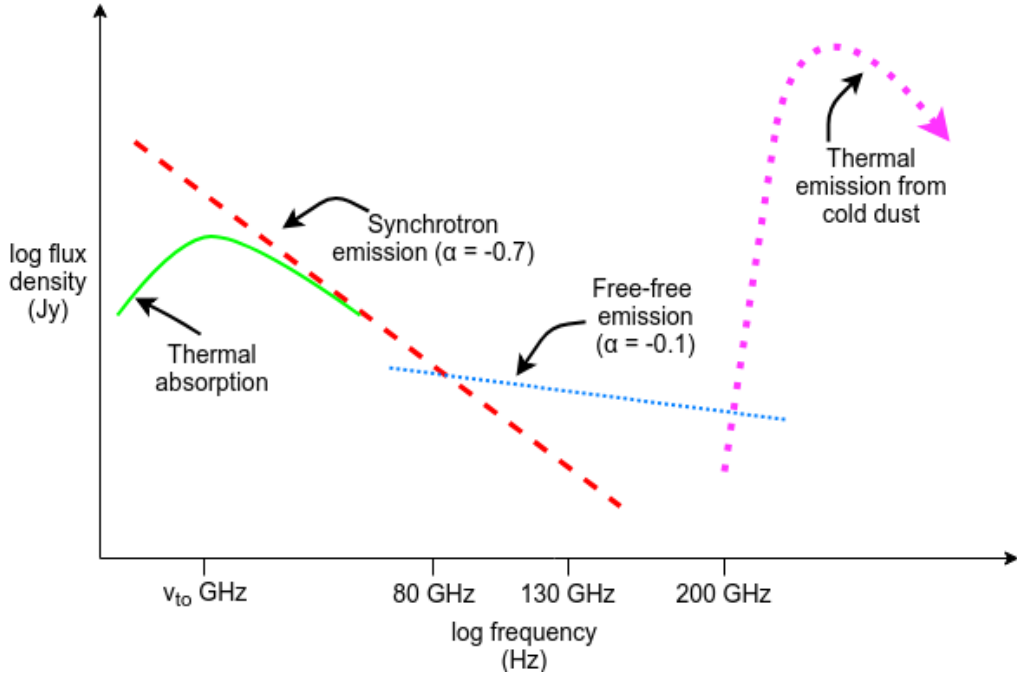


Figure 1.4: This is the Spectral Energy Distribution plot, showing the processes that are dominant at various frequency ranges. Thermal emision from cold dust dominates the spectrum for infrared frequencies (>200 GHz). For frequencies between 80 to 200 GHz, free-free emission dominates the spectrum. From frequencies below 80 GHz, synchrotron emission dominates the spectrum. In regions where the total opacity of the region becomes ≈ 1 or more, the turn over is seen, and thermal absorption lowers the synchrotron flux density. This plot is only representative of the various processes and cannot be taken as an accurate representation of the frequency ranges indicated. This is because these process differ for varying objects, such as in compact sources such as AGNs, synchrotron self-absorption may be responsible for the turn over seen at low frequencies, and not thermal absorption. Also, for high redshift galaxies, these frequency ranges are different.

- The band-pass of LOFAR is affected by several factors: the station beam- which is in itself frequency dependent, the interaction between the antenna elements and the low noise amplifier (LNA). Inorder to take care of this, a digital correction is applied within each 0.2 MHz subband.
- The Field of View (FoV) of LOFAR ranges from 2 to 1200 deg², and is given by:

$$\text{FoV} = \pi \left(\frac{\text{FWHM}}{2} \right)^2. \quad (1.1)$$

1.3 Importance of low frequency astronomy (LOFAR Key Science Projects)

LOFAR covers frequencies from 10 MHz to 250 MHz. As can be seen from Spectral Energy Distribution (SED) plot in the Figure 1.4, the radiation in this regime is from non-thermal synchrotron emission¹, for a star burst galaxy². Furthermore, the flux density of synchrotron radiation increases at lower frequencies (until effects such as synchrotron self absorption and ionization losses take over and reduce the synchrotron flux density) and hence, it gets easier to study the radiation from these low energy cosmic ray electrons. It is also interesting to note that low frequency radiation is produced by low energy electrons that have not been affected much energy loss. This includes the older electrons that have traveled farther from their point of origin, such as SNRs³. Therefore, they can help us study galactic disks and the halos of galaxies. In this section, the different Key Science Projects (KSPs) undertaken by the LOFAR community are explained.

¹We will visit this in section 1.3.1.

²This is somewhat different for other astrophysical soures (see Thompson et al. (2001), Figure 1.1)

³Low energy electrons are also present at the point of origin, while high energy electrons are *only* present close to their injection sites.)

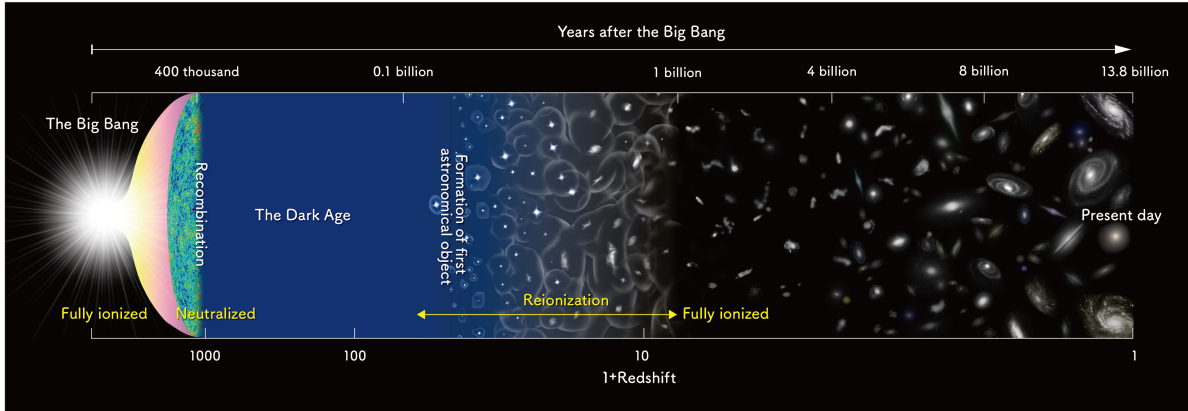


Figure 1.5: This is a schematic diagram depicting the lifetime of our Universe. At redshift $z \approx 1100$, the dark ages begin, and EoR begin at $z \approx 6 - 12$. Courtesy of National Astronomical Observatory of Japan (NAOJ).

Epoch of Reionization KSP: According to the Λ CDM model, there existed a stage 400,000 years after the Big Bang, when the Universe became transparent leaving only a relic radiation which we now call the Cosmic Microwave Background radiation. This era came to be known as the “Dark ages”, and happened when the ions and electron combined. It came to an end 400 million years later, when objects such as stars and Black Holes were formed, and assembled into proton-galaxies. This era came to be known as the “Epoch of Reionization”, or “Cosmic dawn”. Several questions still need to be answered about the formation of the Universe, such as what resulted in the end of the Dark Ages, and what gave rise to the EoR, and how are Black holes formed? One of the best ways to understand and answer these questions is by studying red-shifted HI 21 cm emission line using LOFAR core elements.

Surveys KSP: LOFAR can be used for large sky surveys owing to its large instantaneous field of view. These surveys can help us study high red-shifted galaxies (which will help us understand the formation and evolution of massive galaxies), clusters of galaxies (which will help us understand the characteristics of magnetic fields and CR acceleration) and cosmic star formation history of Universe.

Transients KSP: This entails the study of transients such as pulsars, Gamma-Ray Bursts, X-ray binaries, radio supernovae and flare stars. Due to LOFAR’s wide field and good sensitivity, it would help us do extensive time-domain studies, and discover new transient events.

Cosmic Rays KSP: The Cosmic Ray (CR) flux follows the simple power law: $\frac{dN}{dE} \propto E^{-\gamma}$. Hence, for energies above 10^{19} eV, only one particle per century per square kilometer reaches Earth. Hence, large effective areas are required to do proper statistics. At the energy of $\sim 5 \times 10^{15}$, γ changes from 2.7 to 3.1 in the CR spectrum, and is called the “knee” of the spectrum. After this “knee”, the composition of the CRs is not well known. This knowledge can be obtained with the help of LOFAR, which will help us understand the acceleration and propagation mechanisms, and figure out the universal acceleration process. One of the candidates for the acceleration process is the diffusive shocks in the radio lobes of radio galaxies. Furthermore, extensive research on air showers at ground level, can help us study new particle physics.

Solar KSP: Sun is an intense source of radio thermal emission, and gives rise to solar flares and Coronal Mass Ejections (CMEs) which can be studied with the help of LOFAR. Sun also has an effect on the space environments, and communication technology on earth, and hence, this project mainly aims to study the space weather and solar physics.

Cosmic Magnetism KSP: Magnetic fields are very important to understand the Universe. LOFAR, due to its wide bandwidth can help us do best precision studies of Faraday rotation and weak magnetic fields. With the help of Faraday tomography/ Rotation Measure (RM) Synthesis can help us obtain polarized radio synchrotron emission.

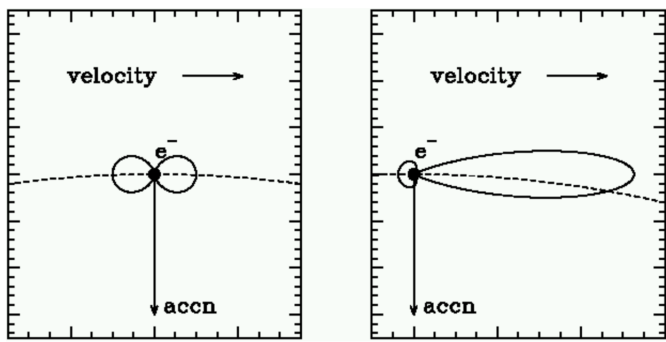


Figure 1.6: When an electron moves at relativistic speeds, the \sin^2 radiation pattern is Lorentz transformed. *Left:* The radiation pattern of a non-relativistic electron. *Right:* The relativistic radiation pattern. This image has been taken from <http://www.astro.utu.fi/~cflynn/astroII/14.html>

1.3.1 Astrophysical processes at Low Frequencies

At low frequencies, several astrophysical process are important. In the Figure 1.4, one can see the various process that become important at different frequency ranges. In the lower frequencies from around 10 GHz to 10 MHz, synchrotron emission is the dominant process. This process was first explained by a German astronomer named Karl-Otto Kiepenheuer in the year 1953. As the wavelength increases, the flux density of synchrotron emission increases. This helps us detect even the lowest intensity emission from the cosmic ray electrons. In this section, the numerous emission and absorption astrophysical processes that need to be taken into account whilst trying to explain the resultant emission at the frequencies that LOFAR detects are explained.

Synchrotron emission: When charged particles (mostly electrons) move around magnetic field lines at relativistic speeds, they emit photons. This emission of photons is called synchrotron emission and is non-thermal, as these relativistic electrons have a power law energy distributions:

$$N(E) dE = E^{-p} dE \quad (1.2)$$

Here, $N(E) dE$ is the number of electrons per unit volume in energy interval E and $E + dE$, and ' p ' is the electron spectral index. Let us consider a single electron (since synchrotron emission mostly comes from accelerating electrons), moving with velocity \mathbf{v} in a magnetic field \mathbf{B} . The electron energy is given by $E = \gamma mc^2$, where γ is the Lorentz factor and c is speed of light, and m is mass of electron. Its motion can be described by:

$$\frac{d}{dt}(\gamma m \mathbf{v}) = \frac{e}{c}(\mathbf{v} \times \mathbf{B}) \quad (1.3)$$

If we resolve \mathbf{v} into components parallel and perpendicular to the magnetic field represented as \mathbf{v}_{\parallel} and \mathbf{v}_{\perp} , then \mathbf{v}_{\parallel} remains constant with respect to time, and $\frac{d\mathbf{v}_{\perp}}{dt} = \frac{e}{\gamma mc} (\mathbf{v}_{\perp} \times \mathbf{B})$. The electron thus moves in a helical path centered at the magnetic field lines. The pitch angle, θ , of the trajectory of electron can be easily obtained from the velocity components. The angular gyro-frequency is given by the equation:

$$\omega_g = \frac{e\mathbf{B}}{\gamma m} \quad (1.4)$$

From the Figure 1.6, we can see that the electron will radiate in the Lorentz transformed beam pattern, and the forward power is in the beam of the angle $\frac{2}{\gamma}$. The full derivation of the emission spectrum for a single electron can be seen in Longair (2011). Here, I have merely written down the final equation. I_{\parallel} and I_{\perp} represent the polarizations of the emission and T_r represents the period of the electron in orbit.

$$j(\omega) = \frac{I_{\parallel} + I_{\perp}}{T_r} = \frac{\sqrt{3}e^3 \mathbf{B} \sin\theta}{8\pi^2 \epsilon_0 c m} \quad (1.5)$$

Here, $F(x) = x \int_x^{\infty} K_{\frac{5}{3}}(z) dz$ where $K_{\frac{5}{3}}$ is the modified Bessel function of the order $\frac{5}{3}$ and $x = \frac{2\omega a}{3c\gamma^3}$. c is the speed of light and m is the mass of the particle. From this equation, one may find the emission from a population

of electrons which is seen in synchrotron emission. For the distribution of electron described earlier, the total emission for electrons with a constant pitch angle can be given by:

$$J(\omega) \propto \kappa B^{\frac{(p+1)}{2}} \omega^{-\frac{(p-1)}{2}} \quad (1.6)$$

Hence, the spectral index of synchrotron emission is represented as α and is equal to the power on the omega function.

Free-free emission: Another process that is important at lower frequencies, is the free-free emission. Deceleration of electrons due to the presence of a charged particle results in thermal emission⁴, which is termed as free-free emission or Bremsstrahlung (from the German words ‘bremsen’ - to brake and ‘strahlung’ - radiation). The energy/frequency of the proton depends upon the loss in kinetic energy of the particle ($h\nu = E - E'$). This process usually is seen in an ionized gas medium, such as an H II region. It results in the steepening of the spectra, however, at such long wavelengths, its effects are severely diminished due to the presence of the steep synchrotron spectrum.

Absorption processes: For every emission process, there should exist an absorption process, according to the Principle of Detailed balance. These absorption processes usually take place in the star forming regions, while the regions with less electron density have a steeper spectra and are not affected by these effects.

- *Synchrotron self-absorption* The brightness temperature of a particle in Local Thermodynamic Equilibrium (LTE) cannot exceed its kinetic temperature. If a synchrotron source has a Maxwellian energy distribution (in LTE), then the synchrotron self-absorption prevents the particles from attaining the brightness temperature greater than the particle temperature.
- *Free-free absorption* If an electron absorbs a photon when moving near an ion, it is called free-free or thermal absorption. This absorption usually takes place in H II regions which are in Local Thermodynamic Equilibrium.

One could use Kirchhoff’s law to obtain the absorption co-efficient, which is given by:

$$\kappa_\nu = \frac{\epsilon_\nu}{B_\nu(T)} = \frac{\epsilon_\nu c^2}{2kT\nu^2} \quad (1.7)$$

Here, ϵ_ν is the emission co-efficient, k is Boltzmann constant. T is the temperature of the H II region and c is the speed of light.

$$\epsilon_\nu \propto \ln\left(\frac{A}{\nu}\right) \quad (1.8)$$

where $A = \frac{m_e}{2\pi Z e^2}$ (after several approximations). m_e and $Z e$ is the mass of electron and the charge of the ion respectively.

Hence, one can use the numerical approximation of $\kappa_\nu \propto \nu^{-2.1}$ to understand the dependence of frequency on the absorption coefficient. The total opacity, τ_ν is the integral of the coefficient of absorption along the line of sight (los):

$$\tau_\nu = \int_{\text{los}} -\kappa_\nu ds \quad (1.9)$$

The flux density of the source is given by:

$$S_\nu \propto \frac{2kT\nu^2}{c} \tau_\nu \quad (1.10)$$

At very high frequencies, the opacity $\tau_\nu \ll 1$, and the H II regions are almost transparent. However, as the frequency becomes lower, the total opacity increases. The region becomes opaque and its spectrum approaches that of a black body, as can be seen in the Figure 1.7. When the total opacity $\tau_\nu \approx 1$, the slope is seen to have the turn over (it changes from -0.1 to $+2$). Thermal absorption thus results in the flattening of the spectrum of a galaxy at extremely low frequencies. Thermal absorption thus results in flattening of the spectrum of a galaxy with high star formation rate, the total opacity approaches the value of 1 at much

⁴Thermal emission is produced by a source whose emitting particles are in local thermodynamic equilibrium (LTE).

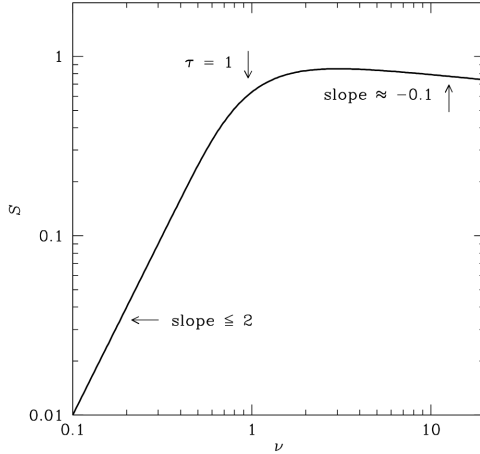


Figure 1.7: The radio spectrum of an ideal HII region. Here, thermal emission and absorption process are dominant, because an HII region is in LTE. At low frequencies, the slope is 2.0, while the slope at higher frequencies is around -0.1. At the total opacity of around 1, the turn over occurs. This is when free-free absorption is seen to dominate. This image has been taken from <https://www.cv.nrao.edu/course/astr534/FreeFreeEmission.html>.

higher frequencies than galaxies with low star formation. A numerically feasible equation to obtain the total opacity is given by the Equation 1.11.

$$\tau_\nu \approx 3.28 \times 10^{-7} \left(\frac{T_e}{10^4} \right)^{-1.35} \left(\frac{\nu}{\text{GHz}} \right)^{-2.1} \left(\frac{\text{EM}}{\text{pc/cm}^{-6}} \right) \quad (1.11)$$

Here, EM is the emission measure which is integral of the square number density of electrons along the los, and is given by the Equation 1.12. Here N_e is the electron number density.

$$\text{EM} = \int_{\text{los}} \left(\frac{N_e^2}{\text{cm}^{-3}} \right) d \left(\frac{s}{\text{pc}} \right) \quad (1.12)$$

With the help of turn-over frequency, i.e., the frequency at which the slope of the power spectrum in the HII region changes to 2 and optical depth τ_ν is 1, one may be able to obtain the value of EM, and thus obtain the electron density present along the line of sight. ν_{to} in the Equation 1.13 is the turn over frequency.

$$\text{EM} = 3.048 \times 10^6 \left(\frac{T_e}{10^4} \right)^{1.35} \left(\frac{\nu_{\text{to}}}{\text{GHz}} \right)^{2.1} \quad (1.13)$$

Loss processes Emitting cosmic ray electrons lose their energies in several ways, some of which are listed below:

- *Ionization loss* When a cosmic ray electron strikes a neutral particle, it may impart some of its energy to it, which may result in ionization, giving rise to an ion. These losses are seen in the nuclear regions of star burst galaxies, and result in the flattening of the spectral index.
- *Inverse Compton loss* When a cosmic ray electron with sufficiently high energy encounters a photon, its energy may be used to increase the energy of the photon. This may result in a photon going from X-ray regime to Gamma regime.
- *Adiabatic loss* Ultra relativistic particles e.g. in SNRs, may lose their internal energy during expansion and result in the dimming of synchrotron emission. This loss mechanism is termed as adiabatic.
- *Free-free loss* When a cosmic ray electron is decelerated in the presence of an ion, it loses some of its energy in form of a photon. The energy of the photon comes from the kinetic energy lost by the electron.

1.4 Image synthesis for interferometers

One of the first few interferometers used in astronomy was the Michelson Interferometer, which was used to measure the diameter of Betelgeuse (a star) (Michelson & Pease 1921). Most of the modern interferometers are

based on this interferometer. Over the years, interferometers have been used in various other fields fields, including Geophysics. In astronomy, interferometers have a special use- to obtain sky brightness distributions. In case of a single dish radio telescopes such as Effelsberg, the angular resolution is limited to:

$$\theta_S \propto \frac{\lambda}{d}$$

‘d’ being the diameter of the dish. However, for interferometers, the resolution depends as:

$$\theta_I \propto \frac{\lambda}{b}$$

‘b’ being the maximum baseline⁵ distance. Thus, the resolution is usually written as $\theta = \alpha \times \frac{\lambda}{D}$ rad, where D is the distance between the telescopes (in meters). Here α depends on the array configuration and the weighing scheme used during imaging. In reality, it also depends on the declination of the source. For LOFAR, the resolution varies between 0.5 deg to sub-arcsecs. Hence, the interferometer provides a very high resolution. An N-element interferometer obtains $N(N-1)/2$ number of visibilities⁶ simultaneously.

1.4.1 Interferometric concepts

In this section, I shall briefly explain the core concepts of an interferometer. A more detailed description can be found in [Thompson et al. \(2001\)](#). The formalism used in LOFAR and the mathematical explanation to obtain visibilities from the electronic voltages obtained from the antennae are explained in the Appendix.

Let us consider a basic two element interferometer, with \mathbf{B} as the baseline vector, and \hat{s} as the unit vector of the direction to an arbitrary source. The source is at a distance far from the interferometer, just like all the astronomical sources, such that the waves that reach the interferometer from the source are planar. The response of the interferometer can be assumed to have quasi-monochromatic response with the critical frequency $\nu_c = \frac{\omega_c}{2\pi}$.

From the Figure 1.8, one can see that the signal from the antenna 1 experiences a delay of $\tau_g = \frac{\mathbf{B} \cdot \hat{s}}{c}$

$$\tau_g = \frac{|\mathbf{B}| \sin \theta}{c} \quad (1.14)$$

The voltages output from the antennae 1 and 2 can be written as V_1 and V_2 respectively.

$$V_1 = V \cos(\omega_c t) \quad (1.15)$$

$$\Rightarrow V_2 = V \cos[\omega_c(t + \tau_g)] \quad (1.16)$$

These voltages are correlated using a complex correlator by multiplication followed by averaging over ‘integration time’.

$$V_1 V_2 = V^2 \cos(\omega_c t) \cos[\omega_c(t + \tau_g)] \quad (1.17)$$

$$= \frac{V^2}{2} \left[\underbrace{\cos \omega_c t}_{\text{constant term}} + \underbrace{\cos [\omega_c(t + \tau_g)]}_{\text{sinusoidal term (with respect to 't')}} \right] \quad (1.18)$$

Thus, the correlated term consists of one constant term, and one sinusoidal term that depends on θ . The sinusoidal term averages to zero, when $\langle V_1 V_2 \rangle$ is computed. Thus, we get:

$$\langle V_1 V_2 \rangle = \frac{V^2}{2} \cos \left(\frac{\omega_c |\mathbf{B}|}{c} \sin \theta \right) \quad (1.19)$$

The correlator response is dependent sinusoidally on the direction of the source. This implies that there may be a loss of data at some values of θ . Hence, a second correlation is done between outputs of the antennae with a $\pi/2$ phase delay on one of the outputs.

⁵**Baseline** is the vector covering the distance from one antenna to another.

⁶Explained in the next section

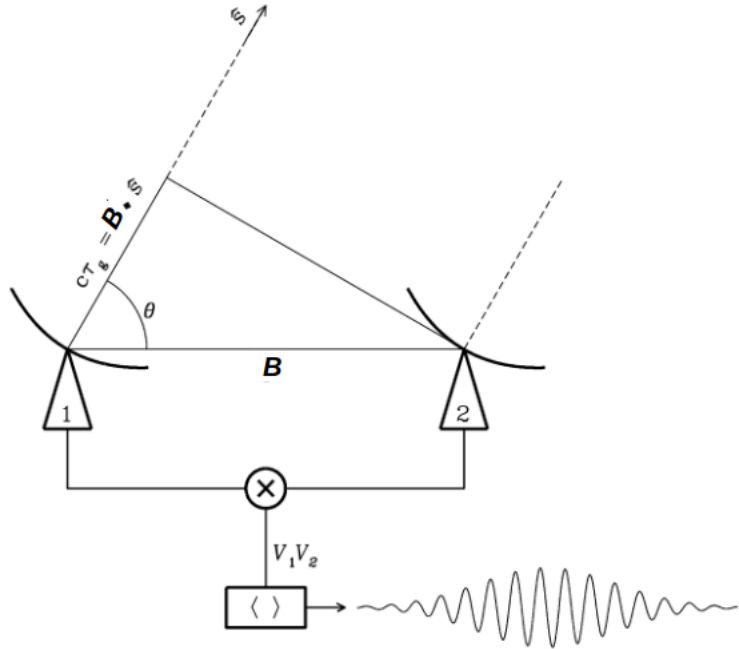


Figure 1.8: A two element interferometer observing an arbitrary source in the direction \hat{s} , with the baseline vector B . The two elements are represented as 1 and 2 with V_1 and V_2 as their respective visibilities. ‘X’ represents the correlator where the multiplication and averaging of the signal takes place.

1.4.2 UVW coordinate system

The UVW system is used in radio interferometry due to its feasibility of use. It is expressed with a reference direction of ‘phase center’ which remains fixed to the sky, and is often in the same direction of the delay centre⁷. This system is a right handed Cartesian coordinate system. U and V are on a plane perpendicular to the phase centre with U in the East West direction and V in the North South direction, as can be seen in the Figure 1.9. W is in the direction of the phase center. Usually, the coordinates are expressed in terms of the wavelength of the observation.

$$(u, v, w) = \frac{B}{\lambda} = \vec{B}_\lambda$$

The UV visibilities are obtained consecutively in time, which makes the baseline vector to rotate in the UVW plane. Thus, the UV coverage is the set of uv values for which the visibilities are obtained. LOFAR visibilities are stored in MeasurementSet format, in which the (u,v,w) data is stored in meters, thus preventing the confusion between various frequency channels in the observation.

1.4.3 Calibration techniques used for LOFAR calibration

LOFAR calibration used the RIME formalism, which is explained in detail in the Appendix. With the help of the Van Zitter Zernike theorem, the true visibilities for an image can be obtained. While this may seem simple enough, there are several challenges that come with synthesis of an image. The true visibility is corrupted by antenna based effects such as atmospheric attenuation, variable pointing offsets, variable delay offsets, electronic gain, delay and phase changes. It may also be corrupted by baseline based effects such as radiometer noise, correlator malfunctions and RFI. Some of the methods to circumvent the problems are discussed below:

⁷

$$\text{Fringe washing function} = \text{sinc}(\pi\tau_g \Delta \nu) = \frac{\sin(\pi\tau_g \Delta \nu)}{\pi\tau_g \Delta \nu} \quad (1.20)$$

$$\Rightarrow \quad \langle V_1 V_2 \rangle = \frac{V^2}{2} \cos(\omega_c \tau_g) \text{sinc}(\pi\tau_g \Delta \nu) \quad (1.21)$$

It diminishes the interferometer response. Thus, one may choose the direction in which the Fringe washing function is zero, called the **delay center**.

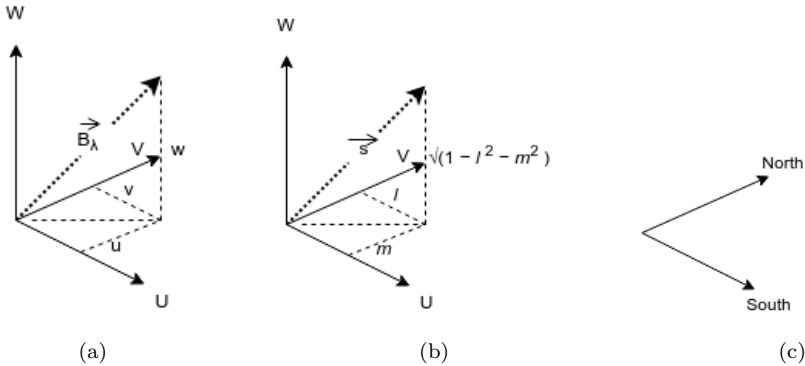


Figure 1.9: The UVW coordinate system. *Left:* The (u,v,w) coordinates, along with the directions. The \vec{B}_λ represents the direction of the source in UVW coordinate system. *Middle:* The (l,m) coordinate system on the image plane, which is visited upon again section A.1. *Right:* The Earth EWNS directions.

Convolutional gridding: To synthesise an image from the UV data, one first has to transform the non-uniformly sampled UV-plane into a uniformly sampled UV plane. This is done with the help of convolutional gridding. The data is first convolved with a appropriate function (such as a SHAH function) so that a uniform UV grid can be generated. This is followed by the IFFT and an element by element division is done on the image plane intensity. This generates the ‘dirty image’, which is then deconvolved to give a clean image.

W-projection: In case of a small field of view, the w -term can be neglected. However, this cannot be done in the case of LOFAR. One of the methods to take care of this term is the w -projection algorithm, in which a visibility sample is projected onto a $w=0$ plane so the effects of the term get nullified. This is followed by the convolutional gridding to obtain the image (Cornwell et al. 2008). Another algorithm is the w -stacking algorithm in which the correction is applied after the visibilities are gridded (Cornwell et al. 2012).

Direction dependent calibration: In LOFAR, the field of view is very large. This proves to severely affect the image of sources that are not point-like, for example, a galaxy like IC 342. This is because the total electron content is different for LOFAR in every direction in its field of view. As can be seen in the Figure 1.10, the variation of the TEC is explained for different array configurations.

In order to obtain better images, LOFAR calibration uses a method called facetting, in which the field of view is divided into smaller fields containing a strong source or a small group of sources with a high flux density. Some of the higher flux density objects have enough Signal-to-Noise (S/N) to calibrate themselves, to obtain a better image. Thus, self-calibration is performed using these strong sources. Using the method of self-calibration, the sensitivity of the image can be greatly improved. Sometimes, the increase in effective S/N may even be an order of magnitude better. Hence, a better gain calibration can be done with just an approximate source image, to give a much better final image of the source.

1.4.4 Overview of imaging procedure for LOFAR

In this section, a brief overview of how the data from the CEP cluster is imaged is given. The pipeline and the procedure I have used my differ slightly from the procedure given in this section.

The data from the CEP clusters is in the form of measurement sets. This data undergoes **pre-processing**. In this stage, the data is flagged in both time and frequency domains (even averaging of data may be done in both domains at this stage, if need be). After this, demixing is done. This is the subtraction of the brightest sources in the low frequency sky (the A-team⁸). A round of initial calibration is applied, which is done using a standard flux calibrator reference source. Then an initial phase calibration is performed. The Local Sky Model (LSM) used for this is obtained from the Global Sky Model (GSM). This uses 4 major catalogues: VLA Low-frequency Sky Survey (VLSS) (Lane et al. 2012), Westerbork Northern Sky Survey (WENSS) (Rengelink et al. 1997), the NRAO VLA Sky Survey and (NVSS) (Condon et al. 1998) and the Multifrequency Snapshot Sky Survey (MSSS) (Heald et al. 2015). For removing any remaining RFI/ noise, another round of flagging and filtering is done.

After the pre-processing of the data, the **imaging** procedure is started. The non-coplanarity effects (the w term

⁸Cassiopeia A, Cygnus A, Taurus A, Virgo A, Hydra A, and Hera A

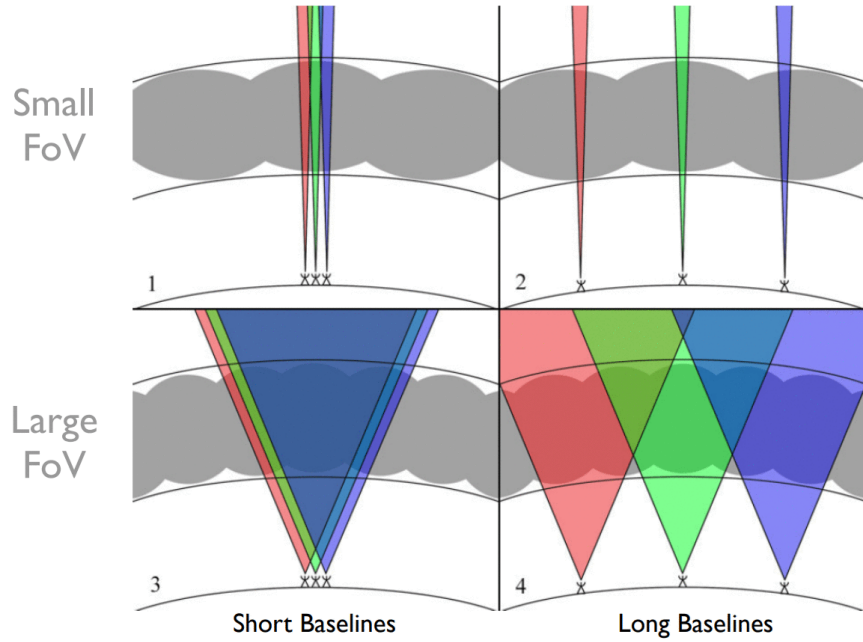


Figure 1.10: LOFAR is represented by three antennas at ground level. The ionospheric electron density structure (grey bubbles) are shown, with the various fields of view shown in (red, green and blue areas). For antennae like VLA, the primary beam patterns, shown in regimes 1 and 2, each individual antenna has the field of view in which the TEC stays approximately the same. The primary beam patterns in LOFAR are more like the ones shown in regimes 3 and 4. The TEC along the line of sight in the field of view has variations. In regimes 1 and 3, the relatively compact array configurations are shown. The TEC variation across the array for a single viewing direction within the FoV is approximately a gradient. In regimes 2 and 4, relatively extended array configurations are shown. The TEC variation varied significantly for the fields of view in such configurations. This image has been taken from [Intema et al. \(2009\)](#), where a very good description of the calibration techniques is given.

of the equation A.9) are removed using an algorithm, especially when doing wide field imaging. This is followed by taking care of the antenna primary beam variations which depend on the time, frequency and polarization. After this, a source finding algorithm is used to generate an updated LSM. Finally, a final round of flagging, imaging and LSM model updating is done. The final image products are then made available in the LTA.

Chapter 2

Imaging

In this thesis, we have imaged two galaxies- IC 342 and NGC 628, using the HBA data.

2.1 NGC 628

NGC 628 is an almost face-on grand design late-type spiral galaxy. It is located at a distance of almost 7.3 Mpc ([Karachentsev et al. 2004](#)). Details on the galaxy can be found in the Table 2.1. It has two clearly defined spiral arms that can be seen in any optical image of the galaxy. In the UV, the spiral arms can be seen as bright knots on diffuse emission ([Marcum et al. 2001](#)), and these knots are also traced in the H α . It is an isolated galaxy, and does not have strong density waves. HI holes have been detected in the HI layer of the galaxy, with sizes ranging from 0.24 kpc to 2 kpc [Bagetakos et al. \(2011\)](#). The galaxy is seen to consist of two disks, the inner disk being 8-10 kpc. These regions span different type of stellar populations [Natali et al. \(1992\)](#), with a colder inner region [Ganda et al. \(2006\)](#), and faint H II regions covering the outer part of the galaxy ([Ferguson et al. 1998](#)). The H I distribution is seen to be extended and asymmetric to the southwest. In [Kamphuis & Briggs \(1992\)](#), it was seen that the inner part of the galaxy has a flat differentially rotating disk while the outer part is not a “well-behaved” disk. In [Martini et al. \(2003\)](#) it was concluded that the inner part of the galaxy has no dust lanes, while outer part of the galaxy has clear nuclear dust spirals.

2.2 IC 342

IC 342 is an intermediate, almost face-on spiral galaxy of the Maffei 1/IC 342 group, the galaxy group nearest to our Local group, at a distance of around 3.3 Mpc([Karachentsev & Kashibadze 2006](#)). Details on the galaxy can be found in the Table 2.2. There has been a great amount of interest in the study of the galaxy, as it has a structure most similar to our own galaxy with similar dynamical mass ($2 \times 10^8 M_{\odot}$) ([Turner & Hurt 1992](#)). The super massive black hole mass at the center of IC 342 is also of the same order ($\sim 10^6 M_{\odot}$) as Milky Way. It is only 10.6 deg above the galactic plane, and is not clearly visible because of the Galactic disk and the large number of foreground stars in optical regime. It is the third largest spiral galaxy in the sky, with an angular size of . It consists of a central nuclear star cluster, where a lot of the star formation occurs. There exist five prominent Giant Molecular Clouds (GMCs) in the molecular ring and the arms, each of the mass of approximately $10^6 M_{\odot}$ ([Downes](#)

Distance ¹	~7.3 Mpc
Position ²	RA:01h36m41.74s DEC:+15d47m01.1s
Morphology ³	SA(s)c
Star Formation Rate ⁴	1.21 M_{\odot} /year
Inclination angle- inner disk (deg) ⁵	7
Inclination angle- outer disk (deg) ⁶	13.5
Position angle (deg) ⁷	02

Table 2.1: Parameters of NGC 628

Position ⁹	RA:03h46m48.503s DEC:+68d05m46.92s
Distance ¹⁰	~3.3 Mpc
Morphology ¹¹	SAB(rs)cd
Star Formation Rate ¹²	2.8 M_{\odot} /year
Inclination angle (deg) ¹³	30
Position angle (deg) ¹⁴	39.4
B _T (mag) ¹⁵	9.16

Table 2.2: Parameters of IC 342

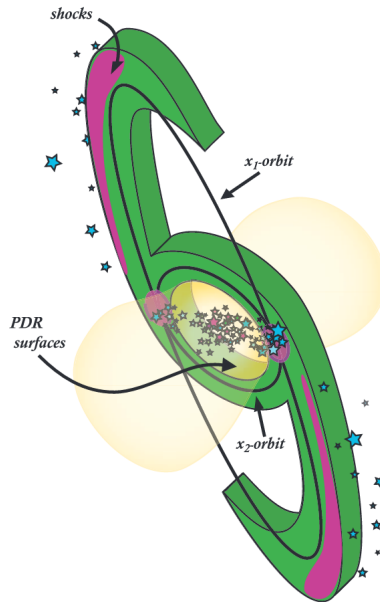


Figure 2.1: Schematic of the chemical and physical structure of the nucleus of IC 342 (Meier & Turner 2005)

(et al. 1992). The nucleus of the galaxy consists of two mini-spiral arms that are connected to the inner molecular ring. This structure is seen due to the presence of barred potential, which is also indicated by the morphology of the velocity residuals⁸ which showed the presence of a large bipolar structure (Ewen & Purcell 1951). The outer part of the galaxy can be seen to have four distinct arms, with the inner part having speeds up to $38 \pm 7 \text{ km s}^{-1}\text{kpc}^{-1}$ and the outer part ($\sim 5 \text{ kpc}$ from center) having a speed of around $11 \pm 6 \text{ km s}^{-1}\text{kpc}^{-1}$ (Meidt et al. 2009). Photo-dissociation Region (PDR) is present within the central 400 pc of IC 342 (Schulz et al. 2001). The physical and chemical geometry can be best understood from diagram 2.1 of IC 342. The yellow regions represent the H II regions. The star formation in the nuclear region was studied using Radio Recombination Lines (RRLs) and continuum emission at C-band and Ka-band with the JVLA, and two components were resolved lying east and west of the central star cluster, which were associated with two GMCs. It was predicted that several compact H II regions provide best fit for the two regions (Balser et al. 2017). It is at a low inclination of 31 deg, according to the HI kinematic data, which also indicates the counter-clockwise rotation of the galaxy (Ewen & Purcell 1951), assuming trailing spiral arms. With the help of H II and S II filters, 16 Supernova Remnants were identified, most of them being near or in the H II regions and two of them isolated (Dodorico et al. 1980). IC 342 is also the host of four Ultra Luminous X-ray sources (ULX) (Rana et al. 2015).

Being an axis symmetric spiral (ASS), over the years, magnetic fields in this galaxy have been studied at several wavelengths- 6.2 and 11 cm (Graeve & Beck 1988), at 20 cm (Krause et al. 1989). Recently, Faraday tomography of the local ISM with LOFAR, in (Van Eck et al. 2017), showed the presence of two Faraday thin neutral clouds clearly separated in Faraday depth. In this thesis, we have also studied the polarized sources in the field of view of the galaxy at frequencies as low as 150 MHz. More information about the magnetic fields in IC 342 can be found in section “Magnetic fields” chapter.

⁸Subtracting the rotation model with the observed velocities gives the residual velocities

Start date (UTC)	22-Nov-2013 / 15:19:00.0
End date (UTC)	23-Nov-2013 / 00:50:59.9
Interleaved calibrator	3C48
Scan length on calibrator	2 min
Scan length on target	20 min
Duration of observation	9 hours 32 min
Final time on target	8 hours (24 scans)
Frequency range (from Pre-factor)	110.667-179.027 MHz
Frequency range (for Factor)	110.667-169.239 MHz
Total bandwidth on target	68.36 MHz
Final bandwidth in target	58.57 MHz

Table 2.3: Parameters of NGC 628

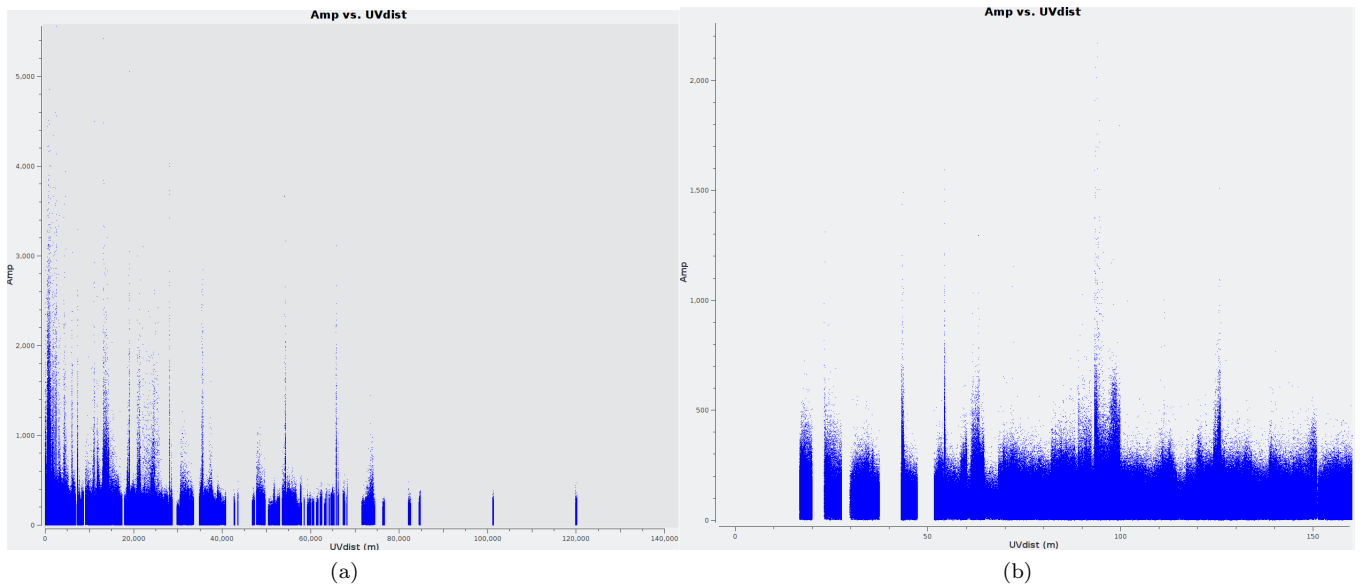


Figure 2.2: This was the arrangement of baselines used for the observation. This is a plot generated by task in CASA called 'plotms' for the first measurement set for the frequency 111 MHz in the first time step. From the plot, one can see the baselines used in terms of meters. As can be seen, the observation uses a dense core to image diffuse flux in the galaxy-the disk and the halo parts. *Right:* This image shows the shorter baselines used. The shortest projected baseline used was around 23 m.

2.3 Observational setup

NGC 628: The observations for NGC 628 were done in an interleaved mode. The calibrator used was 3C 48, and the scans were alternatively taken from the target to the calibrator. The observation used 14 remote stations and 23 core stations. The number of stations used for the observation of NGC 628 was 37. No international stations were used. Details of the observation can be found in the table 2.3. The baselines used for the observation can be seen in Figure 2.2 that shows the UV distance in meters and amplitude plot.

2.4 Calibration of LOFAR data

Calibration in LOFAR is especially difficult due to the ionosphere that causes delay differences between antenna stations. This gives rise to additional phase errors in the visibilities that vary station to station due to LOFAR's large array size. This phase depends on two factors: (1) Free electron column density along the line of sight, (2) Frequency being observed. Another aspect to be noted while calibration of LOFAR is the station beam shape that varies with time and also, the difference between the beam model and the actual beam shape.

In order to take care of these effects, LOFAR data calibration involves two major parts. In this thesis, a tool called Factor¹⁶ was used. The major steps to the data reduction are explained below. An overview on how to use the tool itself is described in a later section 2.4.3.

2.4.1 Direction independent part

The first step to do direction independent calibration is the flagging of RFI (Radio Frequency Interference) with the help of **AOFagger** (Offringa et al. 2012). Then, the data is averaged using **NDPPP** to be 4s in time resolution and 4 channels per sub-band in frequency resolution, to reduce the size of the data. Then, all baselines with CS013 HBA station were flagged and a flux density scale was created for 3C 48 (which was chosen as the amplitude calibrator source) using the model that shows the flux density values of the source at several different frequencies, with a flux density of 64.76 Jy at 150 MHz, as described in Scaife & Heald (2012). Using this primary beam calibrator, the gain solutions are obtained using **BlackBoard Selfcal** (BBS) for all four correlations. The gain solutions are then transferred to the target(Pandey et al. 2009) data to correct for the instrumental effects¹⁷. The A team sources affect the visibilities through the side lobes of the station beam. Hence, the visibilities in which the contribution is more than 5 Jy (in apparent flux density) are flagged. This was followed by another round of flagging, and averaging. The data was concatenated into subbands with time resolution of 8 s. The width of each channel was kept at 48.828 kHz, and the total bandwidth was at 1.95 MHz. The last step in direction independent calibration involves the subtraction of sources by first subtracting clean components in medium resolution images, and then re-imaging the subtracted image at a lower resolution (1.5' and uv cut range of 2 kλ) and full field of view image [write dimensions here]. This is done in order to detect the extended flux emission and sources in the first and second side lobes. The new components found using the lower resolution image were again subtracted from the obtained visibilities. The clean components obtained from the two imaging steps in the direction independent part of calibration are convolved with the gain solutions and subtracted from the uncorrected visibilities and the obtained visibilities were used as input for the direction dependent calibration. Sky models for each frequency were generated (to take care of frequency dependence) which would be used in the later steps of factor.

2.4.2 Direction dependent part

From the Figure 2.6, it can be seen that the artifacts from brighter sources severely affects the image quality. Hence, in order to reduce the noise in the image due to ionosphere and the station beam effects, “faceting” is done obtain solutions and reach near-thermal noise limited images. The field of view is divided into a number of small isoplanatic patches called facets. We assume that the calibration solution towards the brightest source in the facet can be used for the facet as a whole.

For NGC 628: The visibilities obtained from prefactor were moved to the lofar4 cluster where the direction dependent calibration was to be done. The frequencies above 170 MHz were not taken for the next part, as they seemed to have bad visibilities. The first time step was also removed owing to corrupted visibilities. The first step to do DDE calibration is to make a list of the sources to make facets around. The sources above 100 mJy in

¹⁶<https://github.com/lofar-astron/factor>

¹⁷**Instrumental effects:** The clocks at the remote stations are not perfectly synchronized, which causes a phase delay. This in addition to the phase delay by the ionosphere gives rise to phase errors. The phase difference for a baselines can be written as:

$$\Delta \text{ phase}(\nu, t) = \underbrace{2\pi p_0(t)\nu}_{\text{Clock difference effects}} - \underbrace{\frac{8.448 \times 10^9 p_1(t)}{\nu}}_{\text{Total Electron Content (TES) effects}} [\text{rad}]$$

Here ν represents frequency and p_0 and p_1 represents the clock difference and TEC difference. These errors need to be removed. This is done with the help of a bright source with a high Signal to Noise ratio on all baselines. Brute force search is done to obtain clock and TEC initial guesses, as computing using the equation is not computationally feasible.

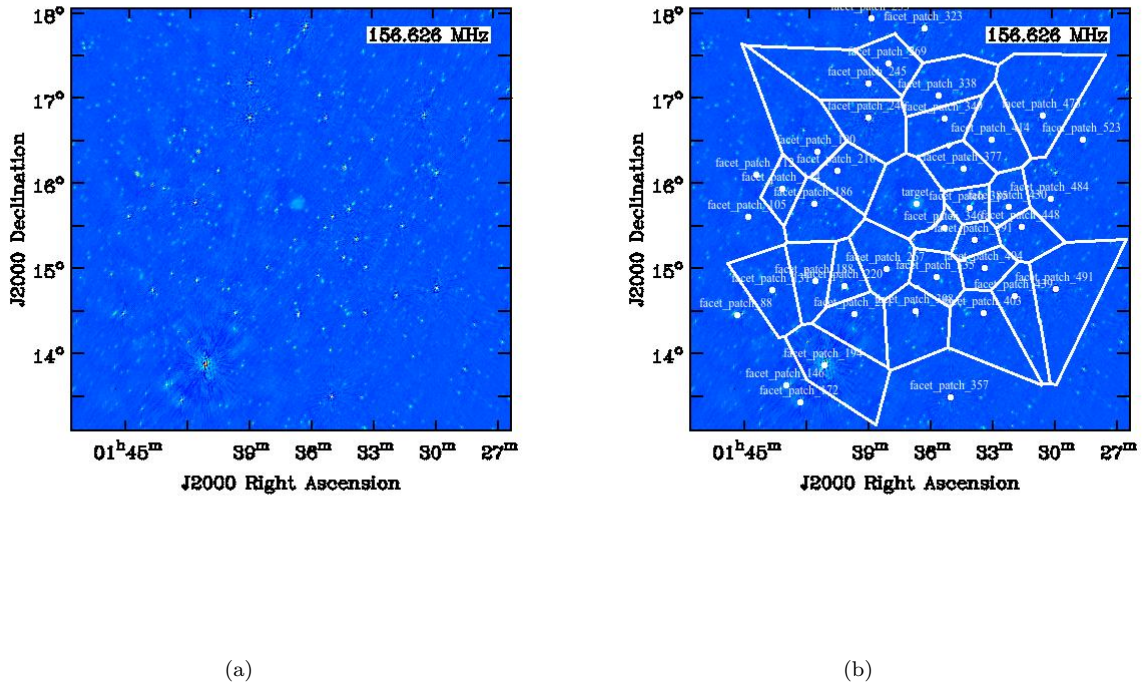


Figure 2.3: *Left:* Initial subtract image of NGC 628, using frequencies between 135 to 167 MHz. It has a restoring beam of 43.99 arcsec by 31.64 arcsec and position angle of -17.27deg. As can be seen, artifacts from individual sources, such as 3C 049 (at RA: 01h41m09.160s and DEC: +13d53m28.05s in J2000 coordinate system), can severely affect the galaxy image quality. Hence, the field of view is divided into “isoplantic” patches called “facets”. *Right:* The facet patches can be seen in the image, and are made around the radio sources present in each facet. They are represented by the white dots in the image on the right. The facet patches are based on the Veroni tessellation scheme.

apparent flux density were selected, with maximum size of $2.0'$. They were set to be separated by a distance of at least $7'$. In cases where more than one source was used as calibrators, the collective maximum flux was set to be 100 mJy. The faceting was done upto a radius of 2.8 deg ¹⁸. If any sources were found at a higher radius than that, a small patch was made around this part. One such source was 3C 047, a quasar, which is labeled as source 1 in the Figure 2.4. The boundaries for some of the sources had to be changed¹⁹ to get better self calibration results (to remove the secondary sources in the facet). The calibration begin with source 194- commonly known as 3C49. The self-cal images after each iteration of 3C49 is shown in Figure 2.5. To do the self- calibration, the source is first added back to the visibility data (the residual visibility obtained from DIE calibration), and phase shifted to the source in the facet, which in the fist case was 3C 49. This is followed by the “short-timescale phase +TEC” calibration to take care of the ionospheric delay (row 2 in the Figure 2.5). Then, to take the effects of the slowly varying station beam into account, the “slow gain” calibration is done. Then the imaging of the facet is done. Once the DDE calibration solutions for the facet are obtained, the other fainter sources within the facets are added back and corrected using the solutions of the strongest source that was used for the calibration. This is followed by the generation of an updated skymodel which is then subtracted from the residual visibilities with the obtained solutions. This whole process is then repeated for another facet that has the source with next highest flux density, so that the sources that have a higher calibration errors do not affect the DDE calibration of the fainter sources in other facets.

For IC 342: The Figure 2.7 shows the facets on the field of view of the observation, and the different directions in which the faceting was done. The sources above 300 mJy in apparent flux density were selected, with maximum size of $2.0'$. They were set to be separated by a distance of at least $7'$. In cases where more than one source was used as calibrators, the collective maximum flux was set to be 200 mJy. The faceting was done upto a radius of 1 deg , while the sources for the directions were set to be searched up to $7'$. A directions file was made by factor based on the given parameters. Then, a few changes were made²⁰ The rest of the procedure followed was mimicking the one for NGC 628.

2.4.3 Overview of Factor

This section gives the description of the steps to calibrate LOFAR data with the help of Factor. Imaging, for both IC 342 and NGC 628 was done on interleaved data-sets. Factor is used to produce deep images using the HBA data employing the direction dependent facet calibration method as described in (van Weeren et al. 2016). The first step to calibration, involves the preparation of the data, using a tool called Pre-factor²¹, which also does the **Direction independent calibration**.

Step 1: The data of the calibrator and target are kept in separate directories. The calibrator data is first processed using the Calibrator Pipeline. The gain solutions obtained using the calibrator are then used for the clock-TEC separation and to compute average gain amplitudes.

Step 2: The target data processing is done. This uses the Target Pipeline that adds the Rotation Measure correction from RMextract to the data file (h5parms) from the Calibrator Pipeline. This requires files that contain information about the ionospheric electron content. It also pre-process the input measurement sets (MSs) and applies the values from the h5parms. It predicts and flags the A-team contamination, and sorts the MSs by time and frequency into groups that are later concatenated. It removes the files with too much flagged data. It also does phase-only calibration on the skymodel. It also produces diagnostic plots, that can be seen in the table 2.4.
Step 3: The final part of Pre-factor is the “Initial subtract” pipeline that produces the sky-model required for Factor from the visibilities. Initial- subtract also gives the full field of view image. In our analysis, raw data was used (non-NDPPP-ed data: no demixing, averaging and flagging was done before-hand), which required the “Pre-Facet-Calibrator-RawSingle” parset (this option is not available in Prefactor anymore). The target part of the calibration was done in six batches due to the large size.

Once the data has been prepared using Prefactor, the **Direction Dependent calibration** is done.

Step 1: The Factor parset is prepared. In this, one can specify any additional flagging needed. One can also give instructions on the field in which faceting needs to be done, and the maximum size of facets and soures (or group

¹⁸This is by default at a value of $\frac{FWHM \times 1.25}{2}$ of the primary beam at the highest frequency.

¹⁹Sources 246, 385, 335, 349, 267, 253, 477, 144

²⁰The boundaries for some of the sources had to be changed to get better self calibration results (to remove the secondary sources in the facet). A few of the sources below the given flux density limit had to be given their own facets. There sources were marked with the prefix ‘d’, see Figure 2.7

²¹<https://github.com/lofar-astron/prefactor/wiki>

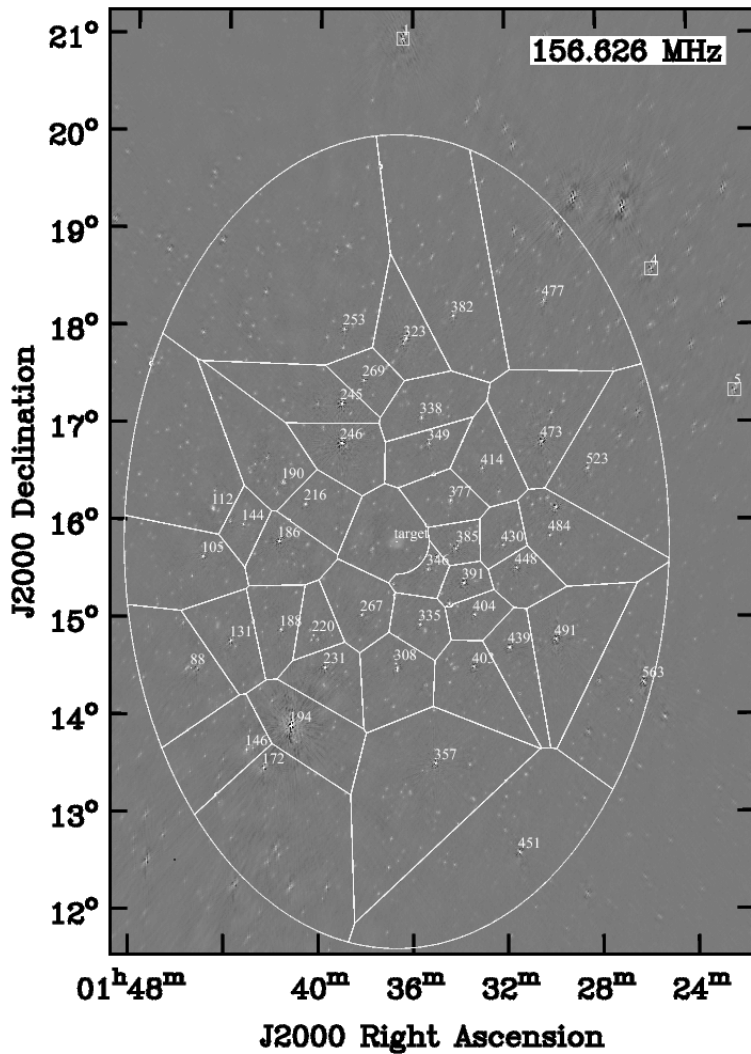


Figure 2.4: This image depicts the faceting scheme used for NGC 628. The middle facet marked “target” is NGC 628. The sources marked 1, 4 and 5 were included by hand due to their high fluxes. The image is the one obtained from the initial calibration (same as the one in the previous figure). The beam is elongated to account for the low elevation elongation of the LOFAR primary beam.

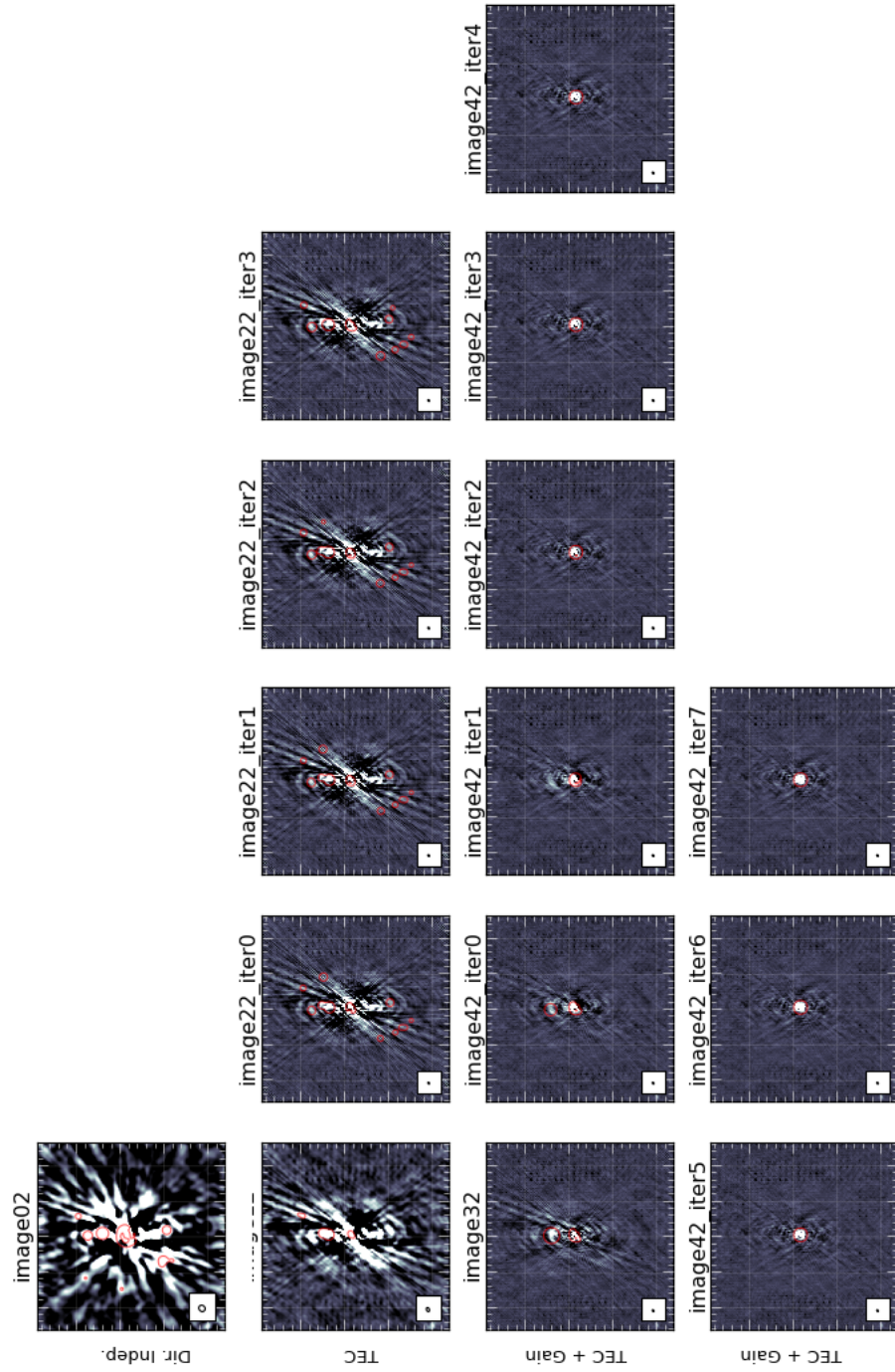


Figure 2.5: Self calibration images of the facet with source 194- otherwise known as 3C49. The image marked “Dir. Indep.” is the direction independent image of the facet. In the second row, the phase term is being solved, which took three iterations. Then, the phase + amplitude calibration was done, which took 7 iterations.

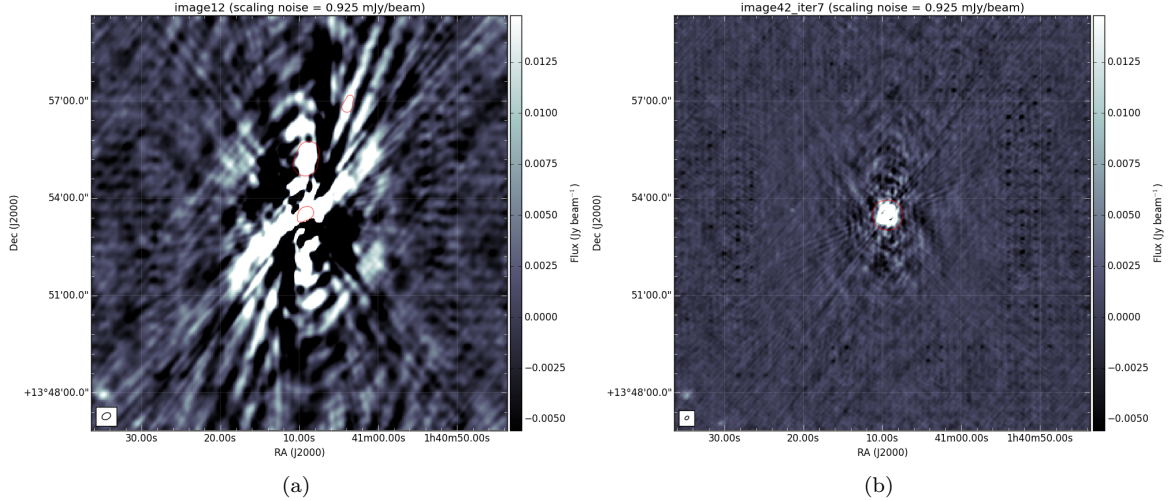


Figure 2.6: *Left:*The initial subtract image of facet containing the source 3C49. *Right:*Final self-cal image of 3C49. The image is considerably better than the one on the left, however some of the artifacts still remain. The source is the source is farther away from the target source, hence, the artifacts that remain do not affect the image too much.

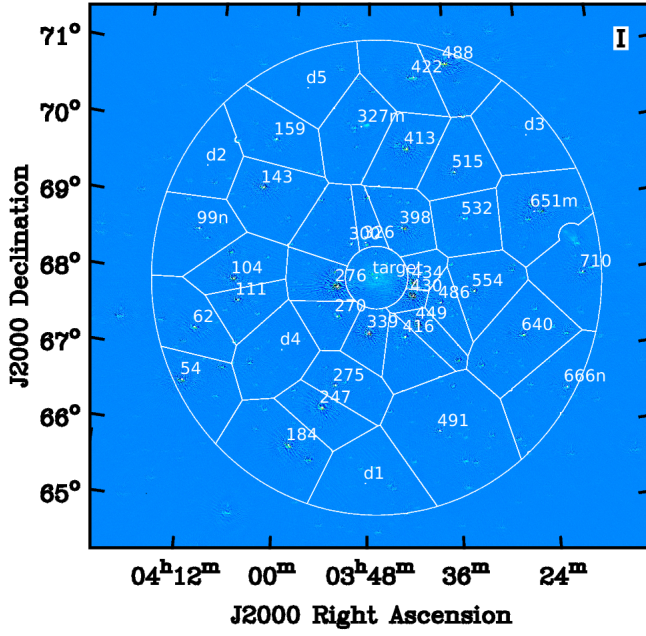
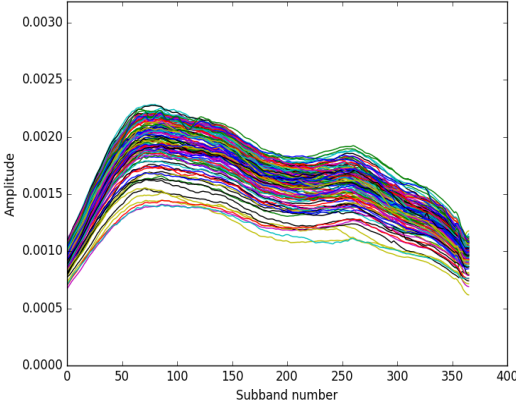
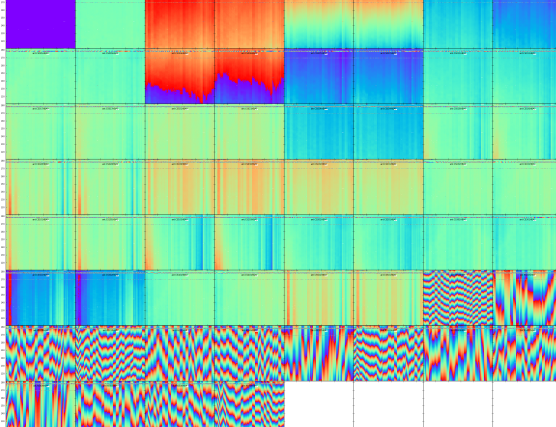
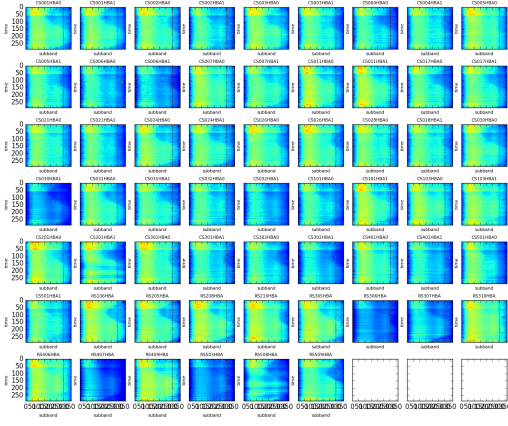


Figure 2.7: Faceting in IC 342 for Direction Dependent calibration in Factor. The facets have been overlaid on the image made using averaged Prefactor data. The resolution of the image is 17.35 by 12.72 arcsec. It was cleaned to a threshold of 0.3 mJy with Briggs weighting of -0.5.

of sources).

Step 2: The directions file can either be generated by Factor, or be edited by the user. One may also remove some of the directions, and add a few depending on what is needed. Factor is run using the command “runfactor”.

Step 3: One can check the progress of the Factor run, with the help of the command “checkfactor”. In Factor, various operations are simultaneously undertaken: Outliers and sources in each of the facets are peeled in the operations named “outlierpeel” and “facetpeel” respectively. This is followed by “facetselfcal” which self calibrates the facet calibrator. “facetsub” operation subtracts the model of the facet and calibrator. The imaging of the facet is done in the “facetimage” operation, in which the facet is imaged using full bandwidth, unlike in the “facetselfcal”, in which only part of the bandwidth is used to image the facet. If the full field of view image is required, it can be done using the “fieldmosaic” operation, in which all the final facet images are made into a mosaic, after the primary beam attenuation correction. The main output of Factor is generated in the “results” directory, which contains the self-calibrated visibilities and the self-calibrated images of the different facets.

Diagnostic plots	Description
	This graph shows the amplitude solutions in the different subbands. As can be seen, there are no clear outliers, showing that this data set does not have bad amplitude solutions.
	This plot shows the calibrator solutions in the YY polarisation. The CS001HBA0 station is flagged, and some of the frequencies between 170 to 180 MHz seem to have noisy data.
	This shows the waterfall plots of the amplitude solutions for the single stations. It can be used to see which stations are bad in the first plot.

Diagnostic plots	Description
	This plot shows the differential Total Electron Content (dTEC). It shows that the data is fine, even though it may be noisy.
	This plot shows the differential clock values. For all the core stations, the values should lie on 0.
	This plot gives the median difference of the phase solutions for the X and the Y antennas. For the station calibration, the X and Y dipole phases are not aligned with each other resulting in phase offsets. The blue spikes represent the ones that have been flagged by pre-factor.

Table 2.4: This table shows the diagnostic plots that are obtained as an output from the Prefactor pipeline. They give an overview of the condition of the data and help us select and flag any data sets that seem bad, and were not previously flagged by the pipeline.

Weighting	Description	Notes
Natural	Constant weights to all visibilities	Lowers the noise level Good to study point sources.
Uniform	Weights are inversely proportional to sampling density function	Noise can be a factor of two larger. Lowers side lobes.
Briggs	Compromise between Natural and Uniform weighting- defined by robust parameter (-2 to +2)	Good for diffuse source imaging. Robust parameter = -2 \Rightarrow Uniform weighting Robust parameter = +2 \Rightarrow Natural weighting

Table 2.5: The weighting schemes in imaging synthesis.

2.5 Imaging

Common Astronomy Software Application²² CASA is used to make images of the two galaxies, using the visibilities of the target facet. The LOFAR primary beam is much larger than the size of the galaxies, and hence, LOFAR primary beam correction was not done. Several images have been made with various weighting schemes and taperings. CASA gives an option of the ‘Robust’, which helps us choose the required weighting scheme. There exist three weighting schemes, as given in table 2.5. For more information, one can visit <https://casa.nrao.edu/docs/casaref/imager.weight.html>.

For IC 342 : One of the major problems encountered during the imaging of IC 342 is the presence of the source at RA: 03h47m28.8s and DEC: +68d08m23s, with a flux density of around 212 mJy/beam at 145 MHz. In the NVSS survey Condon et al. (1998), it has been defined as a radio source, as well as in the paper Baker et al. (1977). However, it is unknown as to what this source might be.

We can rule out the possibility of the source being a supernova remnant (SNR). For example, consider the SNR Casseopeia A. If the source were an SNR, its flux density should have a similar value as that of Cas A. The flux density of Cas A at a distance of around 3.4×10^3 pc would be around 1.24×10^4 Jy for the frequency of LOFAR (Fesen et al. 2006). This flux density value was obtained by extrapolating the flux density values in the NED database to 145 MHz frequency with a spectral index value of -0.93. We know that flux density scales as $\frac{1}{d^2}$, where d is the distance to the object. Hence, at that distance, the flux density of this SNR would be 0.011 Jy, much too low for the object in the image. For Crab Nebula, another SNR, this value is even lower $\sim 4.5 \times 10^{-4}$ Jy. Hence, we can conclude that this source must be a quasar or a radio galaxy. Also, there are four known SNR²³ present in the galaxy, which can be seen in the Figure 2.8 (Dodorico et al. 1980). None of these SNRs have a flux density as high as the one seen in the image for the source considered.

An attempt to get rid of the artifacts has been made by subtracting the source from the visibilities after obtaining them from Factor. However, there is no change from the previous attempts, as can be seen from Figure 2.9.

In the end, three images of varying resolutions are made. The noise of each image is obtained from the rms value of a region around a part of the image with no source. The images are made using the multi-scale clean technique. The Figure 2.10 is obtained using the visibilities from Factor. A brief summary of the image parameters are provided in the table 2.6. An outer tapering²⁴ of 14 arcsec by 9.5 arcsec has been applied. The image has a resolution of 12.48 arcsec by 10.26 arcsec, while the noise in the image is of the order of $390 \mu\text{Jy}/\text{beam}$. The Figure 2.11 uses the circular outer tapering of 22 arcsec. The image thus retrieved has a resolution of 25.93 arcsec by 23.26 arcsec, while the noise in the image is of the order of $560 \mu\text{Jy}/\text{beam}$. The image 2.12 uses an outer tapering of 37 arcsec. The noise in this image is of the order of $780 \mu\text{Jy}/\text{beam}$. The image has a resolution of 38.15 arcsec by 34.39 arcsec. All of these images have been made using the Briggs weighting scheme with a robust parameter of -0.5. A positive weighting scheme gave rise to peculiar artifacts in the image, and hence was avoided for this galaxy.

For NGC 628 : For NGC 628, the imaging is pretty straight forward. The target visibility data set is imaged using various weighting schemes. The galaxy is hardly visible at resolutions as high as 15 arcsec. Hence, all

²²<https://casa.nrao.edu/>

²³These SNRs have been detected by combining the images of the galaxy in H α and |S II| light. The emission nebulae have been sorted out with a low $\frac{H\alpha}{[SII]}$ line intensity ratio.

²⁴In CASA, one can provide a tapering of in the image plane by providing the FWHM. This is the kernel used to convolve the image, and thus obtain an image with the resolution similar to the measures given (in arcsec). One could also give the taper in terms of uv baselines, and these can be in kpc, or in λ , and the specified baselines would be flagged/‘tapered’ out

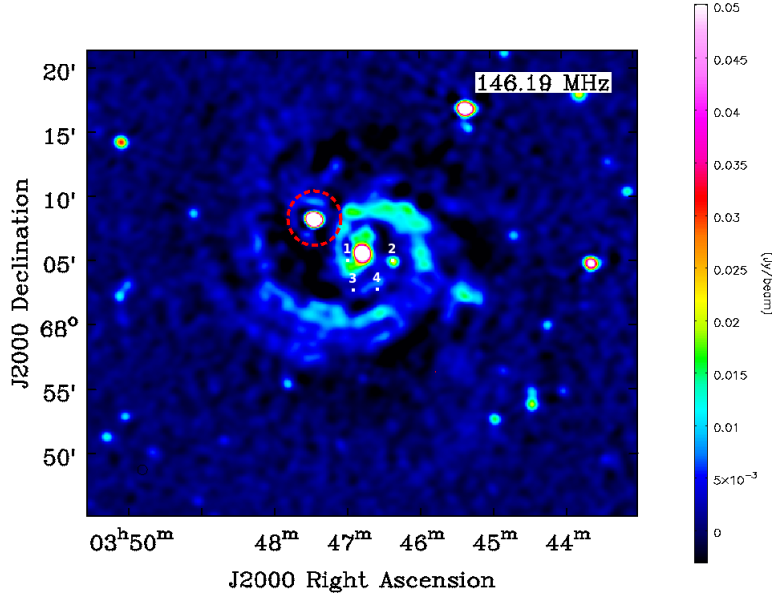


Figure 2.8: The four SNR candidates (labelled 1,2,3 and 4). The source in the dotted red circle cannot be a SNR because these SNRs do not have a flux density as high as the source.

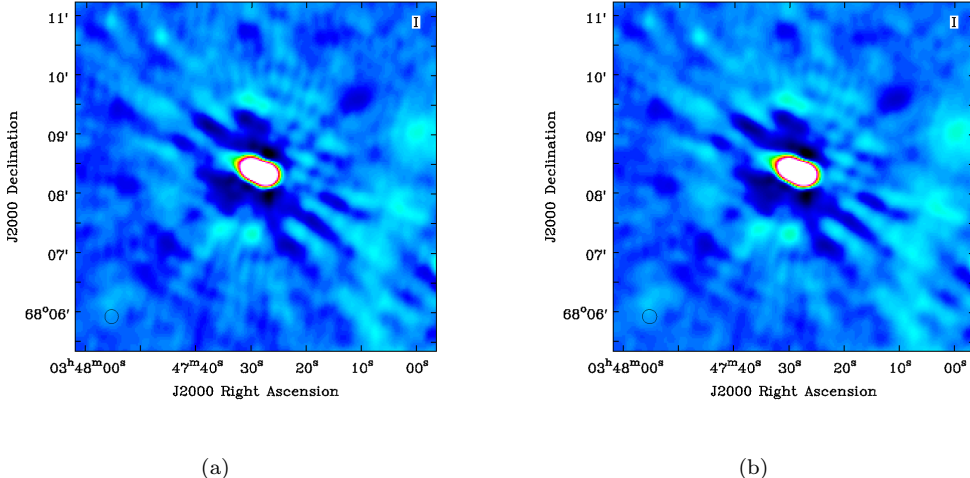


Figure 2.9: This image depicts the source that was a major problem in the imaging of IC 342, giving rise to several artifacts. The Figure on the left depicts the image in which the source has been subtracted while on the right, the source remains. There is little to no difference between the two and there is almost no change in the noise of the images. Hence, subtracting the source also provided no help.

Tapering	Robust parameter	Resolution (/beam)	Noise
14 arcsec by 9.5 arcsec	-0.5	12.48 arcsec by 10.26 arcsec	$390 \mu\text{Jy}$
22 arcsec (circular)	-0.5	25.93 arcsec by 23.26 arcsec	$560 \mu\text{Jy}$
37 arcsec (circular)	-0.5	38.15 arcsec by 34.39 arcsec	$780 \mu\text{Jy}$

Table 2.6: The parameters of the images for IC 342.

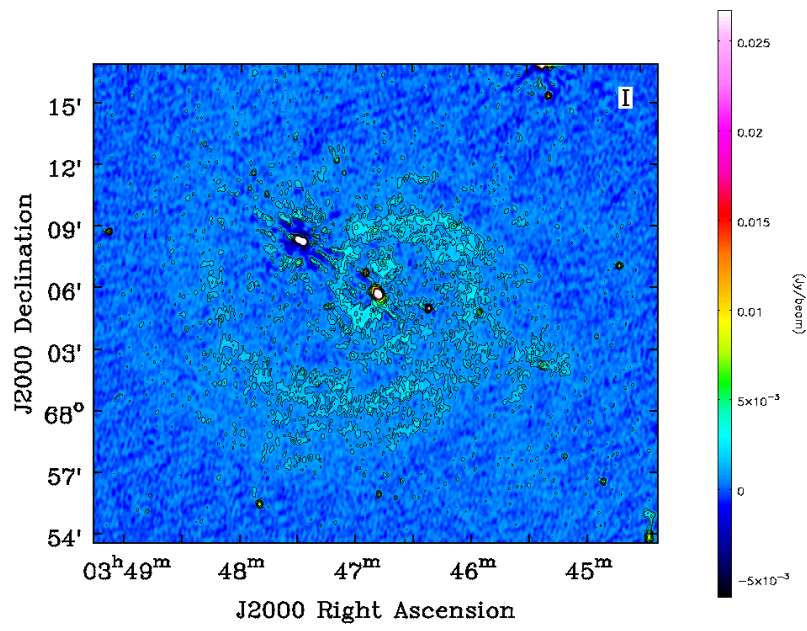


Figure 2.10: This is the LOFAR image of IC 342 at the central frequency of 146.2 MHz. Bandwidth of the observation was 62.5 MHz. This image has the resolution of 12.48" by 10.26"; PA: -8.10 deg. The contours are at 3, 8, 12, 18, 32 and 44×0.39 mJy/beam, which is the noise of the image in a quiet region.

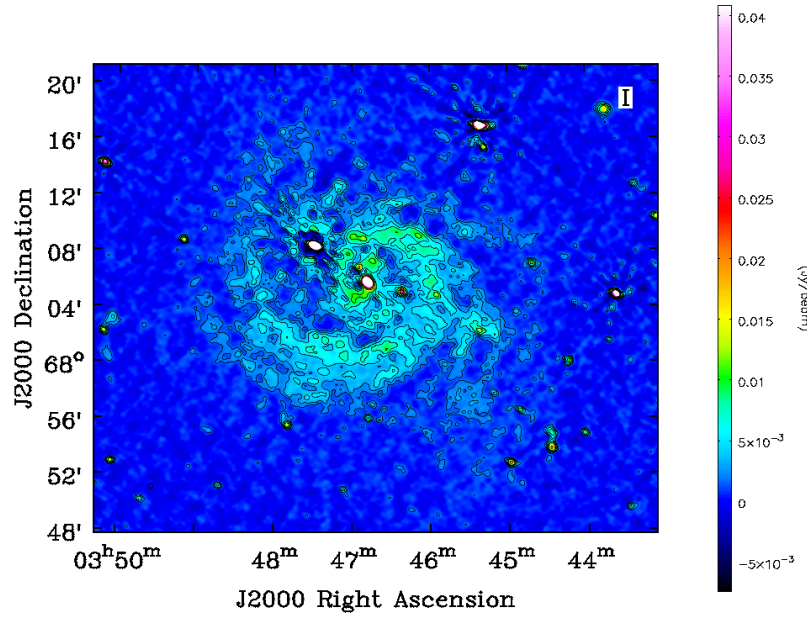


Figure 2.11: This image has the resolution of 25.93" by 23.26"; PA: 62.7 deg. The contours are at 3, 8, 12, 18, 32 and 44 × 0.56 mJy/beam, which is the noise level of the image.

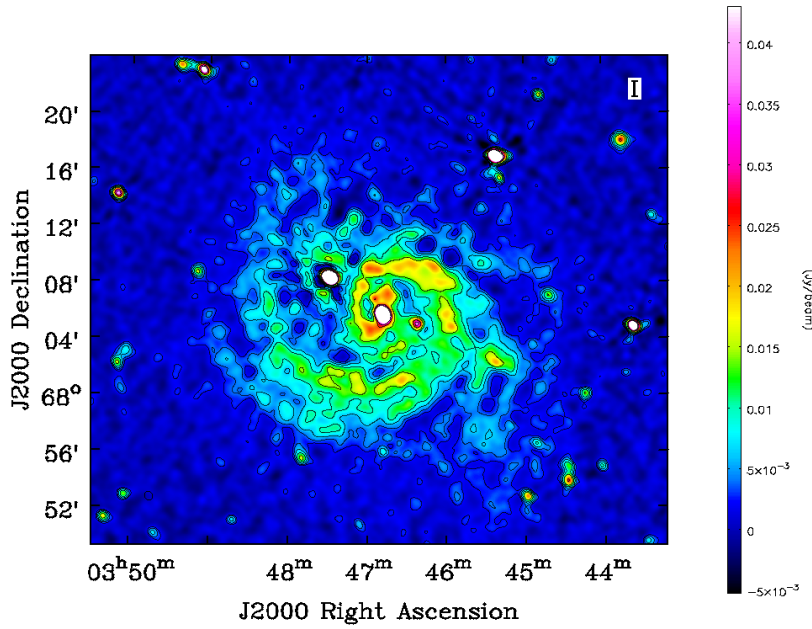


Figure 2.12: This image of IC 342 has the resolution of 38.15" by 34.39"; PA: 23.99 deg. The contours are at 3, 8, 12, 18, 32 and 44 \times 0.78 mJy/beam, which is the noise level of the image.

Tapering	Robust parameter	Resolution (/beam)	Noise
No taper	+0.5	20 arcsec	975 μ Jy
15 arcsec (circular)	-0.5	26.06 arcsec by 25.21 arcsec	1.04 mJy
35 arcsec (circular)	-0.5	40 arcsec	1.06 mJy

Table 2.7: The parameters of the images for NGC 628.

the images of the galaxy included in this thesis are of a lower resolution than that. A summary of these image parameters are given in the table 2.7. The Figure 2.13 is made using the robust weighting of +0.5. The noise in the image is of the order of 97 μ Jy/beam. The image originally made by casa with a resolution of 18.85 arcsec by 18.24 arcsec has been smoothed to a resolution of 20 arcsec with position angle of 180 deg. The Figure 2.14 is made using the robust weighting of -0.5, with an outer tapering of 15 arcsec. The resultant image has a resolution of 26.06 arcsec by 25.21 arcsec with a position angle (PA) of 88.26 deg, with the background noise of the order of 1.04 mJy/beam. The image 2.15 has been made with a Brigg's weighting of -0.5. Circular outer tapering of 35 arcsec has been used. The resultant image, with a resolution of 37.23 arcsec by 36.49 arcsec, has been smoothed to 40 arcsec with position angle of 180 deg. It has a noise level of the order of 1.06 mJy/beam. This has been made to take a look at the large scale structures.

Difference in noise level It is to be noted that the noise level of NGC 628 is much higher than that of IC 342. This may be because of several reasons, as listed below:

- NGC 628 is at a lower elevation than IC 342. LOFAR has less sensitivity at low elevations because at lower elevations:
 - * Dipoles have smaller gains
 - * Projected collecting area of the array is reduced
 - * Lower elevations implies longer paths length through the ionosphere

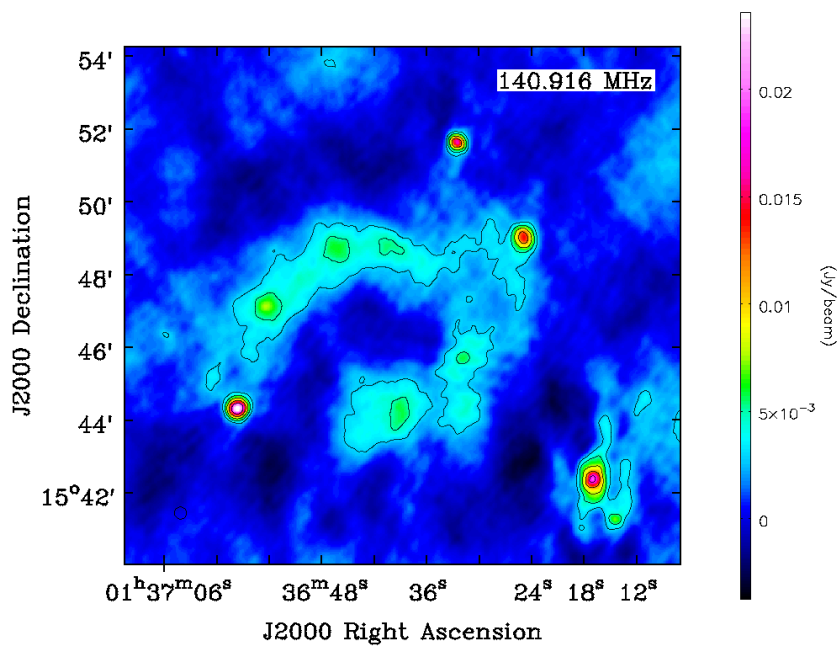


Figure 2.13: This image of NGC 628 has the resolution of 20''; PA: 180 deg. The contours are at 3, 8, 12, 18, 32 and 44×0.98 mJy/beam, which is the noise level of the image

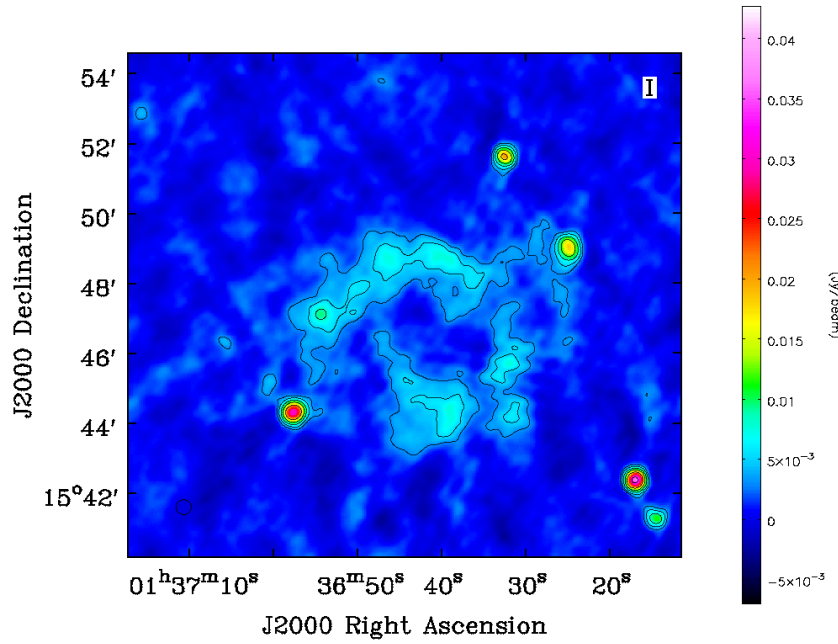


Figure 2.14: This image of NGC 628 has the resolution of 26.06'' by 25.21''; PA: 88.26 deg. The contours are at 3, 8, 12, 18, 32 and 44×1.04 mJy/beam, which is the noise level of the image

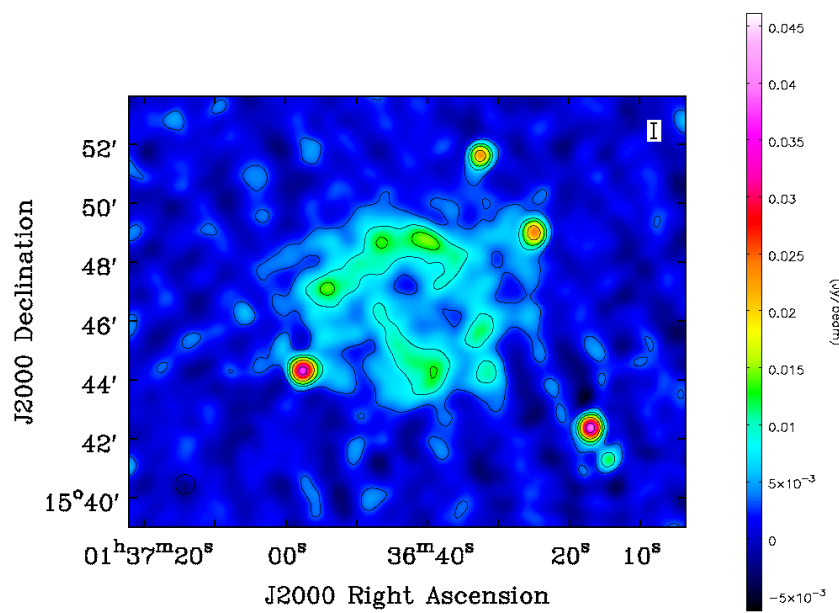


Figure 2.15: This image of NGC 628 has the resolution of 40"; PA: 180 deg. The contours are at 3, 8, 12, 18, 32 and 44 \times 1.06 mJy/beam, which is the noise level of the image.

- * larger separation of the ionospheric LOS of the calibrator sources.
- There was a higher level of ionospheric activity at the time of observation.
- There was a higher level of Radio Frequency Interference (RFI).
- Due to the interference from strong sources in the field.

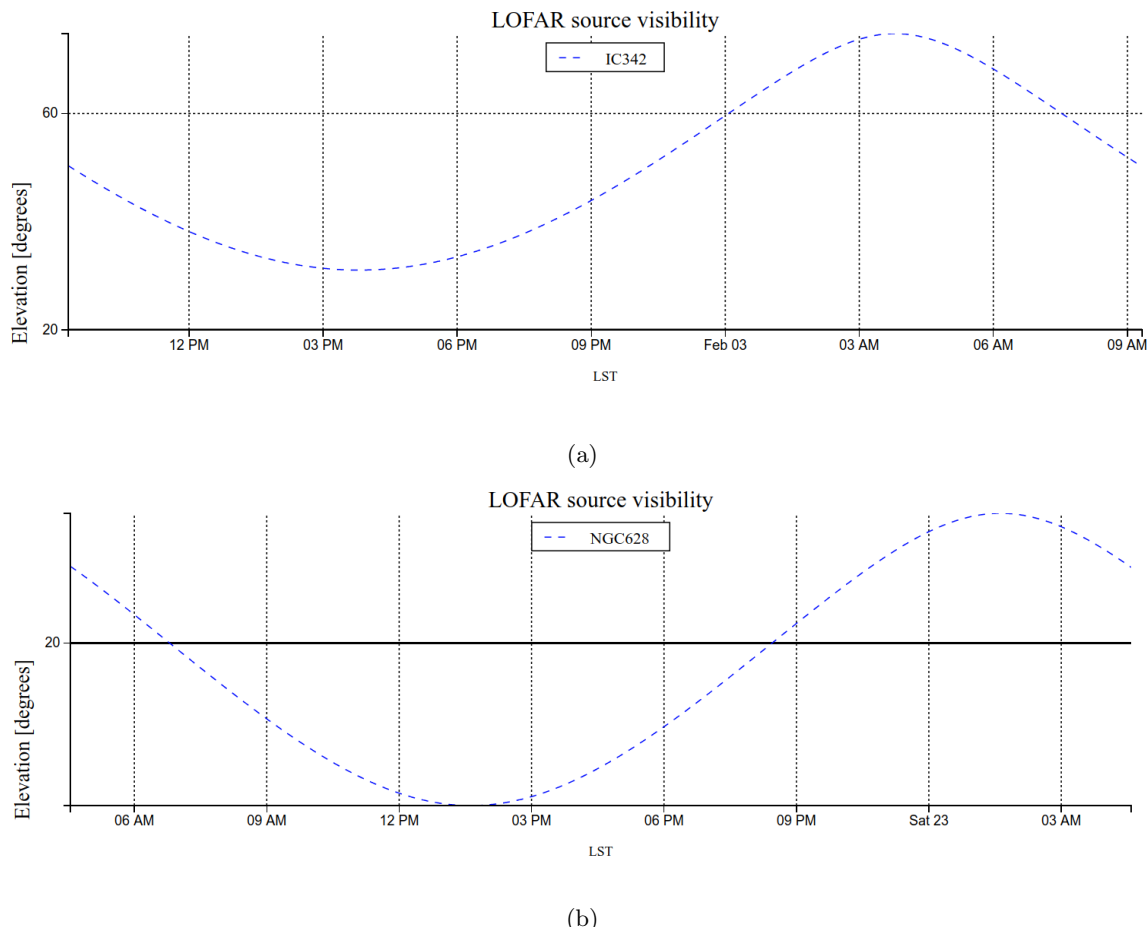


Figure 2.16: The Figure shows the elevation of the two target sources- IC 342 and NGC 628 at the time of observation. The elevation of NGC 628 is lower, which resulted in a lower sensitivity i.e., higher noise level in its image. The plots have been obtained using <https://support.astron.nl/otool>.

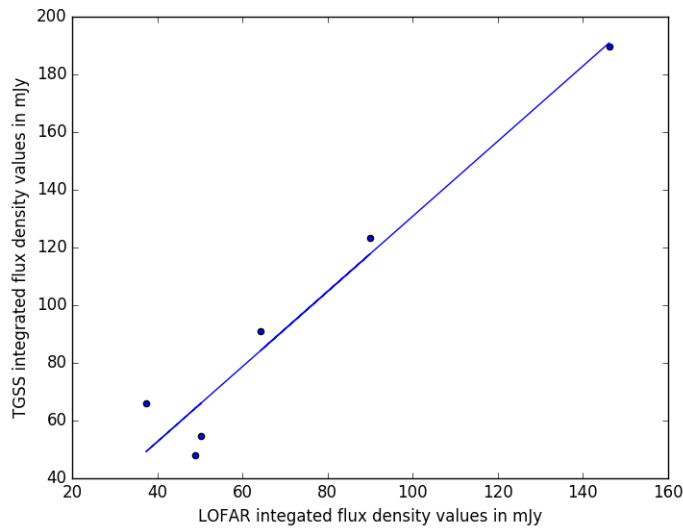


Figure 2.17: The values of integrated flux density values of point sources from the TGSS catalog and the integrated flux density values obtained from LOFAR were compared. On an average, the TGSS point sources had a flux density a factor of 1.3 higher than the LOFAR point sources. Hence, the maps have been multiplied by a factor of 1.3.

2.5.1 Checking flux density scales using TGSS

The integrated flux densities of some of the point sources in the LOFAR map are compared with the values from TGSS ADR1 (Intema et al. 2017). The Figure 2.17 shows the flux densities of various sources in the TGSS catalogue versus the sources in my image. I find that the sources from TGSS have an integrated flux density of 1.3 times higher than my sources. Hence, the images have been multiplied by a factor of 1.3 to take care of the difference in the flux density scale, as it seems substantial.

Chapter 3

Scientific analysis

In the course of this chapter, the results from the images obtained from the LOFAR data are explained.

3.1 Spectral index mapping

Overview of method used: Spectral index mapping involves several steps. One may use the task `COMB` in `AIPS`¹ or the task `immath` in `CASA`². However, it is not possible to obtain a satisfactory error distribution map using these methods. Hence, I obtained the spectral index map and the error map using the method described in this section.

The maps being used to obtain spectral index are of different frequencies, and hence have different inherent beam sizes. Hence, the map with higher spatial resolution is re-sampled to the resolution (lower) of the other map. This is generally done using the `convolution` operation. The Full Width at Half Maximum (FWHM) for both the synthesized beams values are converted to standard deviation using the formula valid for Gaussian distributions (Equation 3.1).

$$\sigma = \frac{\text{FWHM}}{2\sqrt{2\ln 2}}. \quad (3.1)$$

The synthesized beams for the images that have been used in my case are circular. Equation 3.2 shows the convolution formula used. $\sigma_{\text{New kernel}}$ is the standard deviation for the new Gaussian kernel that is to be used for convolving the higher resolution image. $\sigma_{\text{Higher frequency}}$ is the standard deviation of the synthesized beam of higher frequency image. $\sigma_{\text{LOFAR frequency}}$ is the standard deviation of synthesized beam for the LOFAR image.

$$\sigma_{\text{New kernel}} = \sqrt{\left(\sigma_{\text{LOFAR frequency}}^2 - \sigma_{\text{Higher frequency}}^2\right)} \quad (3.2)$$

The beam size is converted to pixel units by multiplying it with the pixel scale in the image. Once the size of the convolution kernel is known in pixel units, we Gaussian smooth (`convolve`) the higher resolution image to have the resolution of the lower resolution image. The images are usually of different sizes, and hence, to ensure that both the images are of the same size, bi-linear interpolation method using the ‘`resize`’ function in sci-kit library of python can be used. Spectral index is calculated using the assumption that the intensity, $I \sim \nu^{-\alpha}$. The error maps are estimated using standard Gaussian error propagation.

3.1.1 IC 342

For IC 342, the spectral index map is made using the images at 1.49 GHz frequency (Beck 2015) and the LOFAR map (at 145 MHz), as shown in Figure 3.1. The UV data from the VLA map uses the baselines from 200 λ to 5200 λ . Though the LOFAR visibilities also have several short baselines due to the dense core, the shorter baselines need to be clipped so that both the maps are sensitive to the same angular scales. The images thus obtained are gridded to have the same grid using the AIPS task `OHGEO`. The LOFAR map is calibrated using the flux density scale as described in Scaife & Heald (2012), while the VLA map was calibrated using the flux density scale as

¹<http://www.aips.nrao.edu/cgi-bin/ZXHLP2.PL?COMB>

²<https://casa.nrao.edu/docs/taskref/immath-task.html>

described in Perley & Butler (2017). The spectral index map is then computed pixel by pixel. The maps presented in this paper are made using a five-sigma filter on the noise levels for both the input images. Both the maps from the two frequencies have a resolution of 45 arcsec. The images of this resolution have been used because the higher resolution images from the LOFAR map still contain several artifacts, while the 45 arcsec image can be seen to have better depiction of diffuse emission.

We plot the histogram showing the distribution of spectral indices values from the Figure 3.1 in the Figure 3.2, and find that the median value is -0.52 for IC 342. The binning has been done using the Freedman-Diaconis rule³

3.1.2 NGC 628

For NGC 628, the spectral index maps depicted in Figure 3.3, have been made using the maps from frequency 3 GHz using VLA data and 141 MHz LOFAR map. Due to the absence of UV calibrated data, we convolve both LOFAR and VLA maps to have the same resolution of 20 arcsec. The images are then regridded using OHGEO task in AIPS and the spectral index map is made with 3-sigma flux densities (3 times the noise level in the individual maps) for both the images. The 20 arcsec image was chose for the LOFAR map because it has a higher Signal to Noise ratio than the other images, while curbing the artifacts. The VLA image used had a resolution of 18 arcsec, and is convolved to have a resolution of 20 arcsec.

In the Figure 3.4, one can take a look at the histogram showing the distribution of spectral index values from the Figure 3.3. The median value for the spectral index values is -0.86, which is the steepness expected from synchrotron emission.

3.2 Interpretation of spectral index maps

One can learn about the process involved in the galaxy with the help of spectral index maps. The Figure 3.5 shows various process involved in a galaxy at low radio frequencies that influence the spectrum can be seen. The spectral index for synchrotron emission is -0.7 and that of thermal emission is -0.1. Thermal absorption is a process that is important especially in star forming galaxies, and explains the flat spectrum when very low frequencies are considered. If one considers the spectral index values between frequencies ν_2 and ν_3 , a flat spectral index is seen. This flatness is because of the thermal emission at the ν_3 frequency. If one considered the spectral index between frequencies ν_1 and ν_2 , the flat spectral index is explained by thermal absorption.

3.2.1 IC 342

The Figure 3.1 shows the spectral index map obtained for IC 342. The edges and the inter-arm regions of IC 342 can be seen to have a steep spectral index. This means that the flux density for the galaxy in the VLA map is much lower than that of the LOFAR map. This implies the presence of a higher level of the synchrotron emission that is traced at lower frequencies. A steep spectral index indicates the presence of low energy, older electrons that have traveled farther away from the spiral arms and the central region where the star formation occurs. Hence, the steep spectral index is expected at these regions.

Flatter spectral index (0.2 to -0.2) can be seen in the center of the galaxy. Flat spectral indices imply that the flux density values for VLA and the LOFAR maps have only a small difference. With the help of the Spectral Energy Distribution (SED), it can be argued that the flat spectral index can happen because of either an increase in the flux density of the galaxy in the VLA map because of thermal emission, or from a decrease in the flux density of the galaxy in LOFAR map because of thermal absorption.

Thermal emission: To examine which process results in the flat spectral index in my case, we first try to obtain the thermal fractions required to explain such a flat spectral index. The thermal and non-thermal components are separated by assuming a constant spectral index (α_{nth}) of -0.7 and -0.5 for synchrotron emission, and a thermal spectral index (α_{th}) of -0.1 for thermal emission. The resulting thermal fractions (f_{th}) are listed in Table 3.1.

³According to this rule, the bin size, $B = 2 \times \frac{IQR(x)}{\sqrt[3]{n}}$, where $IQR(x)$ is the interquartile range, and n is the number of observations in the sample x .

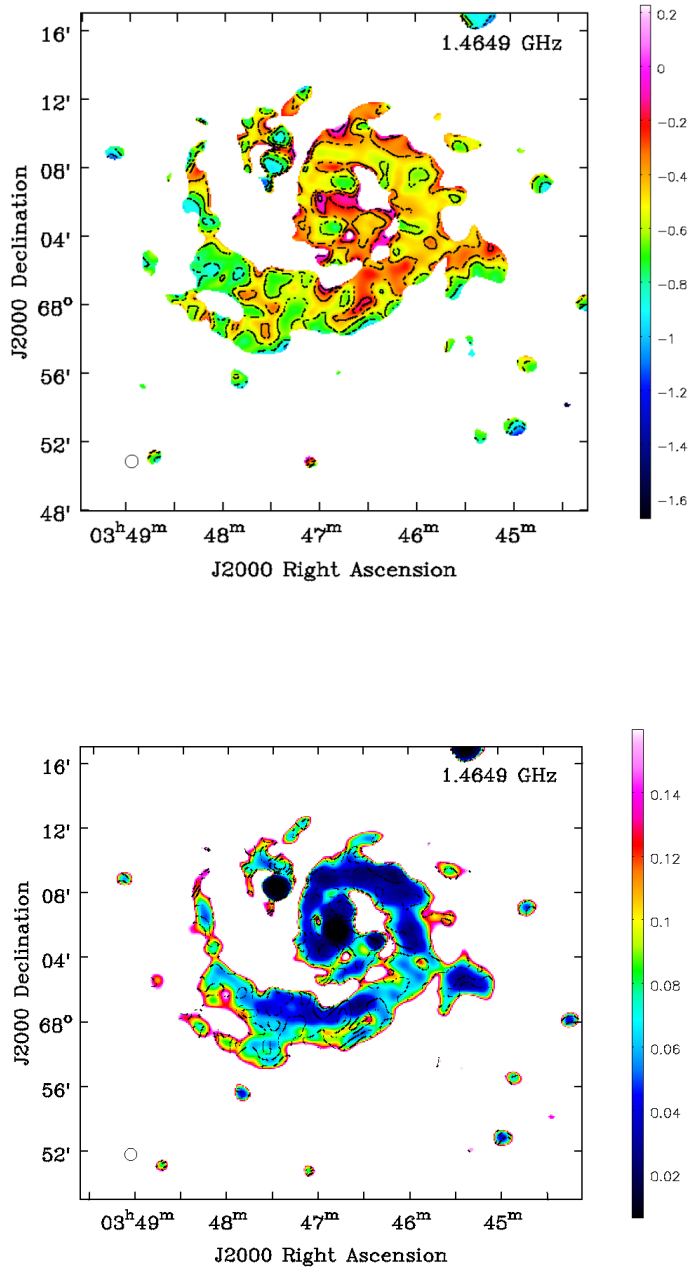


Figure 3.1: *Above:* The spectral index map of IC 342 obtained from 1.4 GHz VLA map and 145 MHz LOFAR map at $45''$ resolution. It uses values above $5 \times$ the noise level (5σ) from the VLA and LOFAR maps. The contours on the map are 0.2, 0.4, 0.6, 0.8, 1, 0 \times -1. *Below:* The error map for the spectral index map. The contours are the same for both the images.

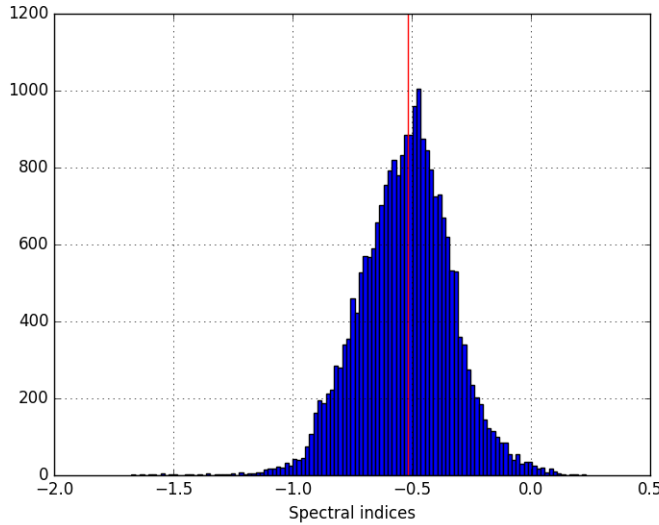


Figure 3.2: The spectral index distribution for IC 342 for the spectral index map shown in Figure 3.1. The binning is done according to Freedman-Diaconis Rule (Freedman & Diaconis 1981)

α_{obs}	$f_{\text{th}-0.7}$ (145 MHz)	$f_{\text{th}-0.7}$ (1490 MHz)	$f_{\text{th}-0.5}$ (145 MHz)	$f_{\text{th}-0.5}$ (1490 MHz)
-0.7	0%	0%	-	-
-0.6	9%	28%	-	-
-0.5	19%	49%	0%	0%
-0.4	33%	67%	17%	34%
-0.3	51%	81%	39%	61%
-0.2	72%	91%	66%	83%
-0.15	85%	96%	82%	92%
-0.1	100%	100%	100%	100%

Table 3.1: If a spectral index for synchrotron emission is assumed as -0.7 and thermal emission is assumed as -0.1 , the percentage of thermal fraction for the observed spectral index values (between frequencies of 145 to 1490 MHz, α_{obs}) are obtained (represented as $f_{\text{th}-0.7}$), at the two frequencies — 145 MHz and 1.49 GHz. The same is done when the spectral index for synchrotron emission is assumed to be -0.5 and the thermal fraction is represented as $f_{\text{th}-0.5}$. These values have been obtained using the code from Dr. Beck (priv. comm).

These fractions seem too high for a galaxy. Beck (2015) found that the thermal fraction at $\lambda 6.2$ cm is about 50% in the central region and 20% to 30% in the spiral arms and 10% or less in the inter-arm region⁴ at 1.49 GHz.

Tabatabaei et al. (2017) found that the thermal fractions in galaxies is around 10%. If one uses this value to be the thermal fraction in IC 342, then for the observed spectral index values of -0.4 , -0.3 , -0.2 and -0.15 , one must assume that the synchrotron spectral index value is -0.63 , -0.53 , -0.42 , -0.32 , -0.21 and -0.16 respectively. This shows that for these spectral indices, thermal emission does not satisfactorily explain the observed flat spectral indices, as it is not physically valid according to existing models of cosmic ray electron acceleration.

Thermal absorption: In order to see if the flat spectral index values are because of free-free absorption, the thermal map obtained from 1.49 GHz is overlaid on the spectral index map. The thermal map traces the regions of star formation activity. Hence, the regions in which the thermal flux density is higher, there is a higher Star Formation Rate (SFR). These SF regions would result in **free-free absorption**, resulting in a decrease in the flux density of the galaxy at the lower frequency.

From the Figure 3.6, we can see that the higher thermal flux density region coincides with the regions of flatter spectral index. Furthermore, from Balser et al. (2017), we know that several dense (with electron densities of

⁴Although it was argued that the thermal fraction is overestimated in the spiral arms because of their method used.

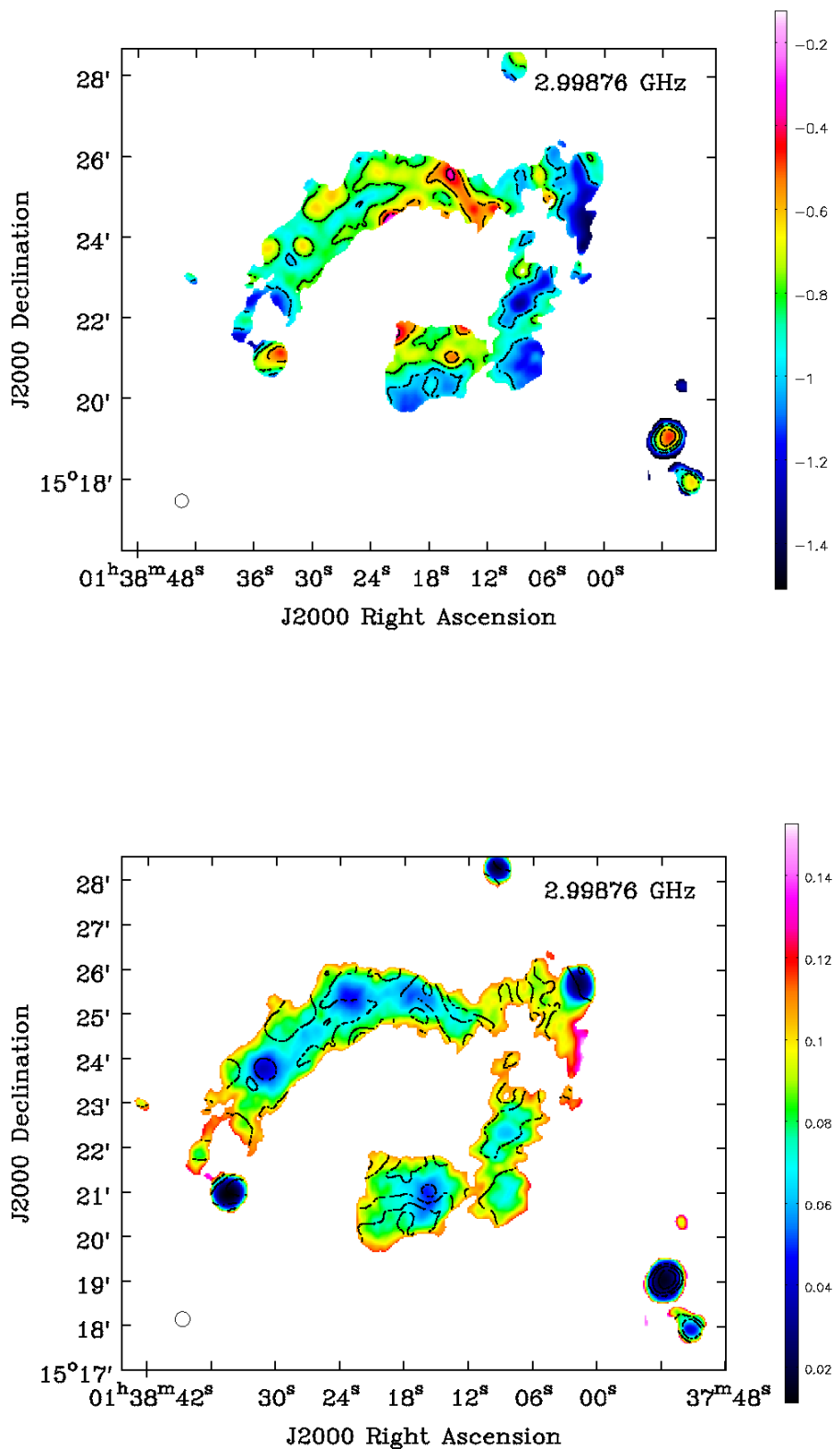


Figure 3.3: *Above:* The spectral index map for NGC 628 obtained from 3 GHz VLA map and 145 MHz LOFAR map at 20'' resolution. This is a 3-sigma spectral index map. The contours on the map are 0.2, 0.4, 0.6, 0.8, 1, 0 with unit contour level of -1. *Below:* The error map for the spectral index map. The contours are the same for both the images.

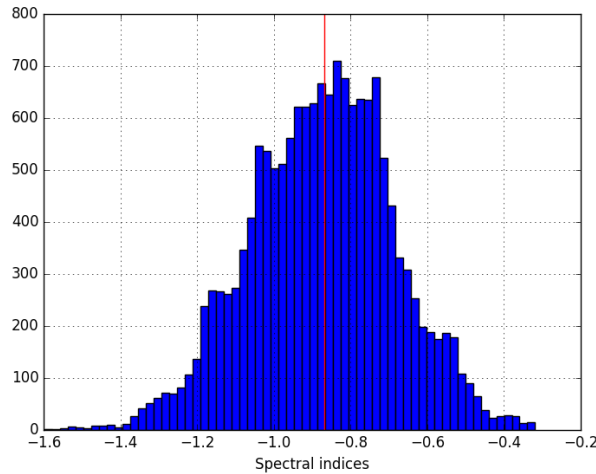


Figure 3.4: This histogram shows the distribution of the spectral index values for NGC 628. The median lies at -0.86 (expected value).

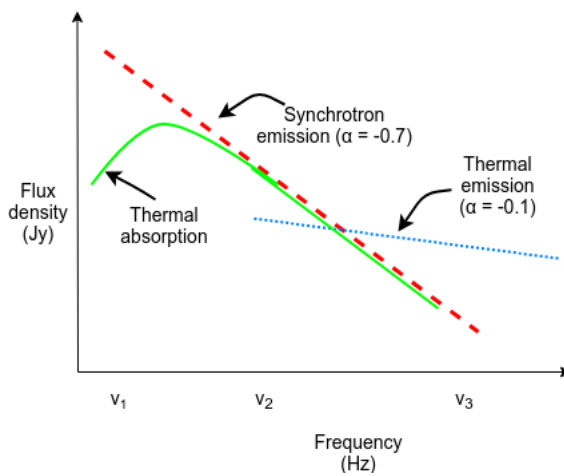


Figure 3.5: Spectral Energy Distribution (SED) for the three processes important in star-forming galaxies like IC 342. The red dashed line indicates synchrotron emission, and has a spectral index value (α) of -0.7. The thermal emission is indicated by the blue dotted line, and has a spectral index value of -0.1. Thermal absorption process is indicated by the green curve. This process is responsible for the flattening of the spectral index at low radio frequencies. Based on the two frequencies considered to obtain the spectral index, the flattening and steepening of the spectrum can be explained.

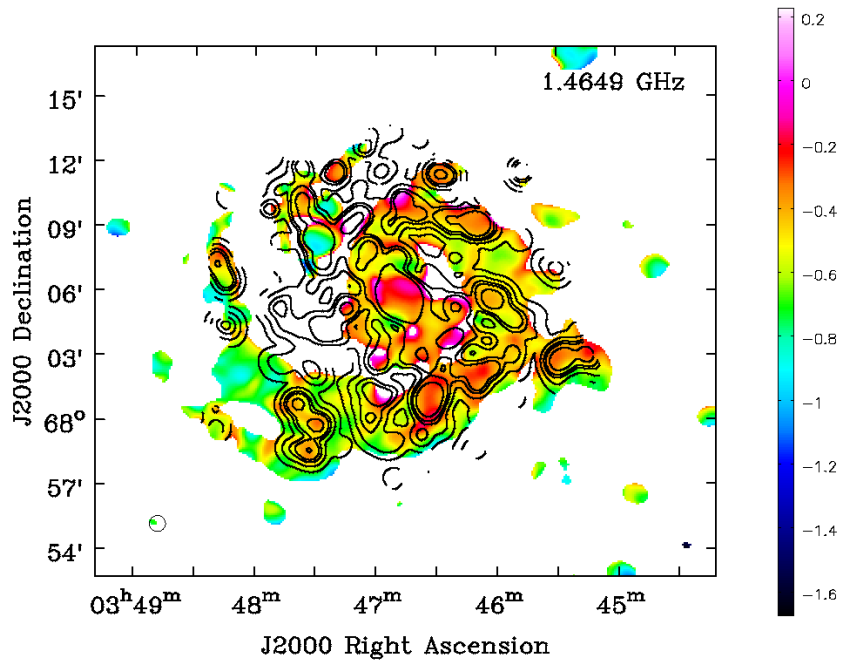


Figure 3.6: This image depicts the correlation of the flatter spectral index and the presence of thermal emission. The contours are 0.5, 5, 18, 32, 80 of the thermal map with unit contour level of 10 mJy/beam

around $104\text{-}105 \text{ cm}^{-3}$), and compact ($\leq 0.1 \text{ pc}$) H II regions are predicted to exist in the nucleus of the galaxy. These regions are known to be heated by the ionizing photons from the early-type stars. They are cooled by lines excited from collisions such as C II line of wavelength $158 \mu\text{m}$. Free-free absorption is especially pronounced in H II regions as explained in Chapter 1. So, we can conclude that the LOFAR synchrotron flux density in the nuclear region is decreased due to the presence of such H II regions, that give rise to free-free absorption. In the Figure 2.1, we can take a look at the position of the H II regions existing in the nucleus of the galaxy.

In order to understand the correlation better, we plot the correlation between the flux densities of the thermal map with the spectral index values for each pixel. From the Figure 3.7, we can see that the pixels with a higher flux density of the thermal map, have a much flatter spectral index value. Thus, we can conclude that the free-free absorption regions with high star formation give rise to flat spectral index.

I also plot a Far Infra Red (FIR) map of 350 nm over the galaxy, that is from the KINGFISH project (Key Insights on Nearby Galaxies: a Far-Infrared Survey with Herschel) (Kennicutt et al. 2011). FIR emission comes from re-radiation by dust, which has been heated by ultra violet (UV) photons. These photons are emitted by massive and short-lived stars. The diffusion length of a CRE is much larger than the mean free path of an FIR photon, a radio continuum image would appear as a smoothed version of a FIR image. The Figure 3.8 shows the correlation of the star forming regions with that of flat spectral index, indicated by the redder regions.

3.2.2 Case of missing flux

We plot the integrated flux density within successive radii of width 0.5 arcmin and obtain the plots shown in Figure 3.10. This is done for both the 20 cm map and the LOFAR map, with full UV coverage for both the maps. We find that the total flux density integrated to $10'$, $S_{\text{LOF}} = 4.82 \pm 0.22 \text{ Jy}$ for the LOFAR map. For the 20 cm map, this value is $S_{\text{VLA}} = 2.26 \pm 0.13 \text{ Jy}$. This shows that there is a lot of missing flux in the LOFAR map, if we consider the existence of only synchrotron emission.

In order to figure out the amount of missing flux, we first extrapolate the flux density values obtained for IC 342 using the values found by Tabatabaei et al. (2017) at higher frequencies, and obtain the spectral index as -0.76 . As can be seen from figure 3.9, the α value is extrapolated to 145 MHz , we expected flux density value is obtained,

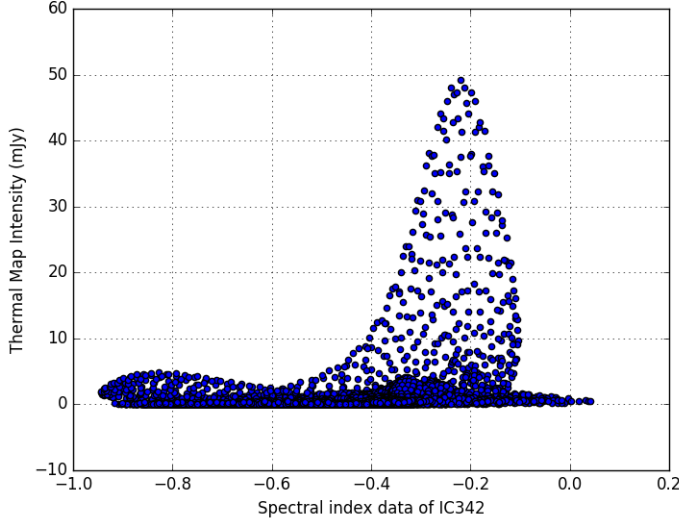


Figure 3.7: Correlation of the thermal intensity values with the spectral index map values for IC 342. The spectral index values are obtained by clipping the values of flux densities lower than $5 \times$ the noise level in 1.49 GHz and 145 MHz map, for each pixel. From the Figure, it is evident that regions with higher radio thermal flux density which indicate the presence of free-free absorption from star forming regions, have a flatter spectral index values. The 'tail' seen at the right hand portion showing the discrepancy may be because of the missing diffuse flux density that affects spectral indices at low intensity.

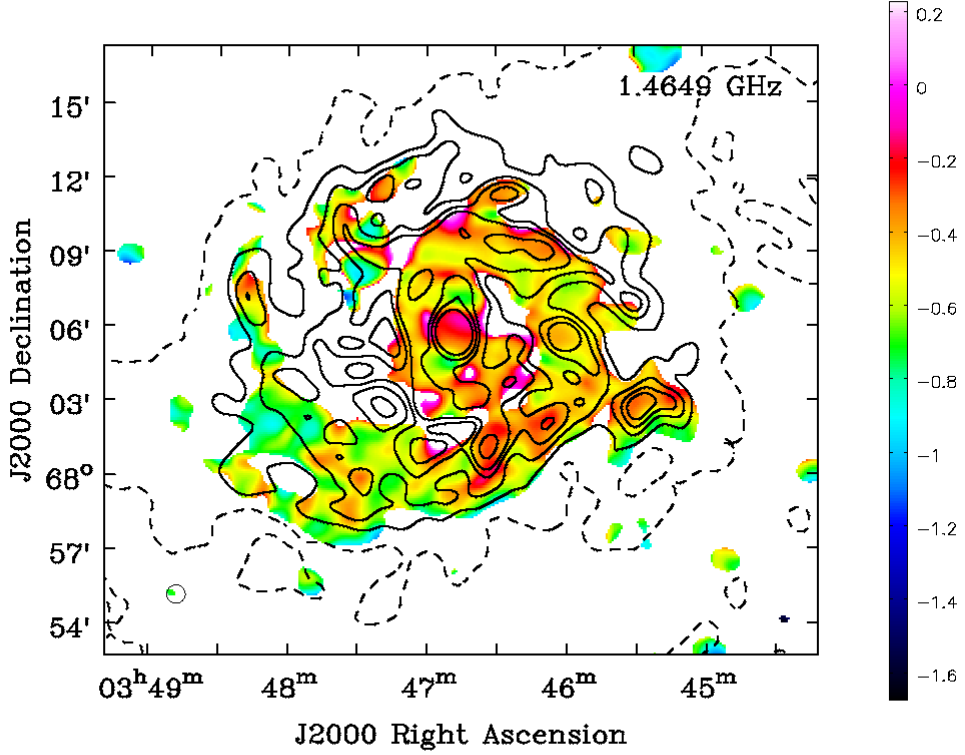


Figure 3.8: The overlaid plot is the FIR map of IC 342 at $350\mu\text{m}$. One can notice the correlation of flatter spectral index and higher flux density of this map. The contours represent $0.2, 0.4, 0.6, 0.8, 1, 1.5, 2, 3 \times 15 \text{ Jy/beam}$.

$S_{\text{EXP}} = 10.7 \text{ Jy}$.

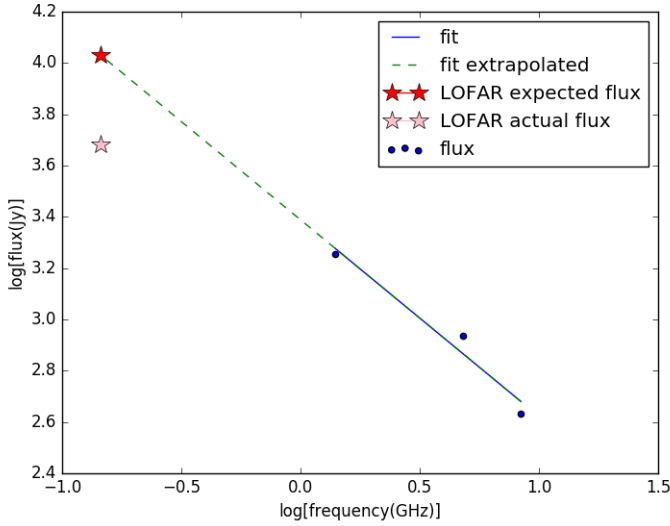


Figure 3.9: This plot shows the flux density values from previous study done for the galaxy by Tabatabaei et al. (2017) for IC 342 as blue dots, with the fit shown in blue line. The green dashed line represents the extrapolated fit with the slope of -0.76. The pink star represents the flux density from the LOFAR map, and the red star represents the expected flux density for the frequency of 145 mHz.

Thus, the amount of missing flux density, $\Delta S = S_{\text{EXP}} - S_{\text{LOF}} \approx 5.9 \text{ Jy}$. The missing flux density per unit beam is given by:

$$\frac{\Delta S}{N} = \Delta S \left(\frac{\text{Area of integration (in arcmin)} \times \cos i}{1.13 \times \text{Resolution of image (in arcmin)}} \right) \approx 14 \text{ mJy/beam}, \quad (3.3)$$

where i is the angle of inclination. This value is almost 36 times the rms noise in the image. This means that a lot of the diffuse flux density is missing.

One explanation for the flux density to be low is thermal absorption. The inner part of IC 342 has a high amount of thermal absorption as is seen from the flat spectral index at the center. Hence, we obtain the amount of missing flux density due to thermal absorption by obtaining the flux density value within 3' radius of the galaxy (with the galaxy's center as its center). This is done between maps that have the same UV baseline coverage with the rest of the baselines clipped, as the diffuse flux in both the maps would be missing, leading to a fair comparison between the two maps.

The amount of thermal absorption is obtained by extrapolating the flux density of the VLA map within 3' to obtain the expected flux density at the frequency of LOFAR, using the relation $S \propto \nu^\alpha$, with alpha being the spectral index (-0.5⁵). $S_{3'}$ is the flux density observed in the LOFAR map within the radius of 3'.

$$\frac{S_1}{S_2} = \left(\frac{\nu_1}{\nu_2} \right)^\alpha \quad (3.4)$$

$$S_1 = S_2 \left(\frac{\nu_1}{\nu_2} \right)^{-0.5} \quad (3.5)$$

$$S_1 = 273 \text{ mJy} \left(\frac{145}{1490} \right)^{-0.5} \approx 870 \text{ mJy} \quad (3.6)$$

$$S_{3'} = 555 \text{ mJy} \quad (3.7)$$

$$\Rightarrow \text{Flux lost due to thermal absorption} \approx 300 \text{ mJy} \quad (3.8)$$

⁵This spectral index is taken as a combined α value for thermal emission and synchrotron emission.

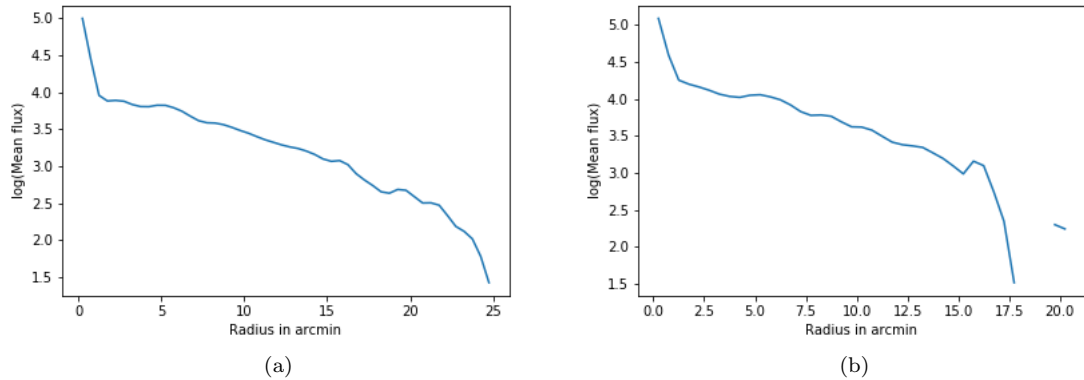


Figure 3.10: The radial profiles for the full UV range maps. *Left:* The radial profile of the galaxy IC 342 i.e., radius vs log of integrated flux density for 20 cm map. *Right:* The radial profile for the LOFAR map. The bright background source for both the images has been subtracted before the integration has been performed.

With the help of this correction flux density value, we can figure out the amount of flux density missing in the overall galaxy (i.e., for the galaxy upto a radius of $10'$).

Correction ≈ 300 mJy (3.9)

$$S_{\text{EXP}} = 688 \left(\frac{1.49}{0.145} \right)^{0.74} \approx 3.72 \text{ Jy} \quad (3.10)$$

$$S_{\text{LOF}} = \underbrace{1.4}_{\mathbf{A}} + \underbrace{0.3}_{\mathbf{B}} \text{ Jy} \approx 1.7 \text{ Jy} \quad (3.11)$$

$$\Rightarrow \Delta S = 3.72 - 1.7 \approx 2.02 \text{ Jy} \quad (3.12)$$

$$\text{Missing flux/beam} = \frac{\Delta S}{N} \approx 4.47 \text{ mJy} \quad (3.13)$$

where \mathbf{A} and \mathbf{B} in Equation 3.11 represents the flux from my LOFAR map of the galaxy upto a radius of 10' and the thermal absorption flux density of the galaxy obtained respectively. If one considers the value of -0.5 as the value of the overall spectral index of the galaxy upto a radius of 10', then this value is reduced is **1.1 mJy**. This value of only 1.6 times the noise level.

Scale height: The integrated flux density values for IC 342 for successive radii in rings with a width of 0.5' (about 0.5 kpc) are obtained, with the center of the rings aligned at the center of the galaxy. The plot with the radial profile using the obtained values is shown in Figure 3.10. This is done for the images of the two frequencies- 145 MHz and 1.49 GHz, with the maps made using the full UV range. We also obtain the scale lengths⁶ for the two maps. For the LOFAR map, it is 15 arcmin, which is around 14.8 kpc. The scale height for the 20 cm map, it is 19 arcmin, which is around 18.7 kpc. Scale length shows the distance traveled by the CRE that is giving out that frequency photon. Here, an electron emitting the photon in LOFAR frequency (145 MHz) travels a distance of 14.8 kpc. Due to the longer life-time of the cosmic ray electrons that are detected using the LOFAR map, we should be able to see a longer scale length in the case of LOFAR map. However, this is not the case, which shows that the LOFAR map has less diffuse flux from the extended emission than is expected.

Comparision with spectral index maps at other frequencies: The Figure 3.11 shows the spectral index values obtained between λ 6.2 cm and λ 20.1 cm at 25" resolution (Beck 2015). As the wavelengths of the two maps

⁶The scale length is defined as the radius at which the flux density of the galaxy has fallen off by a factor of e (2.71828) from the center. The flux density can be written as the function:

$$I = I_0 \exp\left(-\frac{r}{r_0}\right)$$

Here, I_0 is the flux density in the center of the galaxy and r_0 is the scale length. Hence, when plotting $\ln I$ as a function of the radius r , the scale length is given by $r_0 = -\frac{1}{S}$, where S is the slope of the fitted linear line

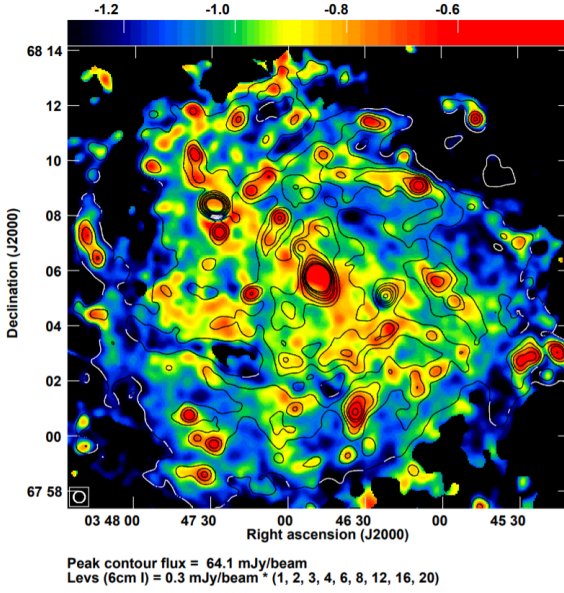


Figure 3.11: This is the spectral index map obtained between $\lambda 6.2$ cm and $\lambda 20.1$ cm at $25''$ resolution. Contours show the total intensity at $\lambda 6.2$ cm. It has been taken from Beck (2015).

in Figure 3.11 are lower, the flatness in the spectral index can be explained by thermal emission (the flux density in this case is higher for the lower wavelength— $\lambda 6.2$ cm map, resulting in a flat spectrum). The spectral index in the inter-arm regions and in the outer disk is steep, as expected, due to synchrotron emission.

3.2.3 NGC 628

The spectral index map of NGC 628 can be seen in the Figure 3.3. The regions with flatter spectral index values are depicted in red. One can trace the presence of spiral arms in the red regions, and the outer edges of the galaxy have a steeper spectrum, as shown by the green regions. This shows that the spiral arms have flatter spectral index which are the regions with younger recently formed stars. The steepness in the outer regions is indicative of the older electron population, where the flux density of the LOFAR map is much higher than that of the VLA map.

In order to study the star forming regions in NGC 628, and understand the flattening of the various regions, we overlay an H alpha image onto the spectral index map⁷. We can see a clear correlation between the flattening of the spectrum and the H alpha region. We can also see the two arms of the galaxy that are traced by both the H alpha region and the flatter (depicted by red) in the galaxy. The steeper part of the galaxy that contains the synchrotron emission from the diffuse electrons can be seen between the two arms. This shows that most of the star formation takes place in the arms while the diffuse older electrons that have traveled away from the spiral arms are present in the inter-arm regions. This part of the galaxy is marked as region **A**, **B** and region **E** in the Figure 3.12.

However, something peculiar is seen in the region marked as **D**. It appears to be much steeper even though there is a clear increase of the intensity in the H alpha map. In order to understand it better, I overlay the LOFAR map with an optical image as can be seen in the Figure 3.13. In this image, this region is shown in yellow meaning that it is not an H II region. However, in the paper Kennicutt & Hodge (1980), this source has been listed as an H II region, of the name “NGC 0628:[H76] 566”, although not much is known about this region. Hence, this discrepancy may be because the red continuum has not been sufficiently subtracted in the H alpha map, which may be because of the presence of a bright star in H alpha image.

The Figure 3.14 shows the various regions and their correlations. The two spiral arms have different slopes in the correlation plot. This may be because of different levels of star formation in the two arms, which gives rise to different levels of thermal absorption in the galaxy at various regions. It is interesting to note that the Figure 3.7, depicting the same correlations does not show this feature of differing slopes.

⁷H-alpha emission has a wavelength of 656.28 nm in the visible spectral range. It occurs when a hydrogen electron falls from its third to second lowest energy level.

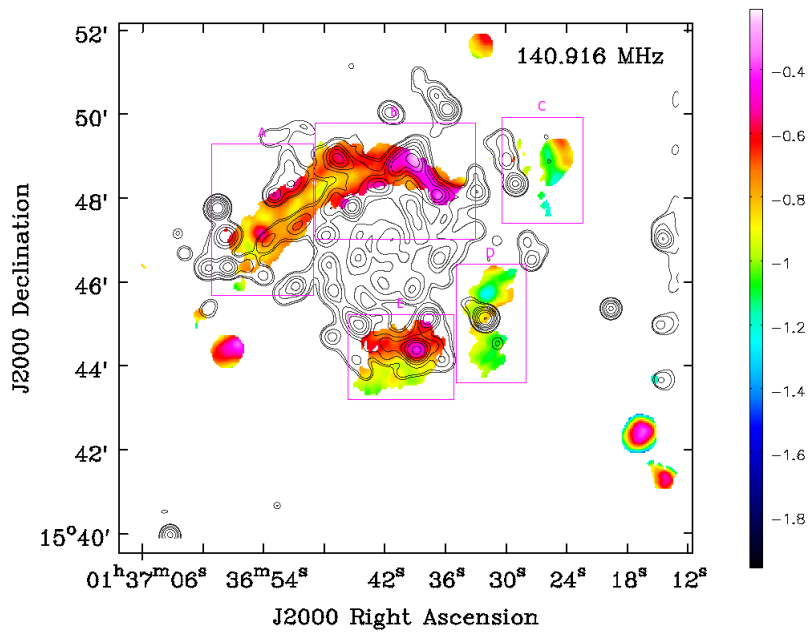


Figure 3.12: This image depicts the correlation of the flatter spectral index and the presence of H- α emission. The contours are 0.5, 1, 3, 5, 8, 12, 18, 32, 44, 80 of the h-alpha map with unit contour level of 5 mJy/beam. The regions are described in the text.

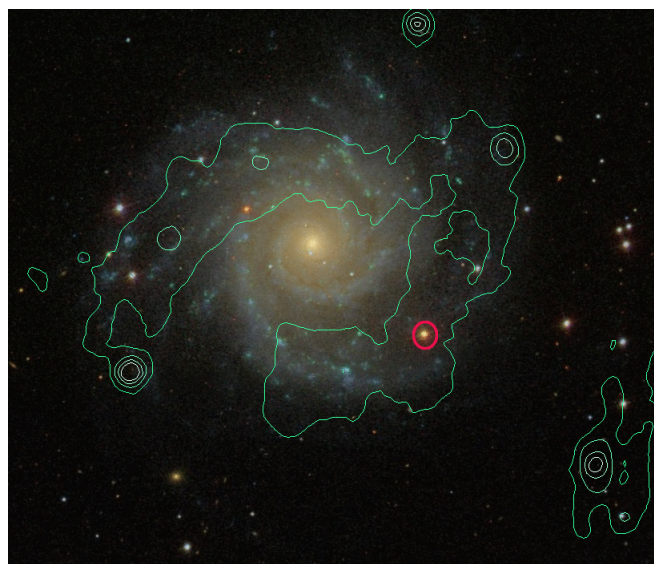


Figure 3.13: Overlaying the LOFAR map onto an optical image from SDSS shows that this region contains a stellar object. This was done in order to understand the region marked **D**.

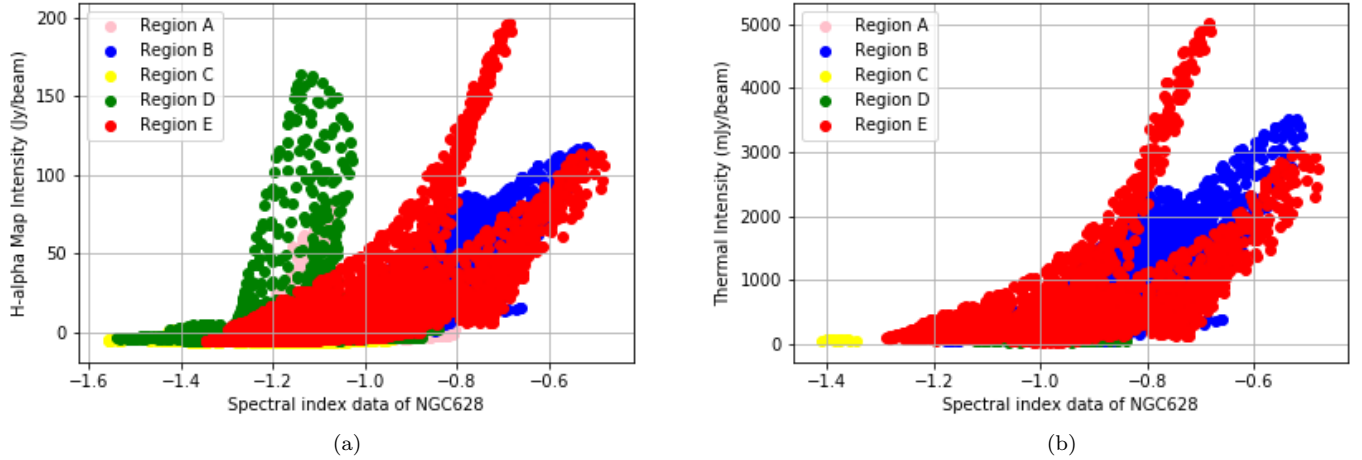


Figure 3.14: Correlation plots of the thermal intensity values value with the spectral index map values, for each pixel. The various regions have different slopes of correlation, which is interesting. *Left:* The correlation plot of the H-alpha map flux density. the region marked **D** in this case seems to have a higher flux in H-alpha map, but with a steep spectral index. *Right:* The correlation plot of the thermal radio map. The region **D** in this plot vanishes. Hence, the discrepancy seen in region **D** was because of an improper continuum subtraction.

In order to understand the discrepancy in the region **D**, we try to do the correlation plot using the thermal radio map obtained at a frequency of 3 GHz ([Mulcahy et al. 2017](#)). In this case, the region **D** does not have a higher intensity value in the thermal map, and hence, the steep spectral index is correct. This map can be seen in the Figure 3.15.

Integrated flux density: The integrated flux density values for NGC 628 for successive radii in rings with a width of 0.5' (about 1.1 kpc) are obtained, with the center of the rings aligned at the center of the galaxy. The plot with the radial profile using the obtained values is shown in Figure 3.16. This is done for the images of the two frequencies- 145 MHz and 3 GHz. I then find the integrated flux density of the galaxy up to a radius of 5' of NGC 628 (around 11 kpc) in the VLA map at a frequency of 3 GHz to be 108 ± 3 mJy. The value for the LOFAR map for this integrated flux at 145 MHz is 680 ± 120 mJy. This value seems to show that the spectral index of the map is -0.61. This shows that overall, synchrotron emission dominates in the LOFAR frequency for the galaxy.

3.3 Star Formation in the two galaxies

In this section, I shall discuss star formation in the two galaxies- IC 342 and NGC 628. Star formation in spiral galaxies is usually seen to take place in the spiral arms. It would be interesting to understand whether spiral arms trigger star formation, or if they rearrange the stars and molecular gas such that majority of star formation (SF) is seen in the arms. One may hypothesize that the sudden increase in the density in the spiral arms results in mechanisms of gravitational collapse such that conditions for SF is acquired. Stars are formed from molecular gas. However, most of the molecular H₂ is cold (10-20 K) and hence, invisible. It is also not easily excitable as requires a large amount of energy to be excited⁸. Hence, CO, the next most abundant molecule is used as its tracer. Using the well known Kennicutt-Schmidt (K-S) law, one can obtain the SF Rate (SFR) of a galaxy ([Schmidt 1959](#)):

$$\Sigma_{SFR}(\text{M}_\odot \text{ yr}^{-1} \text{kpc}^{-2}) \propto (\Sigma_{\text{gas}})^N (\text{M}_\odot \text{kpc}^2) \quad (3.14)$$

Here, Σ_{SFR} represents the SFR surface density and Σ_{gas} represents the gas surface density. Usually, the gas surface density is replaced by the H₂ as most of the molecular gas is in this form. Then with the help of the CO surface density, using a conversion factor, one can obtain the Σ_{H_2} .

In the paper [Pan et al. \(2014\)](#), it is found that IC 342 is an H₂ dominated spiral galaxy where significant amount of SF could occur. The SF mechanisms discussed in the paper include gravitational instability in the disk and at

⁸First level rotational level, which is accessible only from a quadrupolar transaction, occurs at a temperature above 500 K.

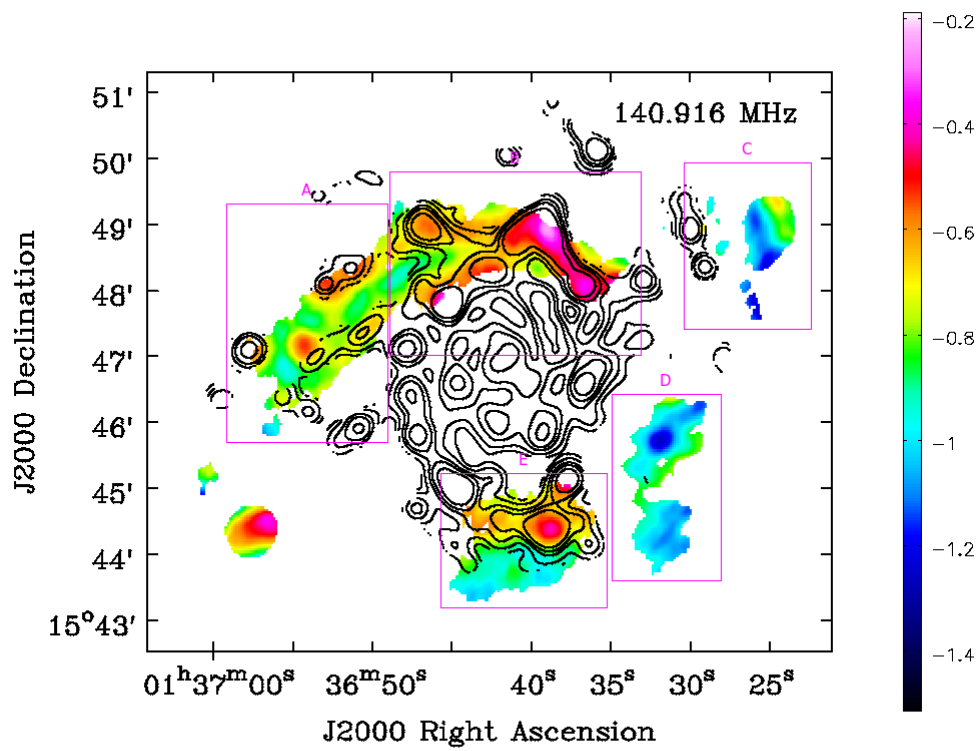


Figure 3.15: Correlation of the flatter spectral index in NGC 628 and the presence of thermal radio emission at 3 GHz frequency. The contours are 0.1, 0.2, 0.4, 0.6, 1×0.1 mJy/beam.

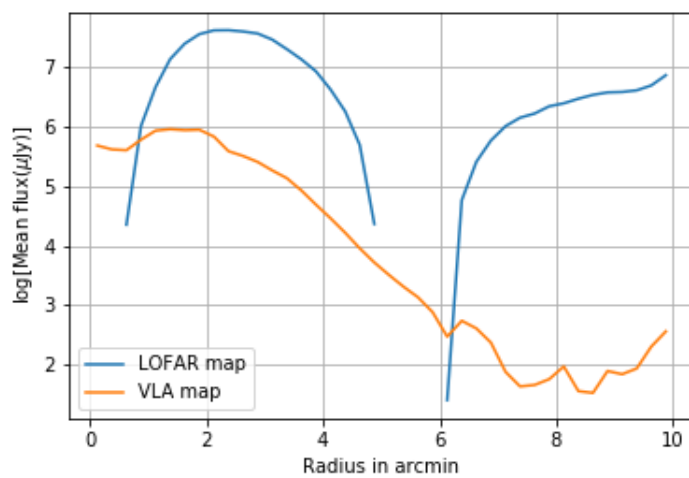


Figure 3.16: The radial profile of the galaxy NGC 628 i.e., radius vs log of integrated flux density for 3 GHz map ([Mulcahy et al. 2017](#)) and 145 MHz LOFAR map.

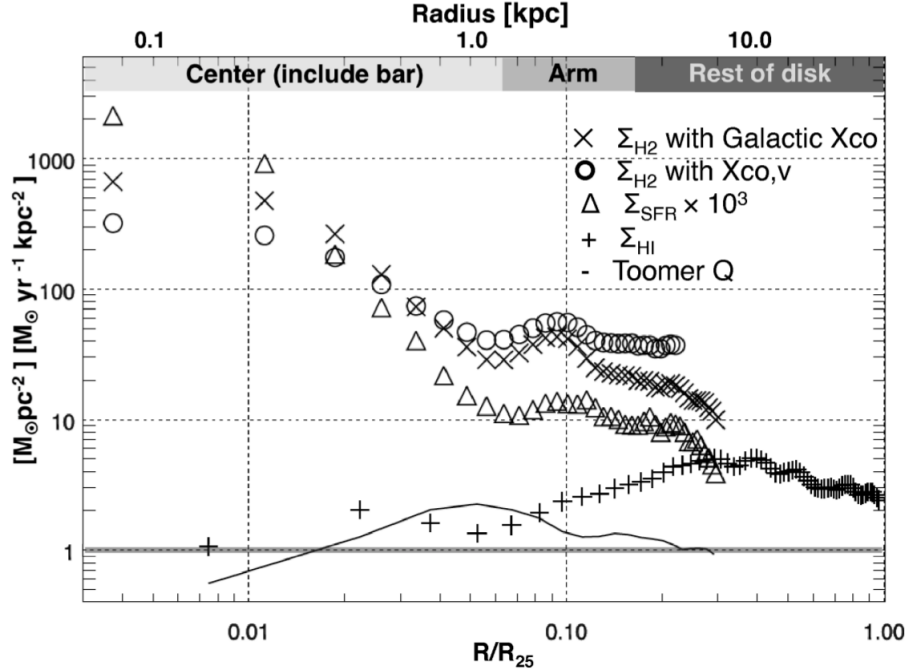


Figure 3.17: The SFR are shown as small triangles (Pan et al. 2014). Each radial step here is $10''$. One can see a similarity in the two plots. In the center, high star formation exists, and that region has a flat spectral index.

the galactic center, and a combination of gravitational instability and cloud-cloud collision at the galactic center. This is because the ‘ N ’ value varies from 1.4 in the low- H_2 domain (where $\Sigma_{H_2} \ll 100 M_{\odot} \text{ pc}^{-2}$) to 2-3 in the high H_2 domain. In the Figure 3.17, one can see the SFRs obtained from this method, and how it changes radially.

Unfortunately, in NGC 628, I cannot do a comparison of the spectral indices and the star formation rates, as the flux density at the center of the galaxy is zero. In the paper Mulcahy et al. (2017), it is seen that NGC 628 at 8.35 GHz has an asymmetric pattern with a lot of emission coming in from the northern part of the galaxy, and not at the center. This would be in concurrence with the explanation that there is a rapid decline in the star formation at the inner region as described in Marcum et al. (2001). In the JVLA image, at the frequency of 3.1 GHz, there was a presence of ‘holes’ which line up with the type 1 H I holes⁹, as seen in Bagetakos et al. (2011). The absence of flux density can be attributed to rapid decline in SFR. However, I cannot be ascertain this in any way.

Using the Star Formation Rates given in Kennicutt et al. (2011), we can try to understand why the median values of the spectral indices of the two galaxies are so different. The SFR of IC 342 is $1.87 M_{\odot} \text{ pc}^{-1}$ while that of NGC 628 is $0.68 M_{\odot} \text{ pc}^{-1}$. Thus one could expect a flatter spectral index of IC 342 than that in NGC 628. Also, IC 342 suffers from a higher level of thermal absorption, indicating the presence of a higher level of star formation, especially at the nucleus of the galaxy.

3.4 Discussion

Further work needs to be done to fully understand the significance of thermal absorption in the galaxies at such low frequencies. Measurement of the spectra at low frequencies should be done using the LOFAR LBA data, and obtain the spectral energy distribution to see how much flux density of the galaxies is removed due to thermal absorption.

⁹H I holes are characterized by the absence of neutral hydrogen and have the dimensions from 100 pc to 1 kpc.

Chapter 4

Magnetic field study at Low frequency

4.1 Introduction

For several decades, the magnetic fields seen the galaxies have mystified astronomers. One of the main motivations behind studying these fields is to understand their contribution in the evolution of galaxies. Several questions about the magnetic fields needed to be answered such as whether magnetic field is just a consequence of the motion of the charged particles, or whether it influences the evolution. As charged particles are present pretty much every where, including the cold atomic clouds, magnetic field can exist every where in the galaxy. One of the first measurements of the magnetic fields in the nearby galaxies was done for the Andromeda galaxy (M31) in 1958. Interstellar linear polarization in Milky Way was studied in terms of extinction of selective elongated dust grain particles (the Davis-Greenstein effect). These particles get aligned by the magnetic field and hence provide us with the understanding of the interstellar magnetic fields which were parallel to the Galactic plane ([Lazarian & Hoang 2008](#)). To get a better understanding of the history of study of polarization in radio frequencies, one may refer to [Beck & Wielebinski \(2013\)](#).

One of the most important forces in the study of magnetic fields, is the Lorentz force¹, through which they influence the Interstellar Medium (ISM). Thus, the magnetic fields are some of the main contributors to the dynamical activity in galaxies. Relativistic electrons, through synchrotron emission, help us study the perpendicular magnetic field component \mathbf{B}_\perp . The degree of polarization of this emission is around 75%, though the actual measured quantity is much less.

In the recent years, two methods have been proposed to study the parallel component of the magnetic field in astronomical objects:

- **Zeeman splitting:** Splitting of an atomic or molecular line in the presence of a magnetic field is called Zeeman splitting. Amplitude of the Zeeman splitting, $\Delta\nu \propto \mathbf{B}$, with \mathbf{B} being the magnetic field. Hence, by measuring the $\Delta\nu$ one can measure the magnetic field. However, since the value of $\Delta\nu$ is very small, we use the measurement from the Right Circular Polarization (RCP) and the Left Circular Polarization (LCP) to find the $\mathbf{B}_{||}$. This measures more of the cold neutral cloud regions. Using this method, for the first time, H I observations of Cas A gave its magnetic fields.
- **Faraday rotation (FR) of linearly polarized light:** In the presence of a magnetic field (like in an ionized medium), the electromagnetic field has a right-hand (RH) mode, that is when the electric field is along the direction of motion of the gyrating electron and a left-hand (LH) mode that is when the electric field is in the opposite direction to the motion of the electron. The RH mode Electric field travels faster than the LH mode because of the interaction between the electric field and the electron. This in turn results in the rotation of the plane of polarization. The rotation angle ψ of a polarized radio wave is given by the equation [A.1](#), where λ is the wavelength of the observation (in m) and RM is the rotation measure in rad m^{-2} .

$$\text{RM} = \frac{\partial\psi}{\partial\lambda^2} \quad (4.1)$$

¹It is the force experienced by a charged particle in the presence of an electric (\mathbf{E}) and magnetic (\mathbf{B}) field and is written as: $\mathbf{F} = q\mathbf{E} + q(\mathbf{v} + \mathbf{B})$.

where the angle of polarization can also be written as:

$$\psi = \frac{1}{2} \tan^{-1} \frac{U}{Q} \quad (4.2)$$

In theory, one may obtain the RM by plotting the angle of polarization against the λ^2 . However, this is not feasible in real life because of several reasons, such as the $n\pi$ ambiguity. This effect is seen because the polarization angle is known only know in multiples of π . Hence, with a few wavelength bands, this fitting would just be arbitrary (for example in [Rand & Lyne \(1994\)](#)). Another major reason is depolarization, which is notably seen at lower frequencies. It was first observed in the paper [Wucknitz \(2010\)](#) for LOFAR. In this paper, it was seen that an unpolarized source was showing significant signal in the XY/YX correlations, and none in XX/YY. With the help of the RIME, this phenomenon can be mathematically explained. It can be shown that if a 1 Jy source undergoes a FR of $\pi/2[+2\pi n]$ on one of the stations and $0[+2\pi n]$ on the other station, all the original I flux will be detected as V. This phenomenon was termed as Differential FR. At the low frequencies in which LOFAR operates, ionospheric FR can be very high, making the observation of polarization significantly harder.

There are four major depolarizations seen other than wavelength dependent depolarization.

- **Bandwidth dependent depolarization:** This kind of depolarization occurs when the signal get depolarized within a frequency band. The polarized signal is reduced proportional to the sinc of the bandwidth (in terms of λ^2). This effect can be reduced by dividing the whole bandwidth into narrower channels.
- **Beam depolarization:** If the magnetic field is tangled on scales that are smaller than the resolution of the observation, some of the polarization is canceled out by itself inside the beam. This effect can be reduced by having better resolution.
- **Faraday dispersion:** The polarized emission sometimes is depolarized through by Faraday rotation the line of sight (LOS). If this occurs within the emission region, it is called internal, and if it is outside, it is called external.
- **Galactic foreground:** If the galaxy is present at lower galactic latitudes, this polarization becomes very important. It is caused by the polarization by the Milky Way galaxy. It is an example of external Faraday dispersion.

In order to curb the effects of the limited sampling of λ^2 , the technique of RM Synthesis is used as described in [Brentjens & de Bruyn \(2005\)](#), which is the continuation in the work done in the paper [Burn \(1966\)](#). This method is described in the next section.

4.2 Faraday Rotation Measure synthesis technique

Faraday depth (ϕ) of a source can be written as in equation 4.3. Here, $B_{||}$ is the parallel component of the magnetic field (in μG), n_e is the free electron density in cm^{-3} and dl is the path length in parsec².

$$\phi(\mathbf{r}) = 0.81 \int_{\text{here}}^{\text{there}} n_e B_{||} dl \text{ (rad m}^{-2}\text{)} \quad (4.3)$$

The polarization vector can be written in terms of the polarization angle as:

$$P(\lambda^2) = \int_{-\infty}^{+\infty} pI e^{2i[\psi_0 + \phi\lambda^2]} d\phi \quad (4.4)$$

Faraday dispersion function describes the intrinsic polarized flux, and can be written in terms of Faraday depth. Thus, we can wrote Faraay depth as $F(\phi) = pI e^{2i\psi_0}$. Thus, the relation is in the form of a Fourier transform, and can be inverted to give:

$$F(\phi) = \int_{-\infty}^{+\infty} P(\lambda^2) e^{-2i\phi\lambda^2} d\lambda^2 \quad (4.5)$$

²**Note:** One must remember that Rotation Measure is the same as Faraday Depth if and only if the Faraday rotating medium is present in front of the background source. If an emitting plasma exists in the source, then the equation can only be written in terms of ϕ . Thus, Faraday Depth is the general case and the RM is used for a specific case only.

However, we do not observe for wavelengths in which $\lambda^2 < \infty$ and *all* the values in which $\lambda^2 > 0$. Hence this technique was formulated. It also avoids bandwidth depolarization by averaging the complex polarization. The reconstructed Faraday dispersion function is thus written in the form described in equation 4.7. $R(\phi)$ is the Rotation Measure Synthesis Function (RMSF).

$$F'(\phi) = F(\phi) * R(\phi) \quad (4.6)$$

$$= K \sum_{i=1}^N w_i P_i e^{-2i\phi(\lambda_i^2 - \lambda_0^2)} \quad (4.7)$$

Here, $*$ denotes convolution. w_i is the weight of the i^{th} data point. The RMSF represents the response of the instrument because of the discrete separation of the bandwidth into separate channels. It is:

$$R(\phi) = K \sum_{i=1}^N w_i e^{-2i\phi(\lambda_i^2 - \lambda_0^2)} \quad (4.8)$$

$$K = \frac{1}{\sum_{i=1}^N w_i} \quad (4.9)$$

Once RM Synthesis has been performed, a deconvolution procedure called RM Clean is performed to get rid of the side lobes generated by the RMSF (Heald et al. 2009). These side-lobes provide difficulties in obtaining the Faraday Depth at which the source is present. This deconvolution is somewhat similar to the one performed during the imaging synthesis procedure. The flow chart in Figure 4.1 describes the different steps in performing RM Synthesis.

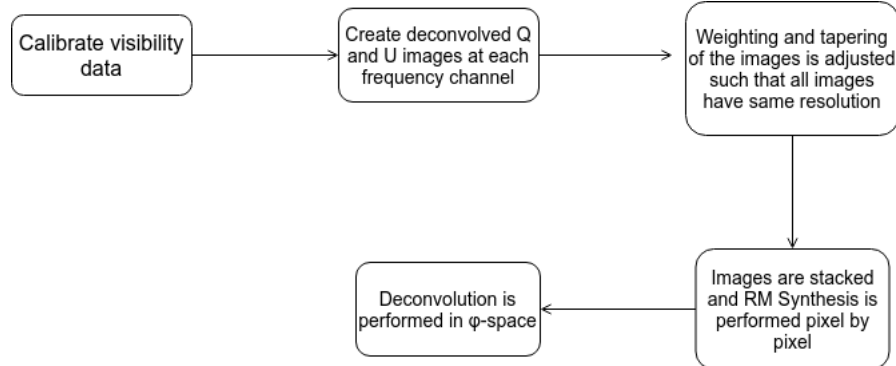


Figure 4.1: Flow chat depicting the procedure of RM Synthesis to understand polarization in astronomical objects, using the visibilities obtained from a radio receiver

Caveats: Some of the limitations of the RM Synthesis is described below:

- The deconvolution process may amplify the artifacts, thus decreasing the image quality.
- The higher and lower frequency images need to be of the same resolution, resulting in the loss of resolution of the higher frequency images due to the tapering and the convolution processes involved.
- Wide continuous frequency range is required to see the magnetic field structures in spiral galaxies.

There are other methods to obtain Rotation Measures- Faraday Synthesis (Bell & Enßlin 2012), (Heald et al. 2009) which is followed by clean, wavelets (Frick et al. 2010), compressive sampling (Li et al. 2011), and QU-fitting (Farnsworth et al. 2011). In the first three methods, the Faraday spectra is decomposed into some basis function. In the last method- QU fitting, models of synchrotron-emitting and Faraday rotating medium to the observed $P(\lambda)$ are assumed. In the paper Sun et al. (2015), the various methods were compared with each other to figure out which algorithm works the best to reconstruct the Faraday Spectra. The test was run on 1.1 to 1.4 GHz data with a S/N of 32 to 15. It was found that errors in the Faraday Depth weighted by polarized intensity were

sometimes almost a magnitude higher for the first three methods (Faraday Synthesis, wavelets and compressive sampling) than the errors from the QU fitting algorithm. Most of these methods worked well for Faraday thin sources³, while for Faraday thick structures⁴ all the methods fail. QU-fitting seems to have performed much better than the other methods.

4.3 Faraday tomography of the galaxies

The study of linear polarization helps us to understand the magnetic fields within the source through synchrotron polarization and Faraday rotation, and also through the LOS to the source with the help of Faraday rotation. Ideally, LOFAR would be a very good instrument to measure the polarization because it has the potential to measure to measure the Faraday depths to an accuracy of 0.1 rad/m^2 . It can also indicate the presence of two polarized sources which are separated only by a few rad/m^2 . It could, in principle, measure weak magnetic fields and detect low electron densities that are not observable at higher frequencies.

Magnetic fields in IC 342: Studying magnetic field for IC 342 at such a low frequency would be very interesting, because it has a high star formation rate at the center, unlike most of the other spiral galaxies, in which the star formation mostly takes place in the spiral arms. The high SFR at the center could be attributed to the inflow of gas from the outer parts of the galaxy in a steady form. In the Figure 27 in the paper Beck (2015), one can clearly see the “magnetic arms” of the galaxy pointing towards the center. The magnetic fields in the galaxy have been studied thoroughly at lower wavelengths such as 20.1 cm using VLA, in which it was found that depolarization effects dominate in the northern part of the galaxy, given the galaxy’s receding rotation. This is attributed to the galaxy’s helical fields that are present from the disk to the halo of the galaxy, as predicted by the mean-field dynamo models (see Beck (2015) for more information on this). It has also been studied at a wavelength of 6.3 cm and 11.1 cm using the Effelsberg telescope, where it was first found that the galaxy has an axisymmetric spiral field (Graeve & Beck 1988). The degree of polarization at the two wavelengths were about 13% and 10% respectively.

Magnetic fields in NGC 628: To study the magnetic fields of the disks of spiral galaxies, NGC 628 is one of the best as it is an almost-face on galaxy with a low inclination of around 7 deg. It is also an isolated galaxy (like IC 342), which would facilitate mean field dynamo to operate without any major disturbance. In the paper Mulcahy et al. (2017), NGC 628 was found to have an ordered magnetic field along the northern arm (in the regions **A** and **B** of the figure 3.12), with a high degree of polarization, possibly being caused by an asymmetric HI hole. A three dimensional field deviation called Parker loop which results in periodic small scale variations of the field orientation and position angle is seen in the northern arm (caused by Parker instability⁵). High level of polarization is seen in the inter arm regions, as observed in IC 342 (see Figure 28 of the paper to see the magnetic field lines).

4.3.1 RM Synthesis to study diffuse emission:

We first started with trying to detect diffuse polarized emission from the galaxies. In order to obtain the RM Cubes, first the stokes Q and U images are obtained at various frequencies using `wsclean`. These files are stored in two separate directories. This is followed by running `pyrmsynth` on them⁶. It uses the technique of Fourier transform to first obtain the dirty image, and then a FFT is performed to do the Fourier inverse. In order to do this, the data is required to be gridded by a convolution using the Kaiser-Bessel Window function⁷ and sampled at regular intervals. This takes care of non-regularly spaced frequencies (in case some of the frequencies had to be flagged during data processing).

The first aim of performing RM Synthesis was to study diffuse polarized emission. For IC 342, the stokes Q and U images had an average noise of 270 mJy. The Full Width Half Maximum of Rotation Measure Synthesis function

³A Faraday thin source is one in which $\lambda^2 \Delta \phi \ll 1$, with $\Delta \phi$ denoting the extent of the source in terms of Faraday Depth (ϕ). These sources are well approximated by a Dirac- δ function of ϕ .

⁴A Faraday thick source is one in which $\lambda^2 \Delta \phi \gg 1$, and it is extended in faraday depth. Such a source is considerably depolarized in λ^2 .

⁵A net force on the plasma that leads to its acceleration caused by magnetic buoyancy is called **Parker instability**.

⁶<https://github.com/mrbell/pyrmsynth>

⁷Kaiser Bessel Window function helps in the estimation of the DPSS window which is harder to calculate. In the function, the signal is concentrated in the main lobe. For more information, please take a look at Kaiser & Schafer (1980).

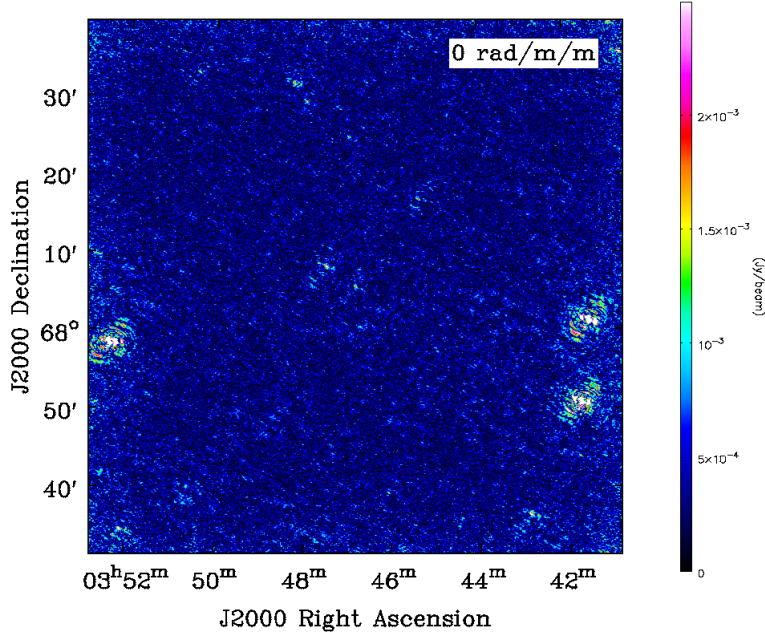


Figure 4.2: Instrumental polarization seen at the Faraday depth of 0 rad/m².

would give us the resolution of the Faraday depth. It is given by:

$$\Delta\phi = \frac{2\sqrt{3}}{\Delta\lambda^2} \quad (4.10)$$

In this case, the $\Delta\lambda$ is given by the width of observed λ^2 distribution. In case of IC 342 data, the RMSF is 0.88 rad/m², with a maximum frequency of 177 MHz and minimum frequency of 115 MHz. The largest detectable structure can be obtained using the value of minimum wavelength of the observation, λ_{min} . It is found to be 0.74 rad/m².

$$\phi_{max} = \frac{\pi}{\lambda_{min}^2} \quad (4.11)$$

Equations 4.10 and 4.11 have been taken from [Brentjens & de Bruyn \(2005\)](#). For IC 342, the cutoff is set as 0.1 mJy and 100 iterations of clean were performed. The resultant Faraday cube has a resolution of around 15 arcsec. We then try to smooth the Faraday cube to have a resolution of 40 arcsec, to try and observe any large scale polarized emission. None of the Faraday Cubes show any obvious diffuse polarized emission. At Faraday Depth of 0 rad/m², instrumental polarization can be seen around the sources that have a higher flux density in the stokes I image (see Figure 4.2). The rest of cube seems to have only noise.

For NGC 628 also, RM Synthesis is performed. It uses the same procedure as explained above. The resolution for the Faraday Depth is 0.814 rad/m². The maximum frequency used for this is 171.06 MHz and the minimum frequency is 110.7 MHz. The largest detectable structure is 0.695 rad/m². The cutoff is set as 0.1 mJy and 100 iterations of clean are performed. The galactic latitude of this galaxy is -45 deg. Even though this seems to be an optimistic latitude to observe polarization (compared to IC 342 whose latitude is 10.58 deg), there is no polarization seen for this galaxy. The lack of observation of polarization from the two galaxies can be attributed to the maximum detectable structure. Any structure with a Faraday Depth larger than the values given by the equation 4.11 would be depolarized.

Though diffuse emission has been studied using LOFAR, it is usually seen in the local interstellar medium, such as in the paper [Van Eck et al. \(2017\)](#), in which the field of view was towards IC 342. There is another study in the Fan region⁸ in which diffuse polarized emission was observed ([Iacobelli et al. 2013](#)). It is to be understood

⁸The Fan Region is centered near the Galactic plane at the latitude of +5 deg and longitude of 130 deg. It is a region that extends

RA ^a	DEC ^b	PI ₁₅₀ ^c	PI _{1.4} ^d	RM ₁₅₀ ^c	RM _{1.4} ^d	I _{1.4} ^d	DP
03 17 47.08±0.11	+68 25 08.30±7	33.45±0.89	15.4±0.7	-11.4±0.05	-32.9±15.8	168.4±5.7	0.131
03 17 42.46±0.08	+68 24 33.30±6	32.93±1.04	14.6±0.7	-8.6±0.05	-12.8±4.7	222.3±7.2	0.060
04 14 45.39±0.09	+69 01 08.30±6	5.67±0.37	8.0±0.5	-28.6±0.05	-32.9±15.8	115.7±4.1	0.124

Table 4.1: *a* and *b* represent the RA and DEC as given the the Taylor catalog. *d* is from the Taylor catalog, while *c* is the quantity of the Van Eck source. The degrees of depolarization is given in the last column using the equation 4.12.

that observations of diffuse emission from the galaxy itself is very difficult because of the depolarization effects along the line of sight, and wavelength dependent depolarization. Attempts to study the diffuse emission has been done using LOFAR for M51 in [Mulcahy et al. \(2014\)](#), which gave a similar result as the one indicated for the aforementioned galaxies. Thus, polarization for star forming galaxies is harder to detect, and the search for detection of polarization should be concentrated on galaxies that have a higher magnetic fields with little star formation.

4.3.2 Extra-galactic polarized sources

Studying extra-galactic polarized sources would be very useful to understand the evolution of populations of radio source, which in turn would probe the evolution of magnetic fields. Comparison of the source counts in the low frequency with that of higher frequencies, would help us understand the evolution of depolarization in radio sources, and thus the evolution of magnetic fields. Source detection might also help us in discovering new pulsars in our galaxy, as they are highly polarized point sources with a very steep spectrum, as done in [Jelić et al. \(2015\)](#), in which the source J081558+461155 is discovered as a pulsar in the field of 3C 196. Pulsars appear as Faraday thin sources, as the pulsar B1112+50 that was found in the paper [Van Eck et al. \(2018\)](#) in the LOFAR Two-meter Sky Survey (LOTSS). In the paper [Van Eck et al. \(2018\)](#), around 92 polarized sources are found in an area of 570 square degrees, i.e., 1 source per 6.2 deg. In [Mulcahy et al. \(2014\)](#), 6 polarized sources were found in an area of 17.3 square degrees, i.e., 1 source per 2.9 square degrees. In the paper [Van Eck et al. \(2017\)](#), 3 polarized sources (henceforth referred to as Van Eck sources) are detected in an area of 5 square degrees, in the field of IC 342, at the frequency of LOFAR.

Procedure: In order to study the polarization of extra-galactic sources at 150 MHz, I try to make smaller Faraday cubes around the sources that have been detected in [Taylor et al. \(2009\)](#), henceforth referred to as “Taylor catalog”. This is done because it is easier to study already detected sources, and understand their polarization and depolarization properties. This is done by first phase shifting the visibility data using the ‘phaseshifter’ function in NDPPP. Then, with the help of `pyrmsynth`, RM Cubes of these sources were made. Furthermore, I tried to manually identify sources, i.e., sources with a flux density of around 3 times the noise level of the image. One could also use the function `pyBDSF`⁹ provided in casa to do the same. This is done for both IC 342 and NGC 628. Unfortunately, I could not detect any polarization that I could be certain was true. For IC 342, there are three sources from the Taylor catalog that were in my field of view. It is to be noted that the Van Eck sources found are all out of the field of view I am studying, and were not detected. Hence, it is of no surprise that I could not detect any polarization from the three sources present in my field of view. The table 4.1 shows the Van Eck sources. The amount of depolarization in the Van Eck sources have been calulated by me using the formula in [Beck \(2007\)](#):

$$DP(150,1400) = \frac{PI_{150}/PI_{1400}}{(\nu_{1400}/\nu_{151})^\alpha} \quad (4.12)$$

Here, PI₁₄₀₀ is the polarization intensity at 1.4 GHz as given in the Taylor catalog, and PI₁₅₀ is the polarized intensity of the Van Eck sources. A value of 1 represents no additional depolarization has been seen at 150 MHz, while a value of 0 represents that the source is completely depolarized.

The values of degree of depolarization are similar to the ones in the paper [Mulcahy et al. \(2014\)](#), in the field of M51¹⁰. One cannot make a conclusion as to why some of the sources in the Taylor catalog cannot be seen the this frequency, as some of the sources that are present in my field of view have a polarized intensity from around 25 to 8 mJy, with a flux density of almost 600 mJy to 42 mJy (see table 4.2), that are in the range of the

over 60 × 30 deg, and is characterized by the electric field vectors that appear to fan out from the Galactic plane near 130 deg at frequencies of 600 MHz.

⁹(The Python Blob Detector and Source Finder, formerly PyBDSM) <http://www.astron.nl/citt/pybdsf/>

¹⁰0.038, 0.196 and 0.029 (not for the aforementioned sources!)

RA ^a	DEC ^b	$I_{1.4}^d$	$PI_{1.4}^d$	$RM_{1.4}^d$
03 52 23.34±0.08	+67 58 27.80±0.6	587.5±18.7	25.17±0.31	-11.2±2.5
03 52 14.00±0.1	+67 58 39.80±0.6	42.4±1.3	8.02±0.37	-13.8±7.9
03 41 30.77±0.08	+68 01 21.40±0.6	342.6±12	11.88±0.3	-32.2±5.3

Table 4.2: All these sources are from the Taylor catalog, which are present in my field of view. They are not polarized at 150 MHz in my study.

quantities of Van Eck sources. In the paper [Mulcahy et al. \(2014\)](#), polarization from sources with polarized intensity as low as 0.89 mJy has been studied, with the integrated flux density of one of the sources as low as 44 mJy.

For NGC 628, there are 34 sources from the Taylor catalog that are in the field of view. Similar procedure as the one for IC 342 is followed. None of these sources are seen to have any polarized emission. The Faraday spectrum of one of the sources is given in the Figure 4.4. This is most probably an AGN source, as can be seen in the Figure 4.3. It has a peak polarized intensity of 7.32 mJy and a flux density of 112.7 mJy. It is one of the higher values among the other sources present in the field of view, and is expected to show polarization at 150 MHz frequency range. However, no clear peak can be seen in the Faraday spectrum.

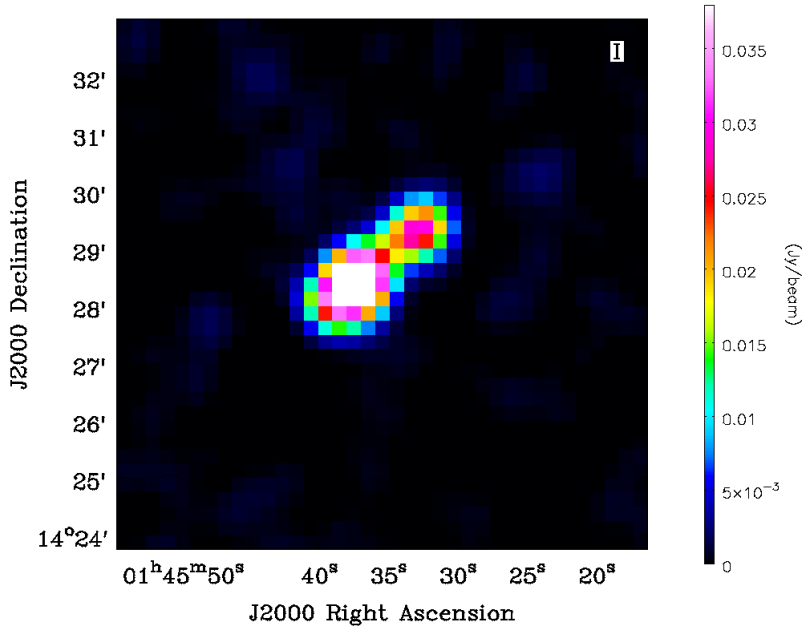


Figure 4.3: One of the sources from the Taylor catalog that has been observed to have a higher polarized intensity compared to other sources in the FoV of NGC 628 (7.32 mJy). It is expected to be polarized at 150 MHz, but no polarization is seen. This image has been taken from the NVSS survey and is at a frequency of 1.4 GHz.

In order to identify, I use the code provided by Dr. S.P O' Sullivan (priv. communication), which uses the method described in [George et al. \(2012\)](#) to detect sources. I first try to set the detection threshold for the smaller RM Cubes as $8\sigma_{QU}$. This provides no results. Similar results are obtained for the thresholds of $7\sigma_{QU}$, $5\sigma_{QU}$, $3\sigma_{QU}$ and finally $2\sigma_{QU}$. The σ_{QU} value is calculated by the code, which uses the noise value from the Faraday depths over beyond +100 and less than -100, as no polarized sources have been detected at such high and low Faraday depths. The Faraday depths from -5 to +5 are avoided due to the presence of instrumental polarization effects. I try the same for most of the sources in the field of view that are present in Taylor catalog, with negative results.

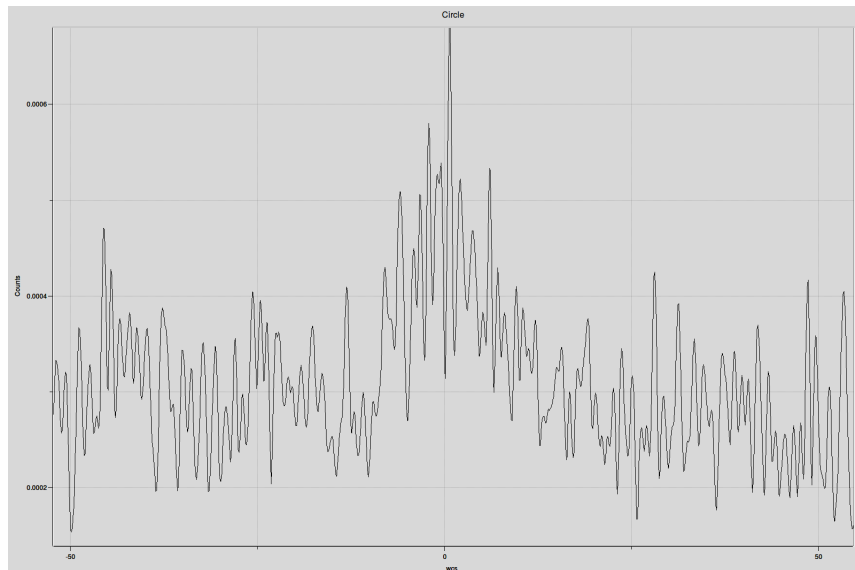


Figure 4.4: Most of the Faraday Spectrum that has been studied looks like this, thus making it impossible to understand if there are any real peaks in the Faraday spectrum.

Appendix A

Appendix

A.1 Radio Interferometry Measurement Equation- RIME formalism

The calibration techniques used for LOFAR are based on RIME formalism. The explanation closely follows the one given in (Smirnov 2011), since the Direction Dependant Effects (DDE) are well explained in it. This section describes the calculation of RIME from the voltages obtained at the antennae.

Consider a quasi-monochromatic source giving out a signal. This can be represented by a complex vector \mathbf{e} (the “original signal”), and be written in the form of a matrix using an orthogonal coordinate system xyz , with ‘ z ’ along the direction of propagation.

$$\mathbf{e} = \begin{pmatrix} e_x \\ e_y \end{pmatrix}$$

The signal encounters multiple effects on its path towards the antennae. These effects are assumed to affect the signal *linearly*. The signal changes to \mathbf{e}' due to these effects and can be written in the form given in the equation A.1.

$$\mathbf{e}' = \underbrace{\mathbf{J}_n \mathbf{J}_{n-1} \dots \mathbf{J}_1}_{\text{Jones chains}} \mathbf{e} = \mathbf{J} \mathbf{e} \quad (\text{A.1})$$

Here, \mathbf{J} is a 2×2 complex matrix known as Jones matrix. Since there are multiple effects along the path of the signal, the Jones chain is written taking all these effects into account and the final cumulative Jones matrix can be written as \mathbf{J} . If a and b are two linear dipole feeds, the signal one reaching and gets converted to complex voltages v_a and v_b representing the two polarizations.

$$\mathbf{v} = \begin{pmatrix} v_a \\ v_b \end{pmatrix} = \mathbf{J} \mathbf{e} \quad (\text{A.2})$$

An interferometer consists of several antennae elements, so let us consider two such spatially separated elements - p and q , giving independent voltage vectors v_p and v_q . Their voltages are correlated to give the visibility matrix V_{pq} . Hence, the visibility matrix can be written as:

$$V_{pq} = 2 \begin{pmatrix} \langle v_{pa} v_{qa}^* \rangle & \langle v_{pa} v_{qb}^* \rangle \\ \langle v_{pb} v_{qa}^* \rangle & \langle v_{pb} v_{qb}^* \rangle \end{pmatrix}$$

Here, v^* represents the complex conjugate of v . V_{pq} can be written as matrix product of v_p and complex conjugate of v_q . H represents the conjugate transpose operation.

$$V_{pq} = 2 \langle v_p v_q^H \rangle \quad (\text{A.3})$$

Combining equations A.2 and A.3, we get:

$$V_{pq} = 2 \langle \mathbf{J}_p (\mathbf{e} \mathbf{e}^H) \mathbf{J}_q \rangle \quad (\text{A.4})$$

We assume that \mathbf{J}_p and \mathbf{J}_q are constant over the averaging interval.

$$V_{pq} = 2 \langle v_p v_q^H \rangle = 2 \mathbf{J}_p \begin{pmatrix} \langle e_x e_x^* \rangle & \langle e_x e_y^* \rangle \\ \langle e_y e_x^* \rangle & \langle e_y e_y^* \rangle \end{pmatrix} \mathbf{J}_q^H \quad (\text{A.5})$$

A relation can be obtained between the source signal and Stokes parameters (I, Q, U, V) as shown in (Hamaker et al. 1996), and a new matrix called the brightness matrix B is defined.

$$2 \begin{pmatrix} \langle e_x e_x^* \rangle & \langle e_x e_y^* \rangle \\ \langle e_y e_x^* \rangle & \langle e_y e_y^* \rangle \end{pmatrix} = \underbrace{\begin{pmatrix} I + Q & U + iV \\ U + iV & I - Q \end{pmatrix}}_{\text{Brightness matrix B}} \quad (\text{A.6})$$

The signal undergoes sequential layers of corruption, and the resulting Jones matrix \mathbf{J}_p can be written in the form of Jones chain: $\mathbf{J}_p = (\mathbf{J}_{pn} \cdot \mathbf{J}_{p(n-1)} \dots \mathbf{J}_{p1})$. The final Jones matrix can be thus written as a cumulative of the following terms:

- The **phase** term: Phase difference exists between the two antennae due to the path-length difference between the paths from source to p and q . This in turn corrupts the signal. Phase center is the direction in which the antennae are steered towards to minimize the phase difference¹. Considering the conventional coordinate system, with z axis pointed towards the phase center, antenna p 's location can be defined as $\mathbf{u}_p = (u_p, v_p, w_p)$. Thus, the phase term in Jones matrix formalism can be written as:

$$\mathbf{K}_p = e^{i\kappa_p} = e^{-2i(u_p l + v_p m + w_p(n-1))}$$

Here, \mathbf{u} is defined in terms of wavelength. The visibility can hence be written (taking only the phase term into account)

$$V_{pq} = \mathbf{K}_p \mathbf{B} \mathbf{K}_q^H$$

The phase term is a scalar matrix, and hence can be moved around in the Jones chain.

- The **source-independent antenna** gain term: The interferometer itself also has some corrupting effects, and these can be considered in the Jones chain in the form \mathbf{G}_p . This describes the Direction Independent Effects (DIEs) or the uv- Jones term.
- The **source-dependent** gain term: This is the remainder of the Jones chain of the form \mathbf{E}_{sp} . This represents the Direction Dependent Effects (DDEs) or the sky-Jones term.

Hence, in total, the Jones chain can be written as:

$$\mathbf{J}_{sp} = \mathbf{G}_p \mathbf{E}_{sp} \mathbf{E}_{sp}^H \quad (\text{A.7})$$

The final visibility matrix can be written² as:

$$V_{pq} = \mathbf{G}_p \left(\sum_s \mathbf{E}_{sq} \mathbf{K}_{sq} \mathbf{B}_s \mathbf{K}_{sq}^H \mathbf{E}_{sq}^H \right) \mathbf{G}_q^H \quad (\text{A.8})$$

In LOFAR, this equation is taken over all the sufficiently bright sources in the horizon. However, sky is a continuous brightness distribution $B(\sigma)$ with σ being the unit direction vector. Hence, the total visibility for the interferometer should be in the form of an integration, not as a summation of discrete sources. When we write the visibility matrix in terms of the plane projection as described earlier (as opposed to the unit sphere integral, which is not very traceable) it is of the form in the equation A.9, with $n = \sqrt{1 - l^2 - m^2}$.

$$V_{pq} = \mathbf{G}_p \left(\int_l \int_m \frac{1}{n} \bar{\mathbf{E}}_p(l, m) \mathbf{B} \bar{\mathbf{E}}_q^H(l, m) e^{-2\pi i(u_{pq}l + v_{pq}m + w_{pq}(n-1))} dl dm \right) \mathbf{G}_q^H \quad (\text{A.9})$$

¹The net measured visibility is lowered in amplitude due to the presence of this complex term in the Jones matrix, which is variable in terms of both frequency and time. This effect is called “smearing”.

²This equation is in the “onion form”. In this way, the various effects/corruptions are sequentially applied to the signal

Decomposing $w_{pq} = w_p - w_q$ and writing the non-coplanetary term as per antenna terms, we can substitute $W_p = \frac{1}{\sqrt{n}} e^{-2\pi i w_p(n-1)}$ and write $\mathbf{E}_p = \bar{\mathbf{E}}_p W_p$. This would give us the visibility matrix in the form of a 2D Fourier Transform of the apparent sky brightness for the baseline pq (with the term B_{pq} in the place of $\mathbf{E}_p \mathbf{B} \mathbf{E}_q$).

$$V_{pq} = \mathbf{G}_p \left(\int_l \int_m B_{pq} e^{-2\pi i (u_{pq}l + v_{pq}m)} \right) \mathbf{G}_q^H \quad (\text{A.10})$$

This is the general form of the **Van Cittert Zernike theorem**. This is the formalism used by the LOFAR calibration software. This equation effectively takes care of the direction dependent effects. Using this fourier relation, and applying the Inverse Fast Fourier Transform (IFFT) algorithm, we can synthesis an image.

A.2 NGC 628- correlation plot

The Figure A.1 shows the correlation plot for the thermal region for A, C and D regions, for NGC 628. The regions are marked in the Chapter 3 of the thesis in Figure 3.12.

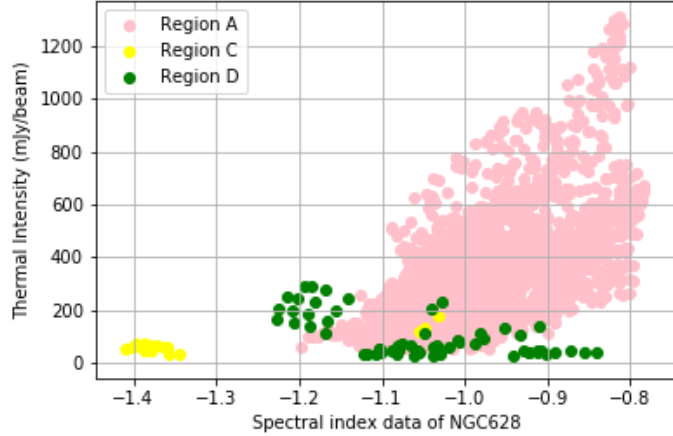


Figure A.1: Correlation of the flux density value with the spectral index map values, for each pixel. The various regions have different slopes of correlation, which is interesting. This plot shows the regions A, C and D.

A.3 Making of thermal maps

To understand how the thermal map is made, one can refer to [Mulcahy et al. \(2017\)](#). In this section I will explain why a simple H- α map might not be sufficient if one needs to do an in-depth analysis of thermal emission in the galaxy, and for an accurate determination of the magnetic fields in the galaxy. Classically, the separation of the thermal and non-thermal components has been done by assuming the spectral index of synchrotron emission to be $\alpha_{\text{Syn}} = -1.0$. This method overestimates the amount of thermal emission in the spiral arms, as the α_{Syn} in such regions is flatter than the assumed value. The α_{Syn} is also steeper in the inter-arm regions and the outer disk of the galaxy, where a higher amount of synchrotron emission takes place. This leads to an overestimation of the thermal emission in such regions. Another approach is to use 24 μm infrared (IR) map to estimate the thermal emission. This method also has its own set of caveats viz, IR emission may also come from non-thermal sources such as super massive black holes, and energetic cosmic rays (CRs) may also produce IR, thus overestimating the thermal fractions in such regions. In this thesis, the thermal map has been made using an extinction corrected H- α map. An H- α map in itself suffers from dust extinction, which would underestimate the amount of thermal emission. In the method where extinction correction is done, the optical depth for the whole galaxy is obtained using high resolution FIR data at 70 and 160 μm . Using this, one can determine the amount of extinction, thus producing a very good estimate of the thermal template. This method was developed by [Tabatabaei et al. \(2007\)](#), and is used in the thermal map that I use in my thesis for NGC 628. The thermal map for IC 342 was based on the

separation of the thermal and non- thermal components by assuming a constant spectral index, as the extinction corrected thermal map was not available. My thesis does not require an accurate determination of magnetic fields and cosmir ray propagation. Thus, a superficial understanding of the thermal regions in the galaxy was sufficient.

Bibliography

- Bagetakos, I., Brinks, E., Walter, F., et al. 2011, *The Astronomical Journal*, 141, 23
- Baker, J. R., Haslam, C. G. T., Jones, B. B., & Wielebinski, R. 1977, *Astronomy & Astrophysics*, 59, 261
- Balser, D. S., Wenger, T. V., Goss, W. M., Johnson, K. E., & Kepley, A. A. 2017, *Astrophysical Journal*, 844, 73
- Beck, R. 2007, *Astronomy & Astrophysics*, 470, 539
- Beck, R. 2015, *Astronomy & Astrophysics*, 578, A93
- Beck, R. & Wielebinski, R. 2013, *Magnetic Fields in Galaxies*, ed. T. D. Oswalt & G. Gilmore, 641
- Bell, M. R. & Enßlin, T. A. 2012, *Astronomy & Astrophysics*, 540, A80
- Bell Burnell, S. J. 1979, *Cosmic Search*, 1, 16
- Brentjens, M. A. & de Bruyn, A. G. 2005, *Astronomy & Astrophysics*, 441, 1217
- Burke, B. F. & Franklin, K. L. 1955, *Journal of Geophysical Research*, 60, 213
- Burn, B. J. 1966, *Monthly Notices of The Royal Astronomical Society*, 133, 67
- Cohen, A. S., Lane, W. M., Kassim, N. E., et al. 2006, *Astronomische Nachrichten*, 327, 262
- Condon, J. J. 1992, *Annual review of astronomy and astrophysics*, 30, 575
- Condon, J. J., Cotton, W. D., Greisen, E. W., et al. 1998, *The Astronomical Journal*, 115, 1693
- Cornwell, T. J., Golap, K., & Bhatnagar, S. 2008, *IEEE Journal of Selected Topics in Signal Processing*, 2, 647
- Cornwell, T. J., Voronkov, M. A., & Humphreys, B. 2012, in *Proceedings of the International Society for Optical Engineering*, Vol. 8500, *Image Reconstruction from Incomplete Data VII*, 85000L
- de Blok, W. J. G., Walter, F., Brinks, E., et al. 2008, *The Astronomical Journal*, 136, 2648
- de Vaucouleurs, G., de Vaucouleurs, A., Corwin, Jr., H. G., et al. 1991, *Third Reference Catalogue of Bright Galaxies*. Volume I: Explanations and references. Volume II: Data for galaxies between 0^h and 12^h . Volume III: Data for galaxies between 12^h and 24^h .
- Dodorico, S., Dopita, M. A., & Benvenuti, P. 1980, *Astronomy and Astrophysics Supplement Series*, 40, 67
- Downes, D., Radford, S. J. E., Guilloteau, S., et al. 1992, *Astronomy & Astrophysics*, 262, 424
- Elmegreen, D. M. & Elmegreen, B. G. 1984, *The Astrophysical Journal Supplement Series*, 54, 127
- Evans, I. N., Primini, F. A., Glotfelty, K. J., et al. 2010, *The Astrophysical Journal Supplement Series*, 189, 37
- Ewen, H. I. & Purcell, E. M. 1951, *Nature*, 168, 356
- Farnsworth, D., Rudnick, L., & Brown, S. 2011, *The Astronomical Journal*, 141, 191
- Ferguson, A. M. N., Gallagher, J. S., & Wyse, R. F. G. 1998, *The Astronomical Journal*, 116, 673
- Fesen, R. A., Hammell, M. C., Morse, J., et al. 2006, *Astrophysical Journal*, 645, 283

- Freedman, D. & Diaconis, P. 1981, *Zeitschrift für Wahrscheinlichkeitstheorie und Verwandte Gebiete*, 57, 453
- Frick, P., Sokoloff, D., Stepanov, R., & Beck, R. 2010, *Monthly Notices of The Royal Astronomical Society*, 401, L24
- Ganda, K., Falcón-Barroso, J., Peletier, R. F., et al. 2006, *Monthly Notices of The Royal Astronomical Society*, 367, 46
- Gao, Y. & Solomon, P. M. 2004, *Astrophysical Journal*, 606, 271
- George, S. J., Stil, J. M., & Keller, B. W. 2012, *Publications of the Astronomical Society of Australia*, 29, 214
- Graeve, R. & Beck, R. 1988, *Astronomy & Astrophysics*, 192, 66
- Hamaker, J. P., Bregman, J. D., & Sault, R. J. 1996, *Astronomy and Astrophysics Supplement Series*, 117, 137
- Heald, G., Braun, R., & Edmonds, R. 2009, *Astronomy & Astrophysics*, 503, 409
- Heald, G. H., Pizzo, R. F., Orrú, E., et al. 2015, *Astronomy & Astrophysics*, 582, A123
- Hey, J. S., Parsons, S. J., & Phillips, J. W. 1946, *Nature*, 158, 234
- Hulse, R. A. & Taylor, J. H. 1975, *The Astrophysical Journal Letters*, 195, L51
- Iacobelli, M., Haverkorn, M., Orrú, E., et al. 2013, *Astronomy & Astrophysics*, 558, A72
- Intema, H. T., Jagannathan, P., Mooley, K. P., & Frail, D. A. 2017, *Astronomy & Astrophysics*, 598, A78
- Intema, H. T., van der Tol, S., Cotton, W. D., et al. 2009, *Astronomy & Astrophysics*, 501, 1185
- Jelić, V., de Bruyn, A. G., Pandey, V. N., et al. 2015, *Astronomy & Astrophysics*, 583, A137
- Kaiser, J. & Schafer, R. 1980, *IEEE Transactions on Acoustics, Speech, and Signal Processing*, 28, 105
- Kamphuis, J. & Briggs, F. 1992, *Astronomy & Astrophysics*, 253, 335
- Karachentsev, I. D., Karachentseva, V. E., Huchtmeier, W. K., & Makarov, D. I. 2004, *The Astronomical Journal*, 127, 2031
- Karachentsev, I. D. & Kashibadze, O. G. 2006, *Astrophysics*, 49, 3
- Kassim, N. E., Lazio, T. J. W., Erickson, W. C., et al. 2007, *The Astrophysical Journal Supplement Series*, 172, 686
- Kennicutt, R. C., Calzetti, D., Aniano, G., et al. 2011, *Publications of the Astronomical Society of the Pacific*, 123, 1347
- Kennicutt, R. C. & Hodge, P. W. 1980, *Astrophysical Journal*, 241, 573
- Kogut, A., Lineweaver, C., Smoot, G. F., et al. 1993, *Astrophysical Journal*, 419, 1
- Krause, M., Hummel, E., & Beck, R. 1989, *Astronomy & Astrophysics*, 217, 4
- Lane, W. M., Cotton, W. D., Helmboldt, J. F., & Kassim, N. E. 2012, *Radio Science*, 47, RS0K04
- Lazarian, A. & Hoang, T. 2008, *The Astrophysical Journal Letters*, 676, L25
- Li, F., Brown, S., Cornwell, T. J., & de Hoog, F. 2011, *Astronomy & Astrophysics*, 531, A126
- Longair, M. S. 2011, *High Energy Astrophysics*
- Marcum, P. M., O'Connell, R. W., Fanelli, M. N., et al. 2001, *The Astrophysical Journal Supplement Series*, 132, 129
- Martini, P., Regan, M. W., Mulchaey, J. S., & Pogge, R. W. 2003, *The Astrophysical Journal Supplement Series*, 146, 353

- McMullin, J. P., Waters, B., Schiebel, D., Young, W., & Golap, K. 2007, in Astronomical Society of the Pacific Conference Series, Vol. 376, Astronomical Data Analysis Software and Systems XVI, ed. R. A. Shaw, F. Hill, & D. J. Bell, 127
- Meidt, S. E., Rand, R. J., & Merrifield, M. R. 2009, *Astrophysical Journal*, 702, 277
- Meier, D. S. & Turner, J. L. 2005, *Astrophysical Journal*, 618, 259
- Michelson, A. A. & Pease, F. G. 1921, *Astrophysical Journal*, 53
- Mulcahy, D. D., Beck, R., & Heald, G. H. 2017, *Astronomy & Astrophysics*, 600, A6
- Mulcahy, D. D., Horneffer, A., Beck, R., et al. 2014, *Astronomy & Astrophysics*, 568, A74
- Natali, G., Pedichini, F., & Righini, M. 1992, *Astronomy & Astrophysics*, 256, 79
- Offringa, A. R., van de Gronde, J. J., & Roerdink, J. B. T. M. 2012, *A&A*, 539
- Pan, H.-A., Kuno, N., & Hirota, A. 2014, *Publications of the Astronomical Society of Japan*, 66, 27
- Pandey, V. N., van Zwieten, J. E., de Bruyn, A. G., & Nijboer, R. 2009, in Astronomical Society of the Pacific Conference Series, Vol. 407, The Low-Frequency Radio Universe, ed. D. J. Saikia, D. A. Green, Y. Gupta, & T. Venturi, 384
- Perley, R. A. & Butler, B. J. 2017, *The Astrophysical Journal Supplement Series*, 230, 7
- Rana, V., Harrison, F. A., Bachetti, M., et al. 2015, *Astrophysical Journal*, 799, 121
- Rand, R. J. & Lyne, A. G. 1994, *Monthly Notices of The Royal Astronomical Society*, 268, 497
- Reber, G. 1944, *Astrophysical Journal*, 100, 279
- Rengelink, R. B., Tang, Y., de Bruyn, A. G., et al. 1997, *Astronomy and Astrophysics Supplement Series*, 124, 259
- Scaife, A. M. M. & Heald, G. H. 2012, *Monthly Notices of The Royal Astronomical Society*, 423, L30
- Schellart, P., Nelles, A., Buitink, S., et al. 2013, *Astronomy & Astrophysics*, 560, A98
- Schmidt, M. 1959, *Astrophysical Journal*, 129, 243
- Schulz, A., Güsten, R., Köster, B., & Krause, D. 2001, *Astronomy & Astrophysics*, 371, 25
- Smirnov, O. M. 2011, *Astronomy & Astrophysics*, 527, A106
- Sun, X. H., Rudnick, L., Akahori, T., et al. 2015, *The Astronomical Journal*, 149, 60
- Tabatabaei, F. S., Beck, R., Krügel, E., et al. 2007, *Astronomy & Astrophysics*, 475, 133
- Tabatabaei, F. S., Schinnerer, E., Krause, M., et al. 2017, *Astrophysical Journal*, 836, 185
- Taylor, A. R., Stil, J. M., & Sunstrum, C. 2009, *Astrophysical Journal*, 702, 1230
- Thompson, A. R., Moran, J. M., & Swenson, Jr., G. W. 2001, *Interferometry and Synthesis in Radio Astronomy*, 2nd Edition
- Turner, J. L. & Hurt, R. L. 1992, *Astrophysical Journal*, 384, 72
- van Ardenne, A., Smolders, B., & Hampson, G. 2000, in *Proceedings of the International Society for Optical Engineering*, Vol. 4015, Radio Telescopes, ed. H. R. Butcher, 420–433
- Van Eck, C. L., Havercorn, M., Alves, M. I. R., et al. 2018, ArXiv e-prints
- Van Eck, C. L., Havercorn, M., Alves, M. I. R., et al. 2017, *Astronomy & Astrophysics*, 597, A98
- van Haarlem, M. P., Wise, M. W., Gunst, A. W., et al. 2013, *Astronomy & Astrophysics*, 556, A2

van Weeren, R. J., Williams, W. L., Hardcastle, M. J., et al. 2016, *The Astrophysical Journal Supplement Series*, 223, 2

Wilkinson, P. N. 1991, in *Astronomical Society of the Pacific Conference Series*, Vol. 19, IAU Colloq. 131: Radio Interferometry. Theory, Techniques, and Applications, ed. T. J. Cornwell & R. A. Perley, 428–432

Wucknitz, O. 2010, in ISKAF2010 Science Meeting, 58